

Electrochemical Evaluation and Modulation of Surface Wettability

by

Chun Haow Kung

B.A.Sc., The University of British Columbia, 2015

A THESIS SUBMITTED IN PARTIAL FULFILLMENT OF

THE REQUIREMENTS FOR THE DEGREE OF

MASTER OF APPLIED SCIENCE

in

THE FACULTY OF GRADUATE AND POSTDOCTORAL STUDIES

(Chemical and Biological Engineering)

THE UNIVERSITY OF BRITISH COLUMBIA

(Vancouver)

August 2018

© Chun Haow Kung, 2018

The following individuals certify that they have read, and recommend to the Faculty of Graduate and Postdoctoral Studies for acceptance, a thesis entitled:

Electrochemical Evaluation and Modulation of Surface Wettability

submitted by Chun Haow Kung in partial fulfillment of the requirements for

the degree of Master of Applied Science

in Chemical and Biological Engineering

Examining Committee:

Walter Mérida, Mechanical Engineering

Supervisor

David Wilkinson, Chemical and Biological Engineering

Supervisory Committee Member

John Frostad, Chemical and Biological Engineering

Supervisory Committee Member

Abstract

Smart surfaces with dynamic and reversible wettability offer much versatility to meet various application needs. However, application of the smart materials remains challenging, mostly due to complex preparation procedure, a small change in the contact angle, and slow wettability switching. A thorough understanding of wetting phenomena is needed to achieve a breakthrough in the design of superwettability systems.

This thesis describes an electrochemical technique to evaluate the surface wettability of rough surfaces based on the wetted area under the droplet. The proportionality between the double layer capacitance and the ion accessible solid-liquid interfacial area is exploited to determine the actual wetted area. While the contact angle fails to describe the wetting mode, the electrochemical approach is capable of discerning the effective wetted area. The electrochemical wettability metric is also used to understand an anomalous wetting behaviour at which the contact angle and interfacial area of an intrinsically hydrophilic substrate show a concurrent increase with roughness. These observations contradict predictions from the Wenzel and Cassie-Baxter models. Based on a coupled optical and electrochemical analysis, the limitations of contact angle are highlighted.

An in-situ control over the wettability of electrodeposited copper structure through electrochemical modulation of oxidation state is demonstrated for the first time. Precise control over the rate and extent of the wetting transition is achieved by tuning the magnitude and duration of the applied voltage. Moreover, air drying at room temperature for 1 hour or mild heat drying at 100°C for 30 min restores the initial superhydrophobicity. Microstructural and electrochemical analysis show that the active wetting control is based on the Faradaic phase transformation of the surface-bound Cu_xO phase shielding the Cu core. Based on the wetting switching functionality of the Cu- Cu_xO core-shell structures, a smart oil-water membrane is designed. The as-deposited or air-dried Cu mesh exhibits superhydrophobicity and superoleophilicity, thus is effective for heavy oil-water separation. On the other hand, the application of a small reduction voltage (< 1.5 V) remediated light-oil contaminated water. Separation efficiencies greater than 98% are achieved with less than 5% variation over 30 cycles.

Lay Summary

Conventional evaluation of surface wettability, a property that governs the interaction between solid and liquid phases, is based on optical measurement of contact angle. However, the solid-liquid interaction beneath the droplet is optically inaccessible. A robust characterization technique is required to understand the structure-property relationship in the development of artificial wetting systems with different functionalities. Through determination of wetted area under the droplet for a series of carbonaceous surfaces with varying roughness, this work has demonstrated the capability of the electrochemical technique for enhancing the understanding of wetting phenomena. An in situ electrochemical alterations of wetting properties on additive-free metal oxide surface has also been demonstrated for the first time. The wetting transition is fully reversible via air-drying at room temperature or mild heat drying at 100°C. Application of the copper structures for on-demand separation of light oil-water and heavy oil-water mixtures shows efficiency above 98%.

Preface

The materials presented in this thesis, including the literature review, experimental work, data analysis, and thesis preparation, was completed by Chun Haow Kung under the supervision of Professor Walter Mérida at the Department of Chemical and Biological Engineering, the University of British Columbia. Dr. Beniamin Zahiri and Dr. Pradeep Kumar Sow provided guidance in the conception of experimental plans and data interpretation. Publications resulting from this work are listed below:

- A version of Chapter 1 is in preparation for publication:
 - 1) **Kung, C. H.**, Sow, P. K., Zahiri, B. & Mérida, W. Limitations of contact angle as wettability metric. To be submitted.
- Parts of Chapter 3 have been published in:
 - 2) Zahiri, B., Sow, P. K., **Kung, C. H.** & Mérida, W. Validation of surface wettability theories via electrochemical analysis. *Electrochem. commun.* **68**, 95–98 (2016)
 - 3) Zahiri, B., Sow, P. K., **Kung, C. H.** & Mérida, W. Electrochemical Approach to Evaluate the Wettability of Rough Surfaces. *ECS Trans.* **75**, 49–57 (2017)
 - 4) Zahiri, B., Sow, P. K., **Kung, C. H.** & Mérida, W. Understanding the wettability of rough surfaces using simultaneous optical and electrochemical analysis of sessile droplets. *J. Colloid Interface Sci.* **501**, 34–44 (2017)
- Parts of Chapter 4 have been published in:
 - 5) Zahiri, B., Sow, P. K., **Kung, C. H.** & Mérida, W. Active Control over the Wettability from Superhydrophobic to Superhydrophilic by Electrochemically Altering the Oxidation State in a Low Voltage Range. *Adv. Mater. Interfaces* **1700121**, 1700121 (2017)
 - 6) **Kung, C. H.**, Zahiri, B., Sow, P. K. & Mérida, W. On-demand oil-water separation via low-voltage wettability switching of core-shell structures on copper substrates. *Appl. Surf. Sci.* **444**, 15–27 (2018)
 - 7) **Kung, C. H.**, Zahiri, B., Sow, P. K. & Mérida, W. Electrochemical Wettability Control on Cu/Cu_xO Core-Shell Dendrites: In-Situ Droplet Modulation and On-Demand Oil-Water Separation. *MRS Advances*, 1-7 (2018)

The manuscript for item 1 was prepared by Chun Haow Kung with inputs from Drs. Benjamin Zahiri, Pradeep Kumar Sow and Walter Mérida. For items 2 to 7, the experiments were conducted by Chun Haow Kung in collaboration with Drs. Benjamin Zahiri and Pradeep Kumar Sow under the supervision of Dr. Walter Mérida. Chun Haow Kung performed the Atomic Force Microscopy (AFM) measurement and analysis. Microstructural analyses based on advanced imaging techniques, including X-Ray Diffraction (XRD), X-Ray Photoelectron Spectroscopy (XPS), High-Resolution Transmission Electron Microscopy (HR-TEM), Scanning Electron Microscopy (SEM), Scanning Transmission Electron Microscopy (STEM) and Energy Dispersive X-Ray Spectroscopy (EDS), were performed by Dr. Benjamin Zahiri.

The work has been presented by the author at the following conferences:

- 8) **Kung, C. H.**, Zahiri, B., Sow, P. K. & Mérida, W. Electrochemical Wettability Control on Cu/Cu_xO Core-Shell Dendrites for In-Situ Droplet Modulation and On-Demand Oil-Water Separation. *Material Research Society Spring Meeting*. (2018)
- 9) **Kung, C. H.**, Zahiri, B., Sow, P. K. & Mérida, W. Low-Voltage Reversibly Switchable Wettability through Electrochemical Manipulation of Oxidation State. *233rd Electrochemical Society Meeting*. (2018)
- 10) **Kung, C. H.**, Zahiri, B., Sow, P. K. & Mérida, W. Electrochemical Wettability Switching on Smart Stimuli-Responsive Surface. *6th Annual Young Electrochemists Symposium*. (2017)

Table of Contents

Abstract.....	iii
Lay Summary	iv
Preface.....	v
Table of Contents	vii
List of Tables	xi
List of Figures.....	xii
Nomenclature	xviii
List of Abbreviations	xxi
Acknowledgements	xxiii
1 Introduction.....	1
1.1 Surface wetting theories	1
1.2 Limitations of contact angle as wettability metric	5
1.2.1 Role of solid-liquid contact area and three-phase contact line	5
1.2.2 The multiplicity of contact angle values on the rough surface	8
1.2.3 Droplet size dependence of contact angle.....	12
1.3 Surface wetting control	15
1.3.1 Passive wettability control through surface chemistry and structure modification	15
1.3.2 Active wettability control on the stimuli-responsive surface	17
2 Motivation and research objectives.....	22
2.1 Objectives.....	22
2.2 Thesis layout	23
3 Electrochemical approach for surface wettability evaluation	25
3.1 Introduction	25
3.2 Experimental methods.....	28

3.2.1	Sample preparation	28
3.2.1.1	Plasma treatment.....	28
3.2.1.2	Mechanical polishing.....	28
3.2.2	High-throughput sessile droplet setup for simultaneous optical and electrochemical measurements.....	29
3.2.2.1	Contact angle measurements	30
3.2.2.2	Electrochemical measurements	32
3.2.3	Surface roughness characterization.....	32
3.3	Results and discussion.....	33
3.3.1	Wettability measurement of plasma treated GC substrates	33
3.3.1.1	Surface characterization	33
3.3.1.2	Optical wettability measurement	34
3.3.1.3	Electrochemical wettability measurement.....	35
3.3.2	Wettability measurement of mechanically polished GC substrates.....	39
3.3.2.1	Surface characterization	39
3.3.2.2	Optical wettability measurement	41
3.3.2.3	Electrochemical wettability measurement.....	44
3.4	Summary	52
4	Electrochemical wettability control.....	55
4.1	Introduction	55
4.2	Experimental methods.....	56
4.2.1	Sample preparation	56
4.2.2	Material characterization	57
4.2.3	Contact angle measurements and electrochemical wettability alteration on the copper plate.....	58
4.2.4	Water and oil contact angle measurements on as-deposited copper mesh	59

4.2.5	Electrochemical characterization of the as-deposited copper mesh	60
4.2.6	Oil-water separation experiments	60
4.3	Results and discussion.....	61
4.3.1	Surface characterization of electrodeposited copper surface.....	61
4.3.2	Wettability of as-prepared copper surface	65
4.3.3	Electrochemical wettability control: Effect of applied voltage and time duration .	68
4.3.4	Mechanism of the electrochemical wettability control.....	71
4.3.5	Reversibility of wetting alteration	75
4.3.5.1	Multi-cycle wetting transformation test	75
4.3.5.2	Surface structure and composition after wetting transition cycles	77
4.3.6	Application of electrochemical wettability control for on-demand oil-water separation	80
4.3.6.1	Surface characterization of electrodeposited copper mesh.....	80
4.3.6.2	Wettability of as-prepared copper mesh.....	85
4.3.6.3	Electrochemical alteration of the surface oxidation state.....	89
4.3.6.4	Controllable oil-water separation in water-removing and oil-removing mode	93
4.3.6.5	Mechanism of selective removal of water and oil.....	96
4.3.6.6	Recyclability of copper mesh	98
4.4	Summary	99
5	Conclusions and future considerations	101
5.1	Conclusions	101
5.2	Future work and recommendations	104
	Bibliography	107
	Appendices.....	141
	Appendix A: Measurement of advancing and receding contact angles	141

Appendix B: Cyclic voltammetry plots of mechanically abraded samples at different sweep rates and electrolyte concentrations	143
Appendix C: Stickiness of the electrodeposited copper surface	145
Appendix D: Effect of ambient hydrocarbon adsorption and mild heat drying at 100°C	147
Appendix E: Microstructural characterization of the copper mesh before and after 30 wetting transition cycles	149

List of Tables

Table 1.1: Overview of the wettability switching techniques reported in the literature.....	20
Table 3.1: Surface wetting properties of mechanically polished samples	41

List of Figures

Figure 1.1: Classification of wettability of a three-phase system using static contact angle.....	2
Figure 1.2: Schematic illustration of the effect of surface roughness on the wetting behaviour of solid surface: (a) Liquid droplet on an ideal smooth surface that can be described using the Young equation, (b) Droplet completely fills the grooves of rough surface (Wenzel state), (c) Droplet partially penetrates into the roughness features (Intermediate state between Wenzel and Cassie-Baxter regime), (d) Droplet sits on crests of rough patterns (Cassie-Baxter state).....	4
Figure 1.3: Schematic illustration of the existence of exterior and interior three-phase contact line for Wenzel and Cassie-Baxter wetting configurations. The red dotted arrow represents the possible direction of droplet movement in response to the supply of external energy.....	7
Figure 1.4: Gibbs energy profile of (a) an ideal solid surface and (b) a real (rough) solid surface in relation to the contact angle value.	9
Figure 1.5: Local deformation of the three-phase contact line as a result of surface defects leading to asymmetric droplet shape.....	10
Figure 1.6: Schematic illustration of the effect of droplet volume on the droplet symmetry and approximation to Wenzel and Cassie-Baxter equations for the rough solid surface. As the droplet size increases relative to the scale of surface heterogeneity, an approximation of the Wenzel and Cassie-Baxter models to the most stable contact angle improves. The corrugation of the contact line is exaggerated for illustration purpose.....	11
Figure 1.7: Summary of observed trends of the contact angle with increasing droplet volume in the literature. The droplet size dependence of the contact angle has been explained using the line tension (τ) effect.....	14
Figure 2.1: Thesis layout.....	24
Figure 3.1: Overview of two aspects of the limitations in static contact angle measurement addressed in this study. (a) Contact angle increase on an intrinsically hydrophobic surface can correspond to both Wenzel and Cassie-Baxter wetting states. (b) Experimental results showed an anomalous increase in contact angle and S-L interfacial area after the introduction of roughness on the intrinsically hydrophilic surface, which contradicts prediction of Wenzel and Cassie-Baxter models.	27

Figure 3.2: Schematic representation of the opto-electrochemical setup for simultaneous optical and electrochemical measurements. WE, CE and RE represent the working electrode, counter electrode and reference electrode, respectively. 30

Figure 3.3: SEM micrographs of the plasma-treated GC samples. The duration of O₂ plasma etching (t_{O_2}) of each sample is indicated at the bottom left of the respective SEM image. The histograms (inset) show the distribution of the width at half maximum height of the conical feature along with the average (μ) and standard deviation (σ). All samples were cleaned with O₂ plasma for 20 seconds. 34

Figure 3.4: Contact angle and projected geometric area (A_{geo}) of the samples with increasing roughness from Sample 1 to Sample 4. Sample 1, 2, 3 and 4 correspond to GC substrates that have undergone O₂ plasma etching for 0, 2, 5, and 10 min, respectively. 35

Figure 3.5: (a) Typical cyclic voltammetry curves for the plasma-treated samples obtained using a droplet of 10 μ L 0.1 M Na₂SO₄ with a scan rate of 100 mV s⁻¹. (b) Comparison of the ratio of the S-L interfacial area to the projected geometric area (A_{sl} / A_{geo}) to the predicted values based on the Wenzel and Cassie-Baxter models. 36

Figure 3.6: An experimental approach for validating theoretical wetting models. 39

Figure 3.7: SEM micrographs and AFM analysis of the mechanically abraded GC samples. The histograms show the depth distribution of the irregular surface roughness detected by the AFM measurement. SS refers to smooth GC sample that was polished to mirror finish. RS1, RS2, and RS3 correspond to GC substrates that had been roughened using the abrasive papers of grit size 1200, 800, and 400, respectively. 40

Figure 3.8: Typical cyclic voltammetry plots corresponding to a droplet volume of 5 μ L, a sweep rate of 100 mV s⁻¹ and an electrolyte concentration of 0.1 M Na₂SO₄. 44

Figure 3.9: Effect of scan rate and electrolyte concentration on the screening efficiency (the A_{sl} / A_{geo} ratio normalized by the lowest sweep rate data at 10 mV s⁻¹). All plots are scaled to similar y-axis values. 47

Figure 3.10: The influence of electrolyte concentration and sweep rate on the screening efficiency. 49

Figure 3.11: The ratio of the solid-liquid interfacial area (A_{sl}) to the geometrical area (A_{geo}) for droplet with electrolyte concentration of 0.001-1 M and sweep rate in the range of 10-500 mV s⁻¹ 50

Figure 4.1: Schematic illustration of the oil-water separation process involving (a) heavy oil-water mixture in oil-removing mode and (b) light oil-water mixture in water-removing mode. The separation efficiency is determined as the ratio of the mass of oil or water phase collected (m) to the mass before (m_0) the separation..... 61

Figure 4.2: The microstructure of the as-deposited copper affects the surface wettability. The SEM micrograph shows the structure of the as-deposited copper structure at (a) low and (b) high magnification. (c) A bar chart showing the average (μ) and standard deviation (σ) of the width of individual dendritic arms (w). (d) The crystal structure of the as-deposited sample studied using XRD. The dashed lines represent the copper XRD peaks, the arrow corresponds to an amorphous/nanocrystalline CuO and the solid circle is an unidentified phase. 63

Figure 4.3: Surface composition of the dendritic structure contributes towards the hydrophobic behaviour. (a) STEM-HAADF micrographs of the as-deposited dendrite structure. (b) STEM-EDS overlapping Cu and O and individual (c) Cu and (d) O elemental mapping. (e) STEM-HAADF of dendritic secondary arms. (f) Corresponding STEM-EDS overlapping and (g) Cu and (h) O mapping. (i) High-resolution XPS spectrum of Cu 2p and (j) O 1s signal from the as-deposited sample showing the presence of oxygen in the copper lattice as well as surface oxygen groups..... 64

Figure 4.4: The electrodeposited copper yields a surface that exhibits superhydrophobic behaviour. This behaviour is characterized by large contact angles (a) and droplet bouncing when dropped on the surface (b) showing the low adhesion easy roll-off properties. (c) Advancing (ACA) and receding (RCA) contact angle measurements obtained by varying the droplet volume between 10 to 20 μ L. The contact angle hysteresis (CAH) of the copper surface is $4.7 \pm 1.8^\circ$... 67

Figure 4.5: Modulation of the magnitude and duration of the applied voltage enables precise control over the rate and extent of the wetting transition. The potential represented here is referred with respect to that of the platinum pseudo-reference electrode (a) A conceptual representation of the electrochemical system where the substrate acts as the working electrode and two platinum wires as the counter and pseudo-reference electrode, respectively (b) Experimental results showing the change in the CA with time at varying reduction potentials. (c)

Results showing the stability of the CA achieved after the application of the potential. The CA reduces upon the application of reduction potential but remains stable when the potential is removed..... 70

Figure 4.6: The change in the contact angle and alteration of wettability occurs due to the electrochemical change in the oxidation state of copper. (a) Cyclic voltammogram of the as-prepared 2 cm² copper strip sample in 0.1 M Na₂SO₄ electrolyte solution conducted with a potential scan rate of 30 mV s⁻¹. (b) The current vs. time profile corresponding to a droplet under a constant reduction potential of -1 V. The sequence of images from A to H shows the evolution of the droplet shape over 180 seconds of the test. (c) A conceptual representation of the underlying mechanism for the contact angle alteration. Negative potential induces the reduction of Cu₂O to Cu and the droplet penetrates into the roughness features. Further application of the reduction potential causes the three-phase contact line of the droplet to spread leading to further reduction in the contact angle. The contact angle of the droplet after the first current peak corresponding to point B in (b) at the rotation angle of (d) 90° and (e) 180° shows the transition from roll-off to sticky surface with high adhesion..... 72

Figure 4.7: Experimental results illustrating the electrochemically controllable underwater hydrophobicity on the copper sample. The wettability alteration was found to be reversible. (a) The as-prepared sample on the copper strip immersed in 0.1 M Na₂SO₄ electrolyte shows a reflective surface due to superhydrophobicity. In the representation, WE and CE denote the working and counter electrodes. (b) The same sample as in (a) after 30 s under a reduction potential of -0.6 V vs. the Ag/AgCl reference electrode. (c) The contact angle of the copper sample measured for 10 consecutive transition cycles. Following the application of reduction potential, the sample showed superhydrophilic behaviour. After heating at 100°C for 30 min or at room temperature (25°C) for 1 hour, the initial superhydrophobic behaviour was regained. 76

Figure 4.8: Surface properties of the copper sample which has undergone 10 consecutive wetting transition cycles resembles that of the as-deposited counterpart. (a) The SEM micrographs of the post-cycled structure. (b) STEM-HAADF micrographs of the dendrite structure after cycling. The STEM-EDS mapping of (c) Cu and (d) O for individual secondary arm indicated by the square in (b). (e) The XRD pattern of the post-cycled structure. The dashed lines represent the copper XRD peaks, the solid circle is an unidentified phase. (f) XPS spectrum of Cu 2p region

for the post-cycled sample reveals similar copper oxide species as those in the as-deposited sample. 79

Figure 4.9: Microstructure of the (a) pristine and (b) as-deposited copper mesh. The inset shows the high magnification of the dendritic structure formed during electrodeposition. (c) The cross-section of a single Cu wire with the full coverage of dendritic structures. The thickness of the deposited layer ranges from 10 to 30 μm . (d) The XRD pattern of the dendritic structure shows a single FCC-Cu crystal structure. 81

Figure 4.10: **(a)**: (a-i) STEM-HAADF of a dendritic cluster with multiple branches. (a-ii) The STEM-EDS mapping of Cu and O on single dendrite branches indicated by the box in (a-i). The concentration of oxygen tends to increase from the interior towards the exterior regions of the dendrite. (a-iii) and (a-iv) HR-TEM of the near-surface regions indicated by arrow 1 and 2 in (a-i), respectively. The insets show the corresponding FFT to identify the lattice spacing. The surface consists of a mixture of CuO and Cu₂O phases while the interior regions contain metallic copper phase. **(b)**: (b-i) XPS profile of the Cu 2p region indicates the presence of Cu(I) and Cu(II) oxide species. (b-ii) The Cu 2p region after the Ar etching indicates the removal of the oxide species. (b-iii) O 1s XPS signal from the as-deposited sample shows the presence of oxygen in the copper lattice and surface oxygen groups. (b-iv) Comparison of the O 1s signal before and after the Ar ion etching shows the removal of the surface oxygen and decreased trace of oxygen in the copper lattice. 85

Figure 4.11: (a) The water contact angle (WCA), oil contact angle (OCA) and underwater oil contact angle (UWOCA) on the copper mesh after (a-i) air drying and (a-ii) voltage application. The OCA and UWOCA are determined using 1,2-dichloroethane. (b) High underwater oil contact angle (UWOCA) of different oils on the electrochemically modified copper mesh via voltage application illustrates the applicability of the mesh as a separator for oil of different densities and viscosities. 87

Figure 4.12: (a) CV profile the copper mesh over a reduction potential range of 0 to -0.8 V vs. Ag/AgCl reference. The inset shows the water contact angle of the mesh in the air before and after the electrochemical reduction. The mesh is superhydrophobic prior to the reduction reaction and turns superhydrophilic following voltage application of -1.5 V. The arrow 1 and 2 denote the forward scan from 0 V to -0.8 V and reverse scan from -0.8 to 0 V, respectively. (b) Nyquist and (c) Bode plots for the mesh surface before and after the reduction process at open circuit

potential. (d) Equivalent electrical circuits used to model the impedance data of the superhydrophobic (before wetting transition) and superhydrophilic (after wetting transition) copper mesh surface..... 92

Figure 4.13: (a) Reversible oil-water separation in oil-removing and water-removing mode triggered by air drying and voltage application (b) Series of images illustrating the on-demand separation of light oil-water mixture via voltage application and the use of the mesh for multiple separation cycles. CE and WE stand for counter and working electrodes, respectively. (c) The current profile of the mesh as it undergoes the wetting transition following application of reduction voltage of 1.5 V. (d) Separation efficiency of the copper mesh operating in both water-removing and oil-removing modes are higher than 98% for different oil-water mixtures..... 95

Figure 4.14: Schematic illustration of the separation process of (a) heavy oil-water mixture in oil-removing mode and (b) light oil-water mixture in water-removing mode. In both oil-removing and water-removing modes, liquid permeation begins by capillary-driven wicking into the dendritic structures followed by gravity-assisted flow through the mesh. At the end of the separation, the dendrite surface is infused with a thin film of oil (water) that restricts penetration of water (oil). 97

Figure 4.15: (a) WCA in air and UWOCA for 30 cycles of reversible transition between superhydrophobic/superoleophilic and superhydrophilic/underwater superoleophobic states induced by alternate air drying and voltage application. (b) The separation efficiency of the copper mesh in water-removing and oil-removing mode for 30 separation cycles. Toluene and 1, 2-dichloroethane are used as the representative light and heavy oil, respectively. 99

Nomenclature

Symbol	Description	Unit
A	Surface area	mm^2
A_{geo}	Projected geometric area	mm^2
A_{geo}^R	Projected geometric area of the rough sample	mm^2
A_{geo}^S	Projected geometric area of the smooth sample	mm^2
A_l	Liquid surface area	mm^2
A_s	Solid surface area	mm^2
A_{sl}	Solid-liquid interfacial area	mm^2
C	Double layer capacitance	$\mu\text{F cm}^{-2}$
C^R	Double layer capacitance of the rough sample	$\mu\text{F cm}^{-2}$
C^S	Double layer capacitance of the smooth sample	$\mu\text{F cm}^{-2}$
C_i^0	Bulk electrolyte concentration	mol L^{-1}
CPE_{dl}	Constant phase element corresponding to double layer capacitance	$\mu\text{F cm}^{-2}$
CPE_f	Constant phase element corresponding to the capacitance of oxide film	$\mu\text{F cm}^{-2}$
D	Droplet base diameter	mm
D_0	Droplet initial base diameter	mm
d	Double layer thickness	nm
E	Potential	V
E^0	Standard equilibrium potential	V
$E_f - E_0$	Potential window	V
e	Elementary charge	C
f_s	Solid-liquid fraction in the Cassie-Baxter equation	-
G	Gibbs free energy	J
I	Current	A

k_B	Boltzmann constant	J K^{-1}
L	Crystallite size	nm
m	Mass after separation	g
m_0	Mass before separation	g
ΔP	Pressure difference across liquid-air interface	Pa
R	The radius of the three-phase contact line	mm
R_1, R_2	Principal radii of curvature in the Young-Laplace equation	mm
R_{ct}	Charge transfer resistance	$\Omega \text{ cm}^2$
R_f	Pore resistance of oxide film	$\Omega \text{ cm}^2$
R_s	Ohmic resistance	$\Omega \text{ cm}^2$
r	Surface roughness factor in the Wenzel equation	-
T	Temperature	$^{\circ}\text{C}$
t_{O_2}	Duration of oxygen plasma etching	min
V	Droplet volume	mm^3
w	The width of dendritic arm	nm
Z	Impedance	$\Omega \text{ cm}^2$
Z_i	Valency of ion i	-
z	Atomic number	-
β	Full width at half maximum intensity	radian
ϵ_0	Permittivity of vacuum	F m^{-1}
ϵ_r	The dielectric constant of electrolyte	-
κ	Debye-Hückel parameter	nm^{-1}
γ	Surface tension	N m^{-1}
γ_o	Oil-air interfacial tension	N m^{-1}
γ_w	Water-air interfacial tension	N m^{-1}
γ_s	Solid surface tension	N m^{-1}
γ_l	Liquid surface tension	N m^{-1}
γ_{ow}	Oil-water interfacial tension	N m^{-1}

γ_{SV}	Solid-vapor interfacial tension	N m^{-1}
γ_{SL}	Solid-liquid interfacial tension	N m^{-1}
γ_{LV}	Liquid-vapor interfacial tension	N m^{-1}
η	Separation efficiency	%
θ	Apparent contact angle	°
θ_{\max}	The position of peak maximum in Scherrer equation	°
θ_Y	Young Contact Angle	°
θ_o	Oil contact angle in air	°
θ_w	Water contact angle in air	°
θ_{ow}	Underwater oil contact angle	°
θ_∞	The contact angle of an infinitely large droplet	°
λ	X-Ray Wavelength	Å
μ	Average	-
σ	Standard deviation	-
τ	Line tension	J m^{-1}
ν	Potential scan rate	V s^{-1}

List of Abbreviations

Abbreviation	Description
ACA	Advancing Contact Angle
ACCA	Actual Contact Angle
AFM	Atomic Force Microscopy
APCA	Apparent Contact Angle
CA	Contact Angle
CAH	Contact Angle Hysteresis
CAH _{evap}	Contact Angle Hysteresis value from evaporation method
CE	Counter Electrode
CPE	Constant Phase Element
CV	Cyclic Voltammetry
DI	Deionized
ECA	Equilibrium Contact Angle
EDS	Energy Dispersive X-Ray Spectroscopy
EEC	Equivalent Electrical Circuit
EIS	Electrochemical Impedance Spectroscopy
FCC	Face-Centered Cubic
FFT	Fast Fourier Transform
FWHM	Full Width at Half Maximum
GC	Glassy Carbon
HAADF	High-Angle Annular Dark Field
HR-TEM	High-Resolution Transmission Electron Microscopy
OCA	Oil Contact Angle
OCP	Open Circuit Potential
RCA	Receding Contact Angle
RE	Reference Electrode
RF	Radio Frequency
RS	Rough Sample
SEM	Scanning Electron Microscopy

S-L	Solid-Liquid
SS	Smooth Sample
STEM	Scanning Transmission Electron Microscopy
UV	Ultraviolet
UWOCA	Underwater Oil Contact Angle
WCA	Water Contact Angle
WE	Working Electrode
XPS	X-Ray Photoelectron Spectroscopy
XRD	X-Ray Diffraction
YCA	Young Contact Angle

Acknowledgements

First and foremost, I would like to express my deepest gratitude to my supervisor, Dr. Walter Mérida, for giving me the opportunity to be part of his research group. His guidance and continuous support throughout my M.A.Sc program is invaluable and much appreciated.

Thank you to Dr. David Wilkinson and Dr. John Frostad for serving on my thesis committee and taking the time to review my thesis.

I am indebted to two knowledgeable and helpful mentors and friends, Dr. Benjamin Zahiri and Dr. Pradeep Kumar Sow, for their unconditional support, constructive advice and mentorship. This work would not be possible without their help.

I am grateful to Dr. Jesus Diaz Real and Dr. Omar Herrera for offering valuable suggestions and guidance. Moreover, I would like to thank Gethin Owen from UBC Center for High-Throughput Phenogenomics (CHTP) for sharing his expertise on scanning electron microscopy (SEM). I also thank Chris Balicki and Tom Cherng from 4D LABS for training in atomic force microscopic (AFM) and reactive ion etching (RIE). My appreciation extends to all my friends and colleagues at Rusty Hut and Clean Energy Research Centre (CERC) for their support whenever in need.

Lastly, I would also like to acknowledge the financial support from the University of British Columbia (UBC) and the Electrochemical Society (ECS) in the form of awards and travel grant.

1 Introduction

1.1 Surface wetting theories

Surface wettability is a key physical parameter which manifests the affinity of a liquid towards a solid phase. Wetting phenomena are ubiquitous and central in various biological systems and technological applications. For instance, the lotus leaf relies on its self-cleaning and water-repelling feature to keep the surface free from dirt and contamination, despite living in a muddy habitat. In industrial applications such as the printing, painting and water treatment industries, the solid-liquid interfacial interaction embodies a range of surface properties, including the surface adhesion, friction, biocompatibility, and catalytic activity. When a liquid is brought in contact with a solid phase, it forms the solid-liquid interface by replacing another fluid (which is usually a vapour phase). The liquid droplet shape is a result of the competition between the cohesive interactions between the like molecules in the liquid phase and the adhesive interactions between the solid and liquid phases¹⁻³. Intrinsically a solid surface with a high affinity towards the liquid phase would form a larger solid-liquid contact area. Alternatively, the liquid would minimize the contact with the solid surface in the presence of a strong cohesive force due to the resistance to separation between the liquid molecules. Characterization of wetting properties of the solid surface has attracted continued interest from the industry and scientific community due to their fundamental importance as well as vast applications in the field of painting, printing, cleaning, and many more⁴⁻⁷.

Due to its simple measurement procedures, contact angle has been widely used as a parameter to quantify the wetting characteristics of solid surfaces and solid-liquid interaction⁸⁻¹⁰. Based on the traditional wettability criteria, a system with a static contact angle less than 90° is regarded as hydrophilic (water-attracting) whereas those with a contact angle greater than 90° are hydrophobic (water-repelling), as depicted in Figure 1.1¹¹⁻¹⁷. However, the general classification as a hydrophilic or a hydrophobic behaviour based on the cut-off contact angle of 90° has attracted few criticisms^{18,19}. Even though the measurement of contact angle appears to be operationally straightforward, interpretation of the measurement is often complicated by an array of factors, including surface smoothness, heterogeneity and cleanliness²⁰. Any variations in these surface properties can result in a significant deviation in the measured contact angle, which could render the interpretation of the experimental results challenging.

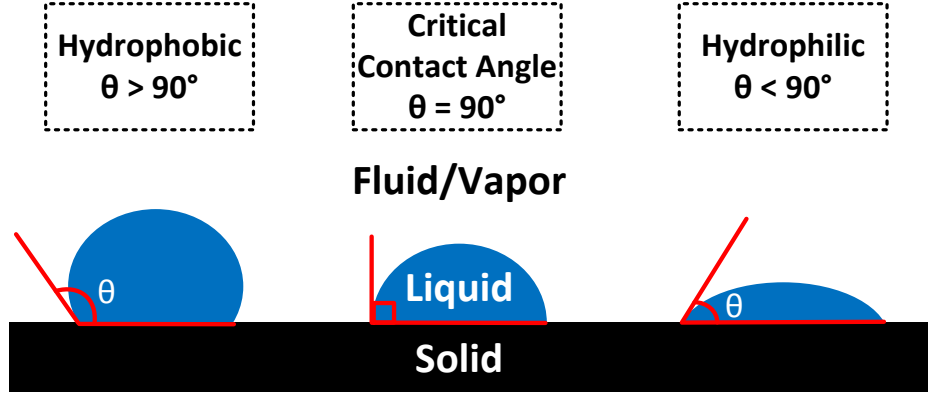


Figure 1.1: Classification of wettability of a three-phase system using static contact angle.

An ideal solid surface is defined as topographically smooth, rigid, chemically homogeneous, insoluble and non-reactive ^{11,21-23}. The homogeneity of the surface results in a uniform surface energy and therefore such ideal surface has a single unique contact angle value. The equilibrium state for a solid-liquid-air system corresponds to the configuration at which the Gibbs free energy of the entire system is at a minimum value ^{24,25}. In other words, the contact angle of a droplet on the ideal surface depends only on the intrinsic surface chemistry, which in turn dictates the Gibbs free energy minimum ^{22,26}. The contact angle on such surfaces can be uniquely described using the Young equation through Young contact angle (YCA). The Young equation (Equation (1.1)), formulated based on the force balance at the interface of all three phases (solid, liquid and fluid) around 200 years ago, is one of the most well-known models used to quantify solid surface energy using the contact angle, θ_Y ²⁷⁻³⁰:

$$\cos \theta_Y = \frac{\gamma_{SV} - \gamma_{SL}}{\gamma_{LV}} \quad (1.1)$$

In the above representation, γ_{SV} , γ_{SL} and γ_{LV} are interfacial tensions between the solid-vapour phase, solid-liquid phase and liquid-vapour phase, respectively. The contact angle (θ) is defined as the angle between the tangent to the solid-liquid and liquid-fluid interfaces at the three-phase contact line, as illustrated in Figure 1.1 ¹¹. The macroscopic contact angle corresponding to the configuration of global Gibbs energy minimum is also known as the equilibrium contact angle (ECA) ³¹. Nonetheless, almost all materials encountered in real life applications exhibit certain extent of intrinsic roughness features. Therefore, the interactions under the droplet and more specifically the solid-liquid interfacial area under the droplet can be

significantly different from that of a perfectly smooth surface. These differences in the interactions lead to variation in the apparent contact angle (APCA), which is the angle between tangents to the liquid-air interface and the macroscopically observable solid surface. This APCA is experimentally measurable and is widely used as a measure of the surface wetting properties owing to its straightforward experimental evaluation process. Nevertheless, the APCA could correspond to the droplet in either the most stable or metastable wetting states. This means that the APCA might be different from the ECA for the rough solid surface. Since the surface wettability dictates the formation of the solid-liquid interface, the APCA should correlate with the geometric considerations and most importantly the wetted area.

The wetting properties of a material are predominantly governed by its chemical composition and surface geometrical structure^{32–37}. Depending on the interplay between these two factors, wetting of rough solid surfaces can be classified into three general categories: Wenzel, Cassie-Baxter and mixed Cassie-Wenzel (intermediate) states, as shown schematically in Figure 1.2^{37,38}. In Wenzel wetting state (also known as homogeneous wetting), the water droplet penetrates completely into the corrugations, cracks and other roughness features of the solid surface and is in full contact with the surface beneath the droplet. On the other hand, the droplet in Cassie-Baxter state (also known as Fakir state or heterogeneous wetting state) is suspended on the tip of surface asperities at which air remains trapped underneath the liquid phase in the grooves. For a system in an intermediate state between Wenzel and Cassie-Baxter wetting states, the droplet only partially fills the grooves between the roughness features. In light of different wetting configurations that could be induced by surface irregularities, the Young equation (Equation 1.1) must be corrected to take into account these surface morphological features. The APCA on the real solid surface can be described through the Wenzel or Cassie-Baxter equations. A surface roughness factor (r) is introduced in the Wenzel equation in order to capture the effect of geometrical heterogeneity^{35,39}:

$$\cos \theta = r \cos \theta_Y \quad (1.2)$$

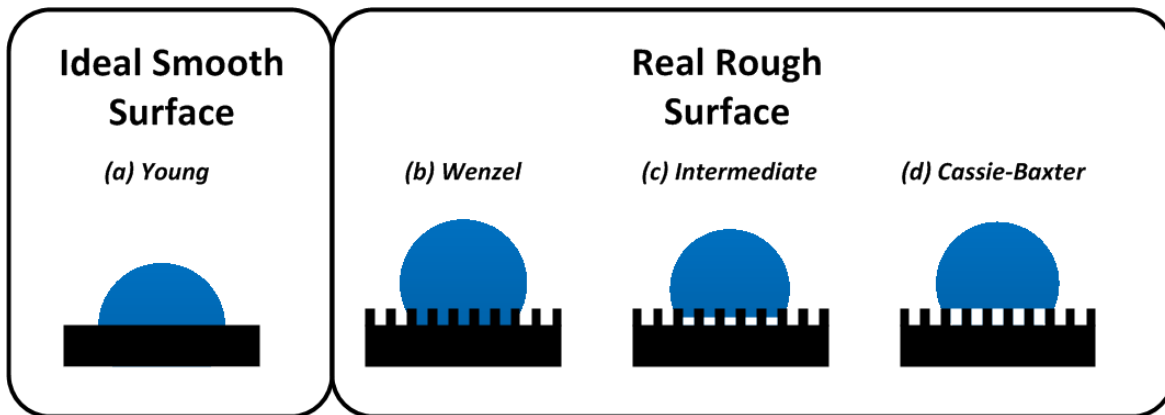


Figure 1.2: Schematic illustration of the effect of surface roughness on the wetting behaviour of solid surface: (a) Liquid droplet on an ideal smooth surface that can be described using the Young equation, (b) Droplet completely fills the grooves of rough surface (Wenzel state), (c) Droplet partially penetrates into the roughness features (Intermediate state between Wenzel and Cassie-Baxter regime), (d) Droplet sits on crests of rough patterns (Cassie-Baxter state).

Here, θ is the apparent contact angle corresponding to complete wetting of droplet (Figure 1.2 (b)), r is the surface roughness factor defined as the ratio of effective solid-liquid contact area to the projected (geometric) surface area, and θ_Y is the Young contact angle (YCA). Equation (1.2) implies that the surface roughness amplifies the inherent interaction between the solid surface and liquid droplet. If the contact angle of a smooth surface is less than 90° , the presence of surface roughness would accentuate the affinity to the water droplet. Therefore, the APCA of the rough surface will reduce further in comparison to the YCA of the same material. Similarly, for a smooth surface with an initial contact angle of $\theta > 90^\circ$, the existence of roughness feature would enhance the non-wetting characteristic, leading to an increase in the APCA. The use of the simple scaling factor r has nevertheless attracted criticism as the applicability of Wenzel equation is only restricted to moderate surface roughness. This is because the maximum attainable value of cosine function is one^{40,41}. It is suggested that beyond certain threshold roughness, air can be trapped between the solid surface and liquid phase, which is characterized as Cassie-Baxter wetting⁴². The Cassie-Baxter model describes the APCA with minimum Gibbs free energy on the rough surface based on the correlation between the surface structures and the intrinsic wettability as:

$$\cos \theta = f_s (\cos \theta_y + 1) - 1 \quad (1.3)$$

In Equation (1.3), θ corresponds to the apparent contact angle of the droplet that rests on the composite surface of solid and air while f_s is the fraction of solid in contact with the liquid phase. Equation (1.3) is a simplification of the original form of the Cassie-Baxter equation on a composite surface. The composite interface under the droplet consists of solid and air, where the air pockets are deemed as completely non-wetting, thus having a contact angle of 180° . A rigorous derivation of the equations above can be found elsewhere⁴²⁻⁴⁴.

1.2 Limitations of contact angle as wettability metric

Although the predictability of the APCA based on the Wenzel and the Cassie-Baxter equations (Section 1.1) may seem straightforward, experimental evaluation has shown significant deviations from the predicted values⁴⁵⁻⁴⁷. One of the reasons suggested in the literature for the deviation is that the above model equations average out the effect of roughness by assuming global considerations⁴⁸. Another emerging line of thought for the observed deviation is that the APCA is independent of the wetted area under the droplet and depends only on the three-phase contact line at the droplet periphery. The Wenzel and Cassie-Baxter models correlate the APCA to the wetted area under the droplet. Therefore, the deviations of the experimentally measured APCA cannot be corrected by improving the pre-existing models. The use of a contact angle as wettability metric is further complicated by the choice of droplet size in relation to the surface geometry and line tension effect^{49,50}. The following subsections outline three main aspects concerning the challenges in measurement and interpretation of contact angle.

1.2.1 Role of solid-liquid contact area and three-phase contact line

Based on a series of experiments on materials with a delicately-engineered center spot with distinct roughness and hydrophobicity, Gao and McCarthy claimed that only the interaction of solid and liquid at the three-phase contact line is important in dictating the contact angle value. Specifically, it is suggested that the solid-liquid interfacial area is essentially irrelevant⁴⁶. The similar proposition has also been asserted by Extrand⁴⁵, Öner and McCarthy⁵¹ as well as Bartell and Shepard⁵². Subsequently, the Wenzel and Cassie-Baxter wetting equations, which were developed based on the impression that wettability is dictated by interfacial free energies and the contact area between the liquid and solid phases, fail under these circumstances.

Nevertheless, there is lack of theory or predictive model that could relate either the geometry (shape, length or continuity) or chemical composition of the three-phase contact line to the magnitude of apparent contact angle (APCA) ⁵³.

Considering the three-phase contact line as the controlling aspect for the contact angle value itself generates a few complications for the rough surface characterization. The three-phase contact line can be described as the point where the liquid, solid and the gas phase co-exist. Depending on whether the droplet is in a Cassie-Baxter or a Wenzel wetting state, the three-phase contact line can exist at different locations at the periphery or even under the droplet ⁴⁸. When the liquid completely penetrates into the grooves as described by the Wenzel wetting configuration (Figure 1.3 (a)), change in the surface free energy and thus the droplet shape and contact angle can only be accomplished via a shift of the three-phase contact line, which in this case is similar to the droplet periphery. Therefore, it is obvious that the three-phase contact line does not exist under the droplet ⁴⁸. The situation of the Cassie-Baxter wetting where air bubbles are trapped underneath liquid in the grooves (Figure 1.3 (b)) is more complicated. Multiple three-phase contact lines actually exist: macroscopically observable *exterior* contact line represented by the droplet perimeter and *interior* three-phase contact line formed by interfaces of solid, suspended liquid and trapped air phase locally (Figure 1.3). Consequently, attainment of a stable contact angle can be achieved by minimization of surface free energy dictated by the *interior* contact line under the droplet through liquid penetration into the grooves. In contrast, movement of the *exterior* three-phase contact line via an increase in the projected droplet diameter can cause a change in the contact angle ⁴⁸. Penetration of liquid that is initially suspended on surface asperities into the surface features could potentially induce a transition from Cassie-Baxter to Wenzel wetting state and change in the solid-liquid interfacial area, as well as the apparent contact angle ⁴⁸. In summary, the droplet perimeter cannot be identified as the three-phase contact line. Instead, the *interior* contact lines under the droplet should be considered in addition to the *exterior* three-phase contact line at the droplet perimeter ^{48,53}.

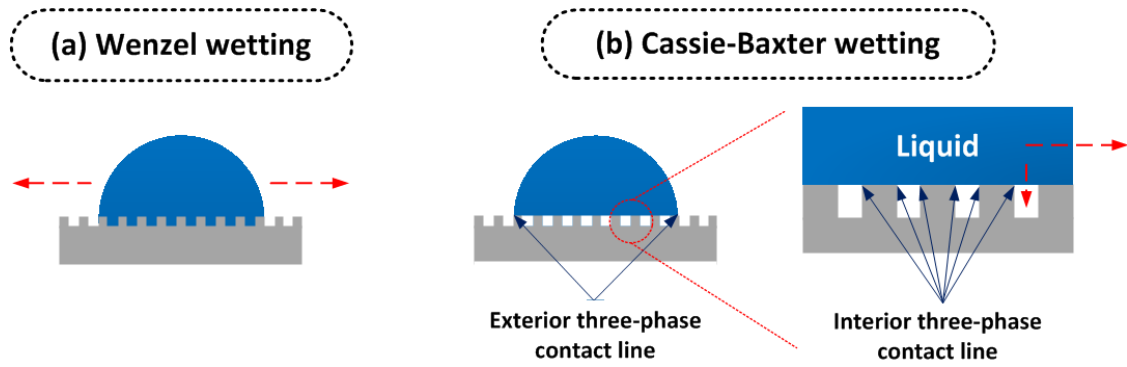


Figure 1.3: Schematic illustration of the existence of exterior and interior three-phase contact line for Wenzel and Cassie-Baxter wetting configurations. The red dotted arrow represents the possible direction of droplet movement in response to the supply of external energy.

In fact, the relevance of both the contact line and interfacial area in governing the contact angle value has been addressed by Marmur and Bittoun by evaluating the assumption of the Wenzel and Cassie-Baxter models. Based on a series of numerical examples, it is shown that both interactions at the three-phase contact line and solid-liquid interfacial area are equally important⁵⁴. The actual contact angle along the contact line must match the local Young contact angle to satisfy the thermodynamic requirement. However, there are many metastable contact angles that fulfill this condition. It is claimed that the attainment of the most stable contact angle is governed by the surface properties of the wetted area⁵⁴. Specifically, it is suggested that the Wenzel and Cassie-Baxter equations are originally formulated by defining a hypothetical surface with average properties representative of the original surface features. Replacement of the real surface with an equivalent ideal surface with single Gibbs energy minimum allows the determination of the most stable energy state which is otherwise impossible^{54,55}. Thus the use of a larger droplet would minimize the effect of surface heterogeneity, in conformity to the averaging approach adopted in Wenzel and Cassie-Baxter wetting models. In turn, this requirement for larger droplet size in obtaining the most stable contact angle is claimed to be the illustration of the significance of the contact area. Therefore, the local and global equilibrium conditions at the three-phase contact line and the interfacial area, respectively, must be considered together⁵⁴.

1.2.2 The multiplicity of contact angle values on the rough surface

Contrary to the case of an ideal surface with single Gibbs free energy minimum, the Gibbs energy curve of a real surface possesses multiple minima points corresponding to many possible metastable equilibrium states, as depicted in Figure 1.4^{11,56}. Presence of multiplicity of Gibbs energy minima for a rough solid surface is a consequence of the variation in the local microscopic properties of the solid surface. These microscopic variations can arise from the surface roughness or chemical heterogeneity. On a microscopic scale, this leads to the formation of different actual contact angles (ACCAs) at each surface site at the periphery of the droplet. A local energy minimum exists when the droplet satisfies both the thermodynamics and the geometric considerations. In order to achieve either the metastable or the most stable state, two thermodynamics conditions must be fulfilled: firstly the *local* actual contact angle (ACCA) must match the Young contact angle (YCA), and secondly the local mean curvature of the droplet must conform to the local pressure difference across the liquid-air interface (ΔP), as described by the Young-Laplace equation^{25,54,57,58}:

$$\Delta P = \gamma_{LV} \left(\frac{1}{R_1} + \frac{1}{R_2} \right) \quad (1.4)$$

In the above expression, R_1 and R_2 are the two principal radii of curvature of the droplet. In addition, the droplet shape must also conform to the geometrical constraint of constant volume, which imposes a relationship between the droplet radius, location of contact line and the apparent contact angle. Theoretically, a droplet could exist at any of the metastable states (Figure 1.4) at which the thermodynamics and geometric criteria are simultaneously satisfied, leading to the multiplicity of the apparent contact angle (APCA)^{11,54,59}. Therefore, in contrary to the unique Young contact angle of the ideal surface, the APCA of the rough surface cannot be uniquely determined. Instead, the value lies between a maximum and minimum value known as the advancing (ACA) and receding contact angle (RCA). Non-singularity of the contact angle values poses a challenge in using the contact angle values for estimating the relative wettability of rough surfaces.

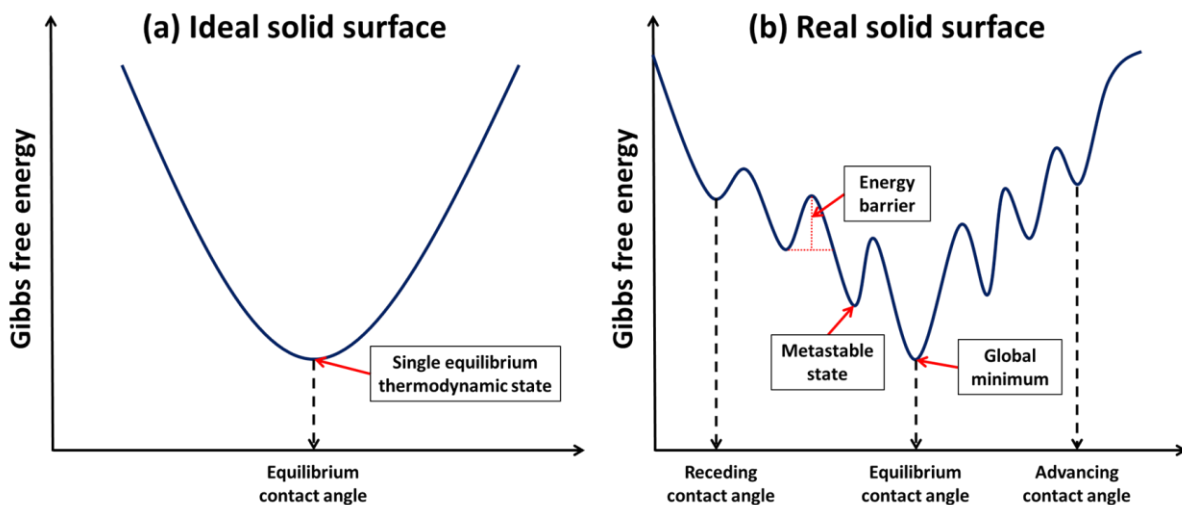


Figure 1.4: Gibbs energy profile of (a) an ideal solid surface and (b) a real (rough) solid surface in relation to the contact angle value.

The existence of multiple thermodynamic states could give rise to the measurement of contact angle values that fail to reflect the representative surface features under the droplet and the effective surface wetting properties. At a metastable state, the system is essentially trapped in a local minimum state imposed by the energy barriers that hinder it from reaching the global minimum energy state⁶⁰. The droplet is pinned to the surface defects due to resistance imposed by the surface structure and/or chemical heterogeneity. External energy is required for the system to overcome the energy barrier and to transit the droplet from one metastable energy states to another. Various approaches have been reported in the literature to provide the additional energy for inducing the transition between thermodynamic states, such as mechanical, thermal or electrical energy^{40,61–64}. From a practical point of view, determination of the amount of energy required to attain the global minimum energy state can be quite challenging. Moreover, the global Gibbs energy minimum state is not readily recognizable experimentally⁶⁵.

Wolansky and Marmur have mathematically shown that a droplet at the state of global energy minimum should be symmetrical. Accordingly, present best practice in measuring contact angle is to ensure that the droplet is axisymmetric^{25,39}. However, the presence of symmetrical droplet is a necessary but not sufficient condition to ensure that the system is at a global-minimum wetting state. It is also worth mentioning that while a droplet on a rough surface may reveal a seemingly circular shape on a macroscopic scale, there will always be a certain degree

of local deformations due to slight inclination of surface defects^{58,66}, as depicted schematically in Figure 1.5.

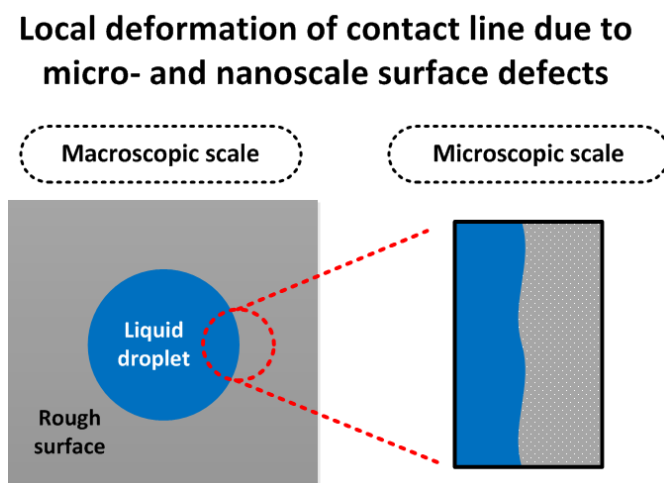


Figure 1.5: Local deformation of the three-phase contact line as a result of surface defects leading to asymmetric droplet shape.

The symmetry of droplet should rather be perceived as a prerequisite for proper contact angle measurement since the evaluation of contact angle from an asymmetric droplet is not meaningful. The reason is that the measured apparent contact angle of a distorted droplet would vary with each angle of observation²⁵. It has been proposed that in addition to taking a side-view image of the droplet, a top-view picture should also be captured to ensure droplet symmetry¹¹. The use of a larger droplet is also favourable in attaining the desired symmetrical shape as the effect associated with surface roughness and chemical heterogeneity would be minimized^{11,39,48,67}. It has been showed that a droplet resembles closer to the spherical cap shape with more circular contact line when a larger droplet size is used because the increase in droplet volume minimizes the corrugation of contact line at local scale^{67,68}. The higher internal energy possessed by a larger droplet would also facilitate movement past the energy barrier towards the global energy minimum state⁶⁸. Additionally, another study on the effect of droplet size showed that the Wenzel and Cassie-Baxter equations used for the interpretation of the contact angle give better predictions when the droplet size is larger by several orders of magnitude in comparison to the scale of surface roughness or heterogeneity³⁹. In other words, the experimentally measured contact angle would approach the value predicted by Wenzel and Cassie-Baxter wetting models when a larger droplet volume is used (Figure 1.6).

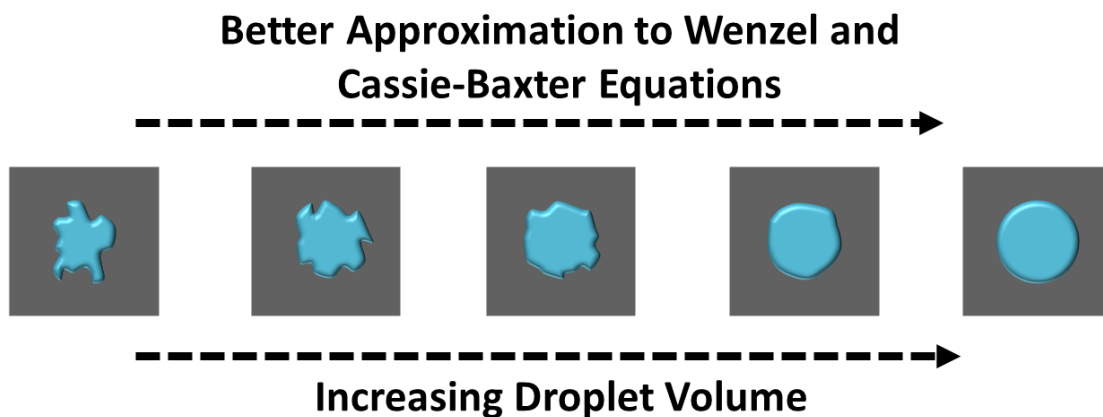


Figure 1.6: Schematic illustration of the effect of droplet volume on the droplet symmetry and approximation to Wenzel and Cassie-Baxter equations for the rough solid surface. As the droplet size increases relative to the scale of surface heterogeneity, an approximation of the Wenzel and Cassie-Baxter models to the most stable contact angle improves. The corrugation of the contact line is exaggerated for illustration purpose.

The requirement on droplet volume described above, however, leads to an interesting complication concerning the ideal droplet size for comparison of surface wettability between different materials. Given the plethora of surface roughness parameters that have been used in evaluating surface geometry, the selection of proper roughness scale is also not trivial⁶⁹. The line tension effect dominates when the droplet size is very small^{25,70-72}. On the other hand, the gravitational effect becomes more predominant with a larger droplet, resulting in distortion of the droplet shape⁷³. Moreover, restriction on the ratio of droplet size to surface roughness scale would impose a certain degree of technical complexity since the type and size of samples that could be analyzed is limited⁷³.

1.2.3 Droplet size dependence of contact angle

The Young equation implies that the contact angle is only dependent on the surface tensions of the constituting solid, liquid and air phases, but not the mass or volume of liquid used in the measurement⁵⁷. In other words, the contact angle should ideally be an intensive quantity. Nevertheless, experimental evidence in the literature reveals a wide range of contact angles in chemically similar systems when different droplet volumes are employed^{50,74,75}. A possible explanation is that the derivation of Young equation entails many simplifications, including the assumption of perfectly smooth and homogeneous surface as well as exclusion of the effect of molecular interactions at the three-phase contact line^{57,72}. In order to account for the effect of droplet size, the concept of line tension has been introduced, leading to a modified form of Young model as shown in Equation (1.5) and (1.6)^{57,76–84}:

$$\cos \theta = \cos \theta_{\infty} - \frac{\tau}{\gamma_{LV}} \frac{1}{R} \quad (1.5)$$

$$\cos \theta_{\infty} = \frac{\gamma_{SV} - \gamma_{SL}}{\gamma_{LV}} \quad (1.6)$$

τ is the line tension, R is the radius of the three-phase contact line, θ is the experimentally measured contact angle of finite droplet volume, and θ_{∞} is the contact angle corresponding to an infinitely large droplet. Equation (1.5) is a simplified case for the ideal solid surface at which the three-phase contact line corresponds to a perfect circle. In other cases, the term $\frac{1}{R}$ has to be replaced by the appropriate radius of curvature of the contact line. When the contact line radius is infinitely large, Equation (1.5) implies that the contact angle would reduce to equilibrium contact angle predicted by the classical Young equation (Equation (1.6))²⁷.

Line tension can be perceived as a manifestation of an imbalance of different intermolecular interactions experienced by the molecules in the vicinity of the three-phase contact line. Depending on the type of systems, intermolecular forces that could exist include the van der Waals, electrostatic, solvation and steric forces^{20,85,86}. In an analogy to the surface tension, the line tension is defined either as the specific free energy (per unit length) of the three-phase contact line or as the force acting at the three-phase line^{21,57,87,88}. As seen in Equation

(1.5), the slope of $\cos \theta$ against $\frac{1}{R}$ depends only on the sign of line tension since the surface tension of the liquid phase is always positive. If the line tension is positive, the linear plot of $\cos \theta$ to $\frac{1}{R}$ would exhibit a negative slope, signifying a decrease of the contact angle with increasing radius of contact line, or equivalently droplet volume. A negligible line tension would imply a constant contact angle with droplet volume. In contrast, the slope of $\cos \theta$ to $\frac{1}{R}$ would be positive and the contact angle would increase with increasing droplet volume when the line tension is negative⁵⁷.

Different signs and orders of magnitude of line tension have been reported in both theoretical and experimental observations²⁰. Typical line tension values are in the range of 10^{-11} and 10^{-5} J m^{-1} with both positive and negative signs^{20,75,89}. Although there is lack of agreement on the sign and magnitude of line tension, many attempts have been made to explain the trends in contact angle relative to the droplet volume using the concept of line tension. Figure 1.7 summarizes three possible trends of change in contact angle with increasing droplet volume that have been observed experimentally. As the droplet size increases, the macroscopic contact angle can either decrease, increase or even remains constant, corresponding to positive, negative and insignificant line tension effect, respectively^{57,21}.

It has been suggested that the controversy over the sign and magnitude of the line tension might be partially caused by artifacts in the experimental approach (sample preparation), misinterpretation of the mathematical models as well as inappropriate comparison between systems with different geometries^{20,21,90,91}. Despite extensive studies on the subject, it is unclear whether the size-dependent wettability can be sufficiently described using the line tension concept as the value and sign of line tension remains a subject of controversy⁹². However, it is noteworthy that the line tension effect is only prevalent for an extremely small droplet in the size of nanometer range. This is because the influence of line tension at contact line becomes more important than the surface tension effect at such small scale. Therefore it is almost negligible for practical measurement of contact angle in most applications^{11,54,72,93-97}.

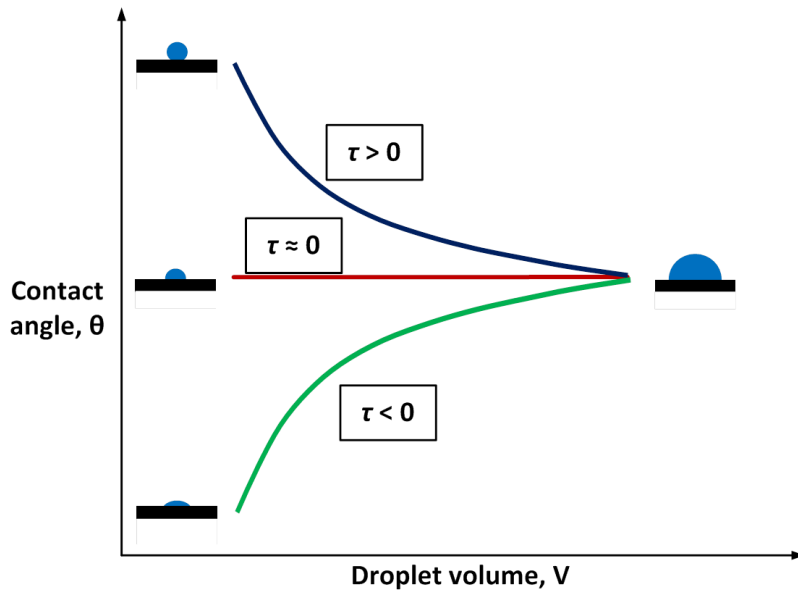


Figure 1.7: Summary of observed trends of the contact angle with increasing droplet volume in the literature. The droplet size dependence of the contact angle has been explained using the line tension (τ) effect.

1.3 Surface wetting control

Biological organisms in nature exhibit unique surface wettability in order to adapt to their living environment. A diverse range of wettability can be observed, ranging from the low-adhesion superhydrophobic lotus leaf with the self-cleaning property, high-adhesion superhydrophobic gecko foot, to the in-air superhydrophilic and underwater superoleophobic fish scale. Inspired by these natural systems with superwetting/anti-wetting properties, significant efforts have been devoted to fabricating artificial surfaces with different wettabilities by engineering the surface microstructure and chemical composition. Functional materials with distinct wetting properties have been fabricated through chemical vapour deposition, electrospinning, femtosecond laser micromachining, plasma treatment, lithography and so on. This approach of tailoring the surface chemistry and morphology represents a passive means for tuning the material wettability. The static nature of these modifications prevents the surfaces to alter the wettability in response to their environment. In fact, active control over the surface wettability is highly desirable in applications including microfluidic devices, sensors, tunable optical lenses, and smart membranes. A number of stimuli-responsive materials featuring dynamic and reversible wettability alteration upon stimulation have been designed. Driven by external stimuli such as pH, temperature, solvent, electric potential, and light, the smart surfaces can switch between two opposing wetting states of superhydrophobicity and superhydrophilicity in a reversible manner.

1.3.1 Passive wettability control through surface chemistry and structure modification

It has been established that surface wettability of a solid substrate is governed by both the surface energy and geometrical structure⁹⁸. Thus the design of artificial wetting systems has been revolved around either modifying the surface chemistry, morphology, or both^{99,100}. The chemical composition dictates the intrinsic wettability of the surface as described by the Young contact angle (YCA). However, the highest contact angle reported to date for surface obtained through chemical modification alone is only about 120°^{101,102}. In fact, both Cassie-Baxter and Wenzel equations suggest that geometrical configuration is a key factor governing the surface wetting properties. Several studies have demonstrated that superhydrophobic behaviour can not only be generated on the intrinsically hydrophobic surface, but also on the hydrophilic surface by

creating sufficient roughness such that the solid-liquid interface is minimized ¹⁰³. Correlating the surface structure and wetting properties, numerous design principles and the role of geometrical parameters have been proposed to guide the fabrication of superwetting and anti-wetting materials ¹⁰⁴. Marmur claimed that the convex roughness feature is favourable over the concave roughness in trapping the air pockets to form the Cassie-Baxter state ⁵⁵. Another study showed that the presence of re-entrant topography induces a negative Laplace pressure difference due to trapped air within the surface roughness, which helps to stabilize the surface superhydrophobicity ^{105,106}. The durability of the superhydrophobic surface can also be increased by creating a hierarchical structure with multi-scale roughness in the range of micro- and nanometer ¹⁰⁷. The multiplicity of roughness scale improves the resistance against water penetration into the roughness features, thus endowing the surface with higher mechanical stability than single-scale roughness surface ¹⁰⁸⁻¹¹⁰. Although the hierarchical architectures is not a prerequisite for superhydrophobicity, it reduces the aspect ratio of the macroscale structure necessary to achieve the Cassie-Baxter state ^{101,108}. Based on these structure-property relationships, various synthesis routes have been adopted.

The fabrication techniques that have been employed in the preparation of artificial surfaces with superwettability can be categorized into the top-down or bottom-up approaches. The top-down synthesis methods involve a restructuring of bulk materials in the form of etching, templating, lithography, micromachining, and plasma treatment ¹¹¹. In the bottom-up approaches, smaller building blocks are integrated into a more complex object through self-assembly. Examples include chemical synthesis, electrochemical deposition, electrospinning, layer-by-layer deposition, colloidal assembly, and sol-gel method ^{103,112}. Compared to the top-down approaches, the bottom-up methods allow a higher degree of control over the molecular arrangement and chemical composition ¹¹². The electrochemical deposition method is particularly attractive due to its high controllability, scalability, reproducibility, and implementation simplicity. Fine control of the material properties can be achieved by simply adjusting the deposition parameters, such as the electrolyte composition, applied potential or current density, deposition time, temperature, and pH ¹¹³. A variety of surface morphologies have been synthesized using the electrodeposition technique, including rods, fibres, needles, dendrites, and flower-like structures ^{111,114-119}.

1.3.2 Active wettability control on the stimuli-responsive surface

In contrast to the static wetting properties induced by structural and chemical modifications, smart surfaces with dynamically switchable and reversible wetting properties offer much flexibility and versatility. The dynamic change in the wetting behaviour is usually triggered by an external stimulus within a short time period. The external stimulus causes a change in the surface structure or chemical composition, which leads to an alteration in the surface wettability^{120–122}. Such on-demand wetting alteration finds numerous technological applications such as self-cleaning surfaces, microfluidic tools, tunable optical lenses, lab-on-a-chip systems, smart membranes, and corrosion platforms^{123–127}. Various external stimuli have been used to achieve the wettability alteration, including pH^{128,129}, temperature^{130,131}, light irradiation^{132,133}, solvent treatment^{134,135} and electric field^{136,137}. Table 1.1 gives an overview of the wetting switching techniques that have been reported in recent years. Among the various wettability alteration approaches, the electric field stimulation has the advantages of real-time response, fast switching, and high stability¹³⁸. The electric potential-assisted wettability control can be realized by a conformational change of functional molecules, charge accumulation at the solid-liquid interface (electrowetting), and redox reaction induced chemical change³⁸. For biological applications that could be susceptible to drastic chemical, electrical, UV, or heat stimulations, wettability regulation actuated by mechanical force is favourable¹³⁹. By manipulating the morphological features of elastic material by mechanical strain, dynamic tuning of the adhesion and wetting properties can be achieved^{140–143}.

As illustrated in Table 1.1, a number of the stimuli-responsive surfaces entail the use of tedious preparation steps and chemical additives to acquire the surface chemistry and structure essential for the superwetting-anti-wetting properties. In addition, some of the wettability transitions require extreme conditions such as high voltage, special light sources and corrosive solvents^{144,145}. The range of CA transition and switching speed also remains an important topic of research. From a practical perspective, a few key features are required to extend the applicability of the material, including a wide range of achievable contact angles, fast response time, and a stable intermediate wetting state. In this context, the use of redox reactions in stimulating the wetting transitions is particularly attractive. Wetting alterations mediated via redox reactions demand much lower potentials than those required for electrowetting and

therefore they are more versatile and efficient approaches to achieve smart wetting alteration^{146,147}.

The design of the electrochemical technique depends on the base material and therefore different mechanistic approaches are involved. Various electrochemical approaches reported in the literature include the use of conformational re-orientation of polyelectrolytes¹⁴⁸, oxidation or reduction of conductive polymers^{149,150}, intercalation and de-intercalation of ionic species^{151,152}, attachment of oxygen functional groups for carbon nanotube arrays¹⁵³ and addition of chemical dopant or grafting of redox molecules^{154,155}. Recently, the low voltage has been used to facilitate electrowetting without any electrochemical reactions following the accumulation of charges at the interfaces. The basic requirement for low-voltage electrowetting involves using a material with low intrinsic electroactivity such as steel, gold and graphite^{156–158}. The potential required for such electrowetting process is on par with that of the electrochemical process. For example, the wetting transition was reversible for the gold surface at < 0.7 V¹⁵⁶, the steel surface showed an irreversible transition using 1.5 V¹⁵⁷, and electrowetting on the graphitic surface was observed at a voltage of approximately 1.5 V¹⁵⁸.

One specific group of stimuli-responsive material that has been extensively investigated is the inorganic-oxide based material^{120,159–162}. Generally, planar metallic and metal oxide surfaces possess high surface energy and hence low contact angle (CA)¹⁵⁹. However, upon modifying their surface morphology or treating with low surface energy compounds^{163–165}, superhydrophobic properties can be achieved. Due to its abundance, low cost and ease of synthesis in several nanoscale topologies, copper and its oxides have attracted much interest for the preparation of the superhydrophobic surfaces¹⁶⁶, electrochemical sensors¹⁶⁷, energy storage materials¹⁶⁸ and photo-electrochemical water reduction catalysts¹⁶⁹. Different oxidation states of copper show distinct intrinsic wetting properties. The metallic Cu is hydrophilic with CA of approximately 78° while the cuprous oxide (Cu₂O) and cupric oxide (CuO) display hydrophobic and hydrophilic character with CA of about 100° and 20°, respectively^{159,170,171}. The commonly observed copper oxide, Cu₂O is formed when Cu gets oxidized¹⁷² or CuO undergoes de-oxidization during prolonged exposure to ambient air¹⁵⁹. The replacement of surface hydroxyl groups by oxygen during air exposure has also been attributed to the de-oxidization of CuO to Cu₂O¹⁷³. The opposing wetting properties of these two copper oxides make them suitable

candidates for developing materials with tunable wettability without additional low surface energy reagents. Copper oxide based surfaces with reversibly switchable wettability under external stimuli without the addition of chemical reagent have been reported in the literature ^{120,159,163,173}.

The dynamic wetting alteration for the copper oxides has been demonstrated with various forms of external stimuli, including heat, ultraviolet (UV)-radiation and X-rays. Lee et al. induced structural and compositional changes to a copper substrate by oxidizing and reducing the copper surface at different temperatures ¹⁷⁰. In their study, the outermost surface layer was dominantly composed of Cu₂O which along with the surface modifications led to different levels of hydrophobic behaviour. Chang et al. showed the use of annealing temperature to attain CuO surface with contrasting wetting characters. The authors showed that the CuO surface becomes hydrophobic by annealing at 100°C, but the surface is hydrophilic when annealed at 350°C in air ¹⁵⁹. The surface hydrophobicity is achieved via surface oxidation and annealing at 100°C in air in order to promote the transformation of the hydrophilic CuO phase to Cu₂O dominant phase with hydrophobic property ¹⁵⁹. Pei et.al reported the switchable wettability of CuO during repetitive exposure to UV and dark storage for creating hydrophilic and hydrophobic surfaces, respectively ¹⁷³. The author used UV exposure time of 4 hours and dark storage of 2 weeks in the study. Kwon et al. showed that the X-ray irradiation modifies the wettability of inorganic substrates including CuO to a superhydrophilic behaviour within a time period of fewer than 10 minutes ¹²⁰.

Table 1.1: Overview of the wettability switching techniques reported in the literature

Stimulus	Synthesis method	Material	Change in water CA	Switching speed	Reference
Temperature (25 to 40°C)	<ul style="list-style-type: none"> • Polymerization 	Poly(N-isopropylacrylamide) (PNIPAAm) film	149.3 to 0°	Several minutes	Sun et al. ¹⁷⁴
pH (1 to 13)	<ul style="list-style-type: none"> • Electrodeposition • Thiol modification 	Thiol-coated gold surface	154 to 0°	Several seconds	Yu et al. ¹²⁸
Mechanical force	<ul style="list-style-type: none"> • Commercial film 	Polyamide film	151 to 0°	-	Zhang et al. ¹⁷⁵
Electric potential (~0.8 V)	<ul style="list-style-type: none"> • Thermal treatment • Surface grafting 	Ferrocene modified TiO ₂ nanotube	115 to 65°	2 min	Schmidt-Stein et al. ¹⁷⁶
O ₂ plasma treatment / dark storage	<ul style="list-style-type: none"> • Solvent oxidation 	CuO / Cu(OH) ₂	159 to 0°	3 min plasma / 72-hour dark storage	Chaudhary et al. ¹⁷⁷
Thiol modification/air annealing	<ul style="list-style-type: none"> • Etching • Electrodeposition • Thiol modification 	CuO film	165 to 0°	10 to 30 min	Wang et al. ¹⁷⁸
Cl ⁻ and PFO ⁻ counterion exchange	<ul style="list-style-type: none"> • Solution immersion • Plasma treatment • Polymerization 	Polyelectrolyte-tethered transparent glass surface	164 to 3°	5 min	Hua et al. ¹⁷⁹
UV irradiation / dark storage	<ul style="list-style-type: none"> • DC reactive magnetron sputtering 	TiO ₂ film	110 to 0°	30 min UV / 1-week dark storage	Zheng et al. ¹⁸⁰
H ₂ O ₂ oxidation / vacuum deoxidation	<ul style="list-style-type: none"> • H₂O₂ solution dipping 	CuO film	150 to 5°	8 hour	Tu et al. ¹⁷¹
Electric potential (10 V)	<ul style="list-style-type: none"> • Chemical bath deposition 	N-dodecyltrimethoxysilane (KH1231)- modified copper foam	154 to 0°	20 min	Lin et al. ¹⁵⁵
CO ₂ / N ₂ treatment	<ul style="list-style-type: none"> • Polymerization • Electrospinning 	PMMA-co-PDEAEMA nanofibrous membrane	140 to 36°	15 min	Che et al. ¹⁸¹

Stimulus	Synthesis method	Material	Change in water CA	Switching speed	Reference
pH (3 to 12)	<ul style="list-style-type: none"> Anodic oxidation Gold layer spraying Thiols modification 	Aluminum alloy	160 to 0°	-	Liu et al. ¹⁸²
H ₂ / O ₂ gas annealing	<ul style="list-style-type: none"> Chemical vapour deposition 	ZnO nanowires	153.5 to 0°	60 to 90 min	Yadav et al. ¹⁸³
Temperature (25 to 40°C)	<ul style="list-style-type: none"> Electrospinning 	Poly-N-(isopropyl acrylamide) (PNIPAM) and poly-(vinylidene fluoride) (PVDF) blend membranes	136 to 5°	Several seconds	Ranganath et al. ¹⁸⁴
UV-vis irradiation / dark storage	<ul style="list-style-type: none"> Hydrothermal Spin coating Stearic acid modification 	Bismuth-based micro/nanomaterial	163 to 10°	5-80 min UV-vis / 3-26 day dark storage	Yang et al. ¹⁸⁵
H ₂ O ₂ oxidation/vacuum drying	<ul style="list-style-type: none"> Hydrazine hydrate-assisted chemical reduction 	Copper surface	150 to 0°	1 min H ₂ O ₂ oxidation / 1-hour vacuum drying	Yang et al. ¹⁸⁶
O ₂ plasma treatment/heat treatment	<ul style="list-style-type: none"> Redox etching Chemical precipitation 	FeNiO _x (OH) _y -coated nickel mesh	153 to 0°	2 min plasma / 3-hour heat treatment	Zhou et al. ¹⁸⁷
Electric potential (2.5 to 35 V)	<ul style="list-style-type: none"> Chemical vapour deposition Annealing 	Super-aligned carbon nanotube (SACNT)	156 to 20°	-	Zhang et al. ¹⁸⁸
Annealing (150 and 400°C)	<ul style="list-style-type: none"> Chemical bath deposition Annealing 	ZnO surface	164 to 0°	30 min to 6 hour	Velayi ¹⁸⁹
Electric potential (< 1.5 V) / air drying	<ul style="list-style-type: none"> Electrodeposition 	Cu/Cu_xO surface	160.8 to 10°	Several seconds to minutes of voltage / 1 hour air drying	Present study _{190,191}

2 Motivation and research objectives

2.1 Objectives

Although the sessile-drop contact angle measurement has been widely used as a tool to characterize surface wettability due to its simplicity, interpretation of the results can be challenging, as discussed in Section 1.2. A robust wettability characterization method is required to enable a thorough understanding of the effect of geometrical parameter and surface chemistry on the wetting behaviour. As shown in Section 1.3, such structure-property-function relationship will establish a set of design criteria in the development of functional surfaces with special wettabilities. In order to realize the full potential of smart interfacial materials with superwettability, several aspects need to be improved, including the material cost, fabrication method, wetting switching condition, the range of contact angle transition, switching speed, and durability.

The focus of this thesis work was thus to develop a new wettability characterization technique to overcome the limitations of the optical method and to design a simple approach for fast and reversible wetting switching on the stimulus-responsive surface. The specific objectives are outlined as follows:

- 1) Development of electrochemical wettability characterization technique
 - To design an electrochemical testing platform for characterizing the wetting behaviour of the surface with a regular and irregular roughness
 - To devise a new wettability metric to overcome the limitations of contact angle
 - To investigate the effect of testing parameters on the electrochemical wettability metric, e.g. electrolyte composition, scan rate
- 2) Development of electrochemical wettability switching method
 - To identify a low-cost, simple and fast route for in-situ wettability alteration
 - To investigate the effect of applied potential magnitude and duration on the wetting switching
 - To investigate the reversibility of the wettability transition
 - To investigate the wetting switching mechanism
 - To explore and demonstrate the relevant application of the tunable wettability

2.2 Thesis layout

This thesis is organized into five chapters. Figure 2.1 is a schematic layout of this thesis depicting the approaches taken to meet the objectives.

- **Chapter 1** provides an overview of the surface wetting theories highlighting the challenges in using contact angle for wettability characterization. The typical approaches employed for controlling the surface wettability are presented. The challenges and opportunities in using the stimuli-responsive materials with switchable wettability are also discussed.
- **Chapter 2** presents the objectives of this thesis work along with a layout illustrating the thesis organization.
- **Chapter 3** describes the use of an electrochemical approach for characterization of surface wetting behaviour. An electrochemical-based wettability metric is proposed and evaluated based on a series of experiments on rough surfaces. The robustness of the electrochemical technique is compared against the standard wetting measurement tool, namely the static contact angle. The results were analyzed based on the Wenzel and Cassie-Baxter wetting models.
- **Chapter 4** presents an electrochemical wettability control technique based on manipulation of the surface oxidation state. The wetting alteration mechanism was investigated using a combination of physical characterization techniques and electrochemical analysis. The wetting switching feature was also demonstrated for on-demand separation of oil-water mixtures.
- **Chapter 5** summarizes the research outcomes and significance, conclusions and recommendations for future work.

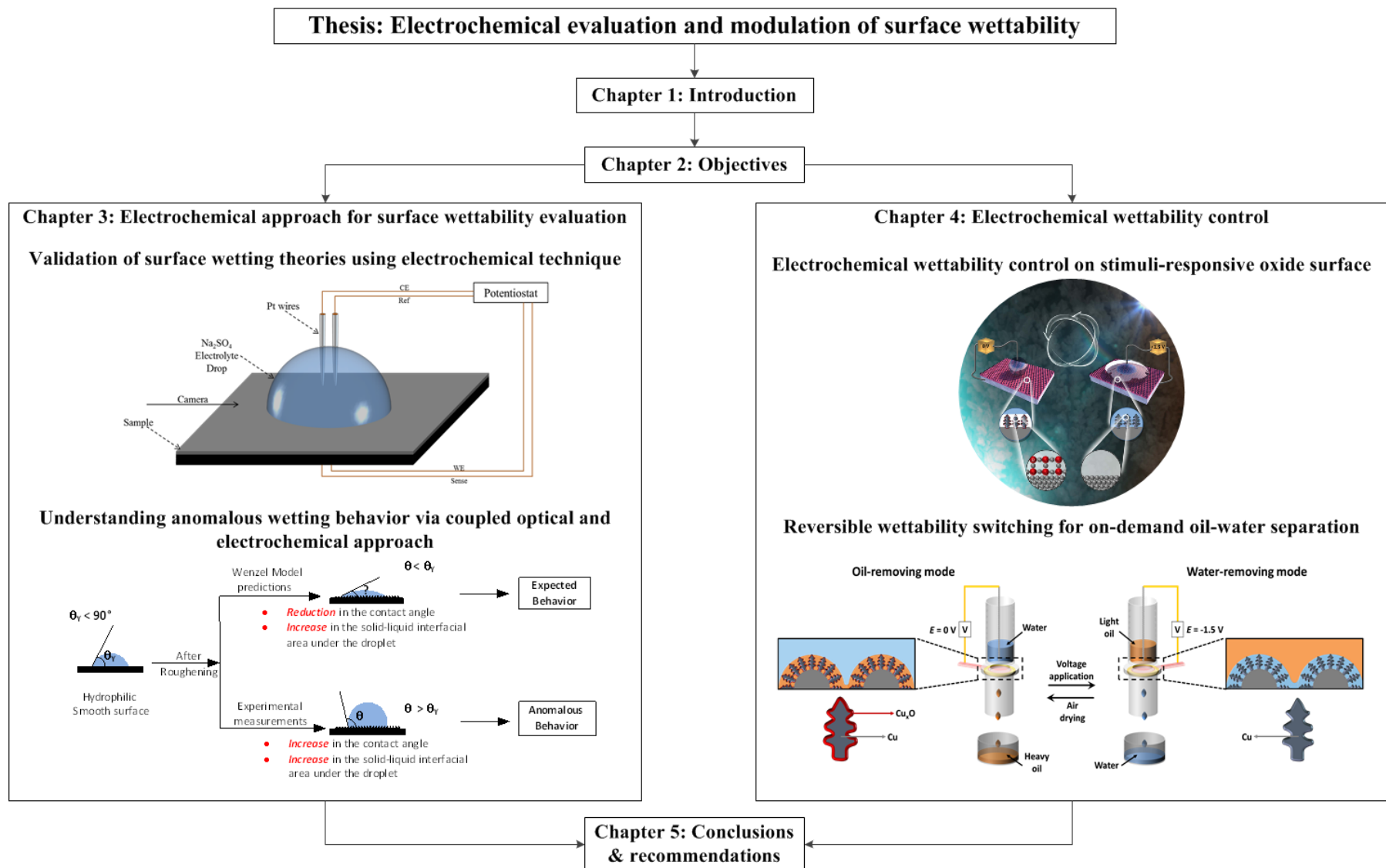


Figure 2.1: Thesis layout

3 Electrochemical approach for surface wettability evaluation

3.1 Introduction

Conventionally, the contact angle is used as a metric for quantitative evaluation of the surface wettability. The apparent contact angle of a droplet placed on a rough surface differs from that on a smooth surface and it depends on the type of solid-liquid (S-L) interface under the droplet. For a rough surface, there are two possible wetting mechanisms. In the first case, the liquid can penetrate into the roughness features forming a fully wetted homogeneous interface under the droplet. In another scenario, the liquid phase can stay suspended on the roughness asperities leading to a composite solid-liquid-air interface. The presence of surface roughness changes the S-L interfacial interaction, which dictates the effective interfacial area beneath the droplet. Subsequently, the variation in the interfacial area and wetting state affect the apparent contact angle. In order to predict the roughness induced change in the contact angle, various theoretical formulations have been developed. The two most widely used models are the Wenzel (Equation (1.2)) and the Cassie-Baxter (Equation (1.3)) equations that are described in Section 1.1. The objective is to predict the apparent contact angle (θ) for a rough surface as a function of the Young contact angle (θ_Y). The vast majority of these models involve a direct or an indirect correlation between three important parameters: θ , θ_Y and the solid-liquid (S-L) interfacial area under the droplet. While the optical evaluation procedure for the contact angle is well established, estimating the wetted interfacial area poses problems primarily due to the limited optical accessibility.

Despite extensive applications of the Cassie-Baxter³⁶ and Wenzel³⁵ models in the literature, there has been a long-standing debate regarding the validity of the models and their range of applicability^{46,192}. The influence of droplet volume during the measurement of wettability parameters has also shown some contradictory results¹⁹³. A quantitative evaluation of the wetted area could provide additional insights into addressing these issues. Moreover, identifying the appropriate model to represent the wetting behaviour based on the optically measurable θ and θ_Y values can be challenging. For example, when the substrate is intrinsically hydrophobic, both the Cassie-Baxter model and the Wenzel model predict an increase in the contact angle with roughness^{22,37}. Understanding the dynamic behaviour of the droplet on

hydrophobic surfaces is also an important field that can benefit from the accurate measurement of solid-liquid (S-L) interfacial area^{194,195}.

Model systems with the patterned roughness of known dimensions for approximating the S-L interfacial area have been used to circumvent these problems^{192,196,197}. However, even for the patterned roughness, the liquid meniscus under the droplet can behave differently depending on the geometry, leading to inaccuracies in the predicted values¹⁹⁷⁻¹⁹⁹. Additionally, the approximations based on a pattern cannot be extended for the surface with irregular roughness features due to the stochastic nature of the surface topologies²⁰⁰.

This chapter describes the development of an experimental approach to overcome the limitations in the contact angle measurement. The proposed method evaluates the parameters θ , θ_Y and S-L interfacial area using a combination of optical and electrochemical measurements. Figure 3.1 highlights two shortcomings associated with the use of contact angle for surface wettability characterization. These two aspects entailing the ineffectiveness of the contact angle in capturing the roughness effect are used to demonstrate the capability of the electrochemical approach. We have shown that the limitations of the conventionally used optical method can be overcome by the electrochemical measurement of the double layer capacitance of the surface. In particular, the proportionality between the electrochemical double layer capacitance and the S-L interfacial area is used to determine the wettability of rough surfaces. Through a quantitative comparison of the model predictions with the experimental results, we identified the model which best describes the wetting behaviour. The applicability of the electrochemical double layer capacitance as a wettability metric was illustrated on carbon surfaces with regular (plasma treatment) and irregular (mechanically polishing) roughness. Previous studies showed that relative scale of the roughness with respect to the double layer thickness and the mass transport rates within the nano-pores could affect the capacitance measurement²⁰¹⁻²⁰³. The impact of these roughness-induced phenomena on the electrochemical wettability measurement has also been systematically studied in present work. By enabling the study of surface structures with a stochastic distribution, the electrochemical technique has the potential to be used in complementary to the optical method to advance the understanding of wetting phenomena.

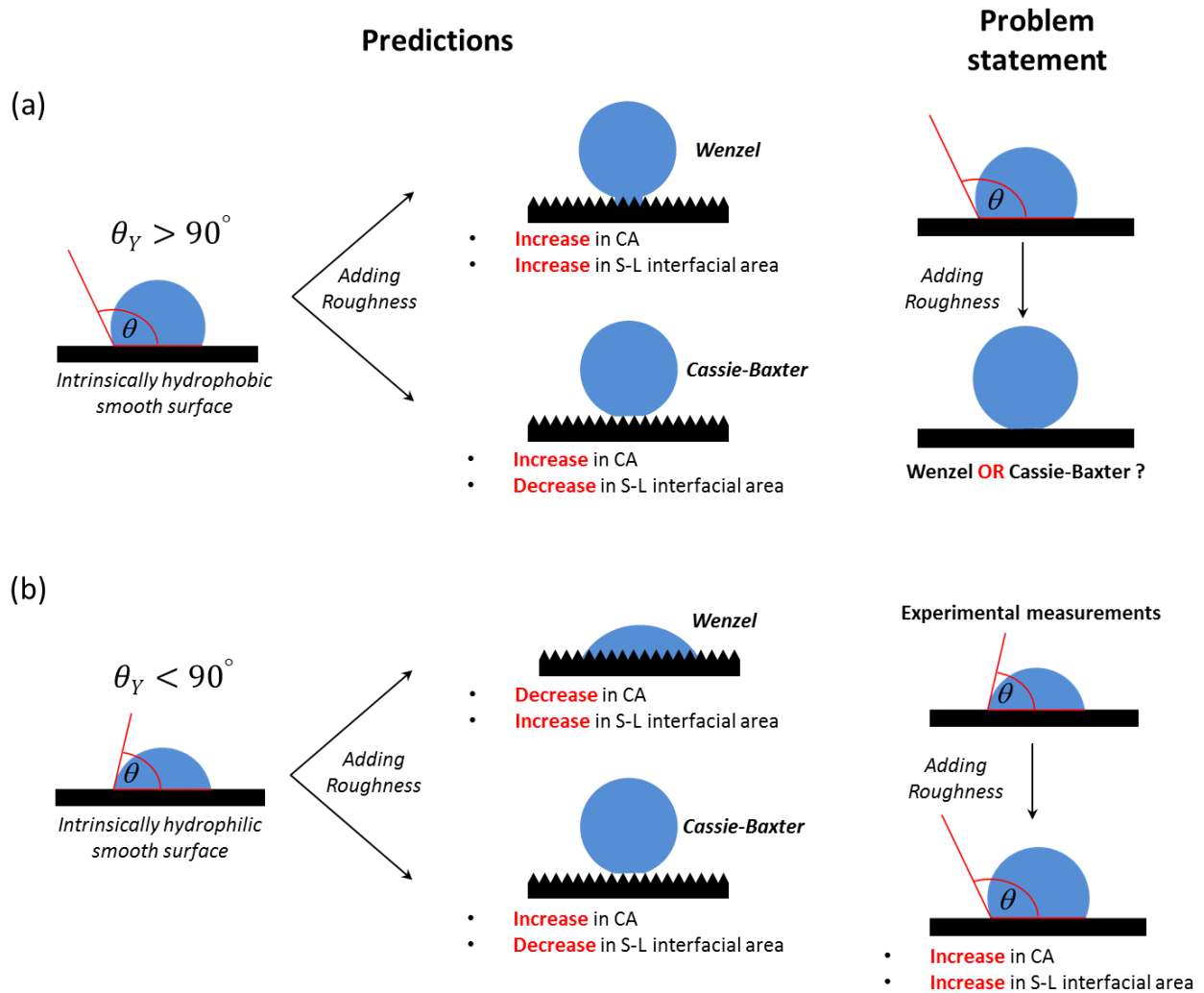


Figure 3.1: Overview of two aspects of the limitations in static contact angle measurement addressed in this study. (a) Contact angle increase on an intrinsically hydrophobic surface can correspond to both Wenzel and Cassie-Baxter wetting states. (b) Experimental results showed an anomalous increase in contact angle and S-L interfacial area after the introduction of roughness on the intrinsically hydrophilic surface, which contradicts prediction of Wenzel and Cassie-Baxter models.

3.2 Experimental methods

3.2.1 Sample preparation

Glassy carbon (GC) discs with 10 mm diameter (Sigradur G from Hochtemperatur-Werkstoffe GmbH) were used as substrates for studying the effect of roughness on surface wettability. Prior to any treatments, all bare GC discs were polished to a mirror finish with 1 μm monocrystalline diamond suspension (Allied High Tech Products Inc.) on a polishing cloth. The polished GCs were successively cleaned with acetone, isopropyl alcohol, and deionized (DI) water for 10 min each in an ultrasonic bath. The approaches used for inscribing regular and irregular roughness on the GC discs are outlined in Section 3.2.1.1 and 3.2.1.2, respectively.

3.2.1.1 Plasma treatment

Plasma treatment is used to generate randomly and homogeneously distributed nanostructured surface roughness features on the GC discs. A Sentech Etchlab 200 reactive ion etcher instrument was used for this purpose. The roughness variation was achieved by controlling the etching condition and the processing time. The samples were dried overnight and pre-evacuated in the pressure range of 10^{-6} Torr. The etching process was performed under pressure of 300 mTorr and radio frequency (RF) power of 300 W with 30 sccm O_2 gas flow to create nanostructures on the GC surface^{204,205}. In order to generate different roughness scales, different etching durations (t_{O_2}) of 2 min, 5 min and 10 min were utilized. Following the O_2 plasma etching, the samples were hydrophobized under 300 mTorr of 30 sccm CF_4 gas flow and 100 W RF power for the duration of 1 min²⁰⁶. A smooth mirror-polished sample was cleaned using a short (20 sec) O_2 plasma step followed by the same hydrophobic treatment to be used as the baseline. Similar surface treatment (O_2 plasma treatment followed by CF_4 plasma treatment) leads to similar surface chemistries and hence comparable electrochemical behaviour is expected.

3.2.1.2 Mechanical polishing

Irregular roughness features are created by mechanical polishing treatment. In contrary to micro- or nano-patterning, surface polishing with abrasive paper generates realistic surfaces that are relevant for industrial applications. One of the mirror-finish polished GC substrates was used as the smooth surface baseline to the mechanically abraded samples. Three GC discs were

roughened with abrasive papers of grit size 1200, 800, and 400. The grit size is a reference to the number of abrasive particles per inch of sandpaper²⁰⁰. The grit size of abrasive papers ranges between 15 and 65 μm , which results in different microscale roughness features as shown in the scanning electron microscopy (SEM) and atomic force microscopy (AFM) images in Section 3.3.2. After the mechanical abrasion, the GC substrates were cleaned by ultrasonication in acetone, isopropyl alcohol and DI water for 10 min each.

3.2.2 High-throughput sessile droplet setup for simultaneous optical and electrochemical measurements

Figure 3.2 shows a schematic diagram of an in-house developed sessile drop setup with coupled contact angle and electrochemical measurement capabilities that was used in this thesis work. The system works as a miniaturized three-electrode electrochemical cell consisting of a liquid droplet as the electrolyte medium, the substrate as the working electrode, and the two platinum wires (Fisher Scientific) as the counter and pseudo-reference electrode, respectively. The working, counter and reference electrodes were connected to an electrochemical analysis system (Biologic SP-150) to facilitate electrochemical measurement. The substrate was clamped on a sample holder consisting of copper contact pads mounted on an x-y platform (Siskiyou Inc.). The platinum electrodes are embedded in a polycarbonate plate and are mounted on a vertical displacement platform for controlling the distance between the platinum wires and the substrate. The experimental procedures involve placing a droplet on the substrate using a precision micropipette, followed by lowering of the two platinum wires into the droplet bulk to complete the circuit for electrochemical assessment. The thickness of the platinum wires is 25 μm , which ensures minimum distortion of the droplet shape. The setup was coupled with a camera (Canon T6i), lights and a diffuser ring to capture the droplet side view image. Apart from the optical evaluation of contact angle, the setup offers the versatility to measure the electrochemical double layer capacitance proportional to the solid-liquid (S-L) interfacial area between the droplet and substrate under study²⁰⁷. Using this proportionality, the S-L interfacial area is quantified and used as a wettability parameter along with the optically measured contact angle.

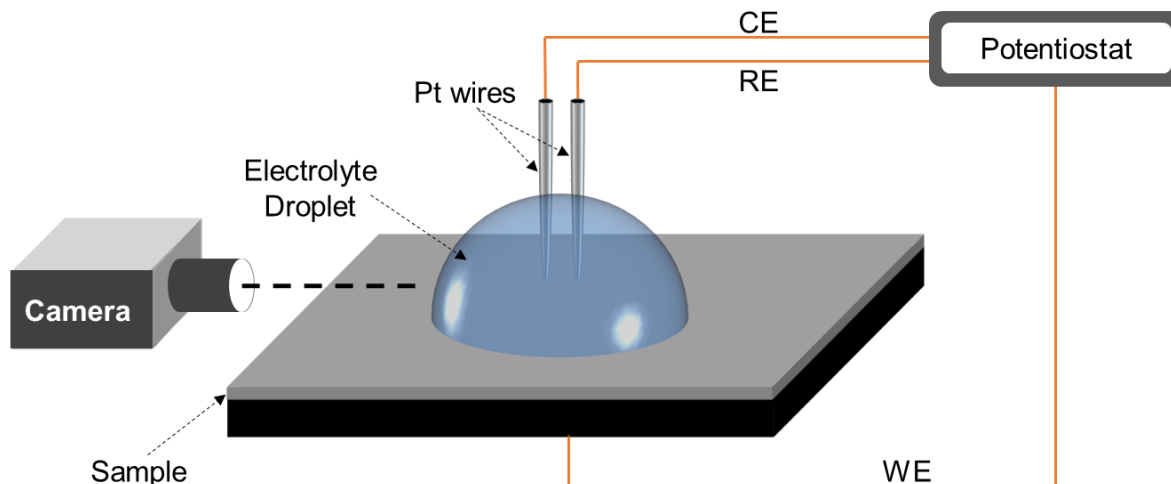


Figure 3.2: Schematic representation of the opto-electrochemical setup for simultaneous optical and electrochemical measurements. WE, CE and RE represent the working electrode, counter electrode and reference electrode, respectively.

3.2.2.1 Contact angle measurements

The static CA was determined by optical imaging of a droplet (5-10 μL) on the sample surface. The side view image of the droplet was captured using a camera (Canon T6i) and the contact angle was measured at the three-phase contact line along with the droplet base diameter using open access image analysis software ImageJ²⁰⁸. The CA and the geometrically projected surface area are used as optically measured parameters for characterizing the water-surface interaction. The surface tension of 1 M Na_2SO_4 electrolyte concentration (the highest concentration used in this study) at 20 °C is 74.67 mN m^{-1} as compared to 72.76 mN m^{-1} for pure water²⁰⁹. Therefore, the surface tension of the electrolyte solution is comparable to that of pure water. We further confirmed this by performing CA measurements at the highest concentration, which showed similar values compared to pure water droplet.

The water dynamic contact angle was measured using the needle-syringe volume changing method^{210,211}. For the roughness study on GC substrates, the initial droplet volumes for both advancing (ACA) and receding contact angle (RCA) measurements are fixed at 5 μL . A Hamilton syringe with needle outer diameter of 0.474 mm was lowered to the center of the droplet to ensure that the liquid injection or extraction would occur in a symmetrical way. The syringe was connected to a Siskiyou MC401 controller for liquid injection into or withdrawal out

of the sessile droplet at a rate of about 1 $\mu\text{L}/\text{min}$ in line with the typical low-rate dynamic CA measurement^{212–215}. The droplet volume was increased and decreased continuously by a total of 2–3 μL for the measurement of ACA and RCA, respectively. The volume variation range was chosen such that the maximum droplet volume is below 10 μL to minimize distortions in droplet shape and to ensure the minimum droplet volume is less than the amount used for the static CA (5 μL)¹⁹³. Side-view image of the droplet was taken during the progress of droplet volume variation to be analyzed for the contact angle and droplet base diameter (D) using software ImageJ. The ACA and RCA were then deduced from the plot of CA versus droplet base diameter as the maximum and minimum contact angles prior to the motion of the contact line, respectively. The contact line movement can be inferred from the change in the droplet base diameter¹¹. The ACA was identified when the droplet showed a constant CA with increasing droplet volume and diameter. A typical ACA and RCA measurement with the needle-syringe method for the smooth GC surface is shown in Appendix A. During the receding measurement, the CA profile shows a continuous decrease. However, there exists a point at about 1% decrease relative to the droplet initial diameter (D_0) where the CA shows a sudden increase. This is in agreement with the previously reported methods for measuring RCA^{216,217}. The point immediately prior to such increase was taken as the RCA. The contact angle hysteresis (CAH) values were calculated as the difference between the ACA and RCA. At least two measurements were performed at different locations of each sample and an average value is reported.

The RCA was also measured using the drop evaporation method by tracking the evaporation of sessile droplet following the procedure described by Erbil et al.²¹⁷. A 5 μL droplet was deposited onto the substrate using micropipette. The droplet was allowed to evaporate in the still air while the evolution of the droplet shape was monitored by capturing the droplet side-view images. All measurements were conducted at an ambient level with a room temperature of 20 ± 2 °C and relative humidity of 30–40 %. The side-view images were then analyzed using the software ImageJ to obtain the droplet base diameter and CA. The RCA can be retrieved from the time plots of droplet base diameter and CA based on the stick-slip motion of droplet during evaporation²¹⁷. The droplet at the initial stage is pinned, thus exhibiting a constant base diameter (D) with systematically decreasing contact angle. Following the retreat of the contact radius (decrease in droplet base diameter), the first contact angle peak corresponds to the RCA. Figure

A1 (c) shows a typical evaporation experiment in the case of the smooth GC. The experiments were repeated for at least three times to examine the reproducibility of the results.

3.2.2.2 Electrochemical measurements

The electrochemical approach to study the surface wettability involves measurement of the double layer capacitance at the S-L interface formed under the droplet. Sodium sulphate (Na_2SO_4 procured from Fisher Scientific) solutions of varying concentration (0.001-1 M) were used as the electrolyte solution to provide the necessary conductivity and to facilitate the electric double layer formation. The double layer capacitance (C) was quantified based on the total charge enclosed by the cyclic voltammetry (CV) curve using the following equation:

$$C = \frac{1}{2\nu(E_f - E_0)} \oint I(E)dE \quad (3.1)$$

Here, the integral term is evaluated based on the area enclosed by the CV curve, ν represents the scan rate, and $(E_f - E_0)$ represents the potential window for the CV measurement. In this study, a potential window of 0.2 V (-0.1 to 0.1 V vs. Pt pseudo-reference) was used at a scan rate of 100 mV s^{-1} . The average value of three measurements for each sample is reported along with the standard deviation. The electrochemical measurements were performed using a Solartron 1470E Cell Test System along with a Solartron SI 1260 Impedance/Gain-Phase analyzer.

The study on the influence of potential sweep rate and electrolyte concentration was carried out using similar droplet setup depicted in Figure 3.2. The sweep rate was varied from 10 to 500 mV s^{-1} to investigate the dependence of capacitance on the double layer charging rate. Six different electrolyte concentrations were used: 0.001, 0.01, 0.05, 0.1, 0.5 and 1 M. Following each measurement, the substrate was cleaned thoroughly with acetone, isopropyl alcohol and deionized water before a fresh droplet was deposited in order to avoid contamination from salt residue on the substrate surface.

3.2.3 Surface roughness characterization

A FEI Helios NanoLab 650 scanning electron microscope (SEM) was used to evaluate the surface morphology of the samples. Low accelerating voltage of 1 kV and beam current of 50 pA was used to ensure that the topmost surface morphology is captured. In order to compare the

roughness dimensions of the plasma-etched samples, representative feature size distribution was extracted using SEM image analysis^{218,219}. However, roughness assessment of the mechanically abraded samples using the aforementioned approach is impractical due to lack of definite features. Therefore AFM was employed to provide a 3D surface roughness profile. AFM was performed at ambient conditions using a Bruker AFM system operated in the ScanAsyst Peak Force Tapping in air mode. A Bruker ScanAsyst-Air probe tip (nominal spring constant of 0.4 N/m) was used. The scan sizes for all the samples were 40 μm by 40 μm . The AFM images were analyzed using the Nanoscope Analysis software to obtain the depth profile.

3.3 Results and discussion

3.3.1 Wettability measurement of plasma treated GC substrates

3.3.1.1 Surface characterization

SEM images in Figure 3.3 show the surface morphology of plasma-treated GC substrates. The baseline sample consists of the minimal amount of surface features and has been considered as the smooth surface in this study. In other words, the short plasma cleaning step (20 sec) and fluorination of the GC surface using CF_4 plasma does not induce any significant change to the surface morphology, but only modifies the substrate surface chemistry, which is in line with the literature²²⁰. The O_2 plasma-treated samples consist of an array of nanoscale conical structures distributed randomly and uniformly over the GC surface. The size distribution of conical features was obtained using image analysis from the SEM image as reported elsewhere^{218,219}. The width at half maximum height of at least 200 features was analyzed and used to compare the roughness dimensions between samples. The average (μ) and standard deviation (σ) of the feature size are reported in the inset of Figure 3.3. The average feature size increases with increasing O_2 plasma etching time (t_{O_2}).

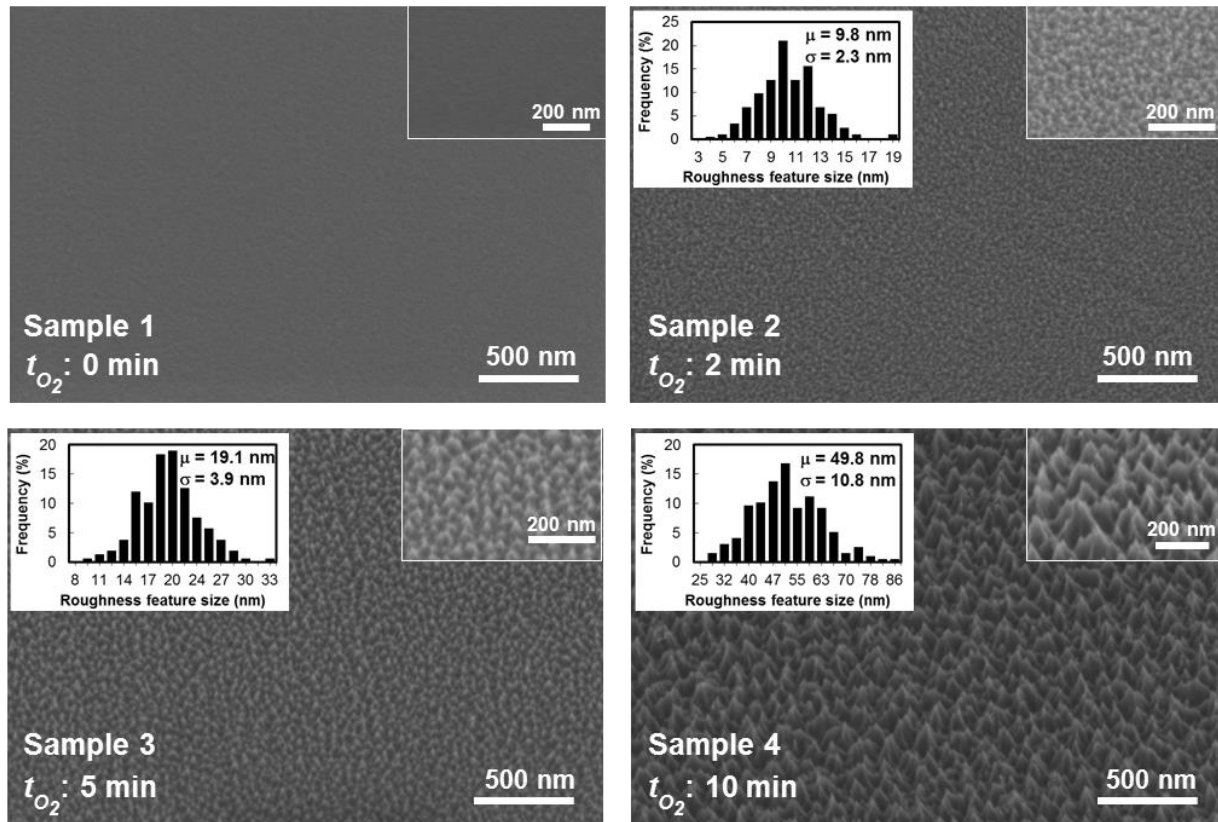


Figure 3.3: SEM micrographs of the plasma-treated GC samples. The duration of O₂ plasma etching (t_{O_2}) of each sample is indicated at the bottom left of the respective SEM image. The histograms (inset) show the distribution of the width at half maximum height of the conical feature along with the average (μ) and standard deviation (σ). All samples were cleaned with O₂ plasma for 20 seconds.

3.3.1.2 Optical wettability measurement

Figure 3.4 shows the typical droplet image of each sample along with the projected geometric area (A_{geo}) and the corresponding contact angle obtained using the image analysis. All samples demonstrated hydrophobic behaviour with a contact angle greater than 90°. The contact angle increased with the roughness scale from 100° for the smooth surface (Sample 1) to 127°, 128° and 137° for Sample 2, 3 and 4, respectively. The contact angle values of Sample 2 and 3 are comparable within the error range and thus the relative wettability of two samples could not be compared by relying only on the optical measurement. Moreover, the increase in the contact angle values with roughness for an intrinsically hydrophobic surface (contact angle of smooth sample 1 is about 100°) could correspond to either homogeneous (Wenzel) or heterogeneous

(Cassie-Baxter) wetting. In order to gain insight into the solid-liquid interfacial interaction, an electrochemical method based on the double layer capacitance is used.

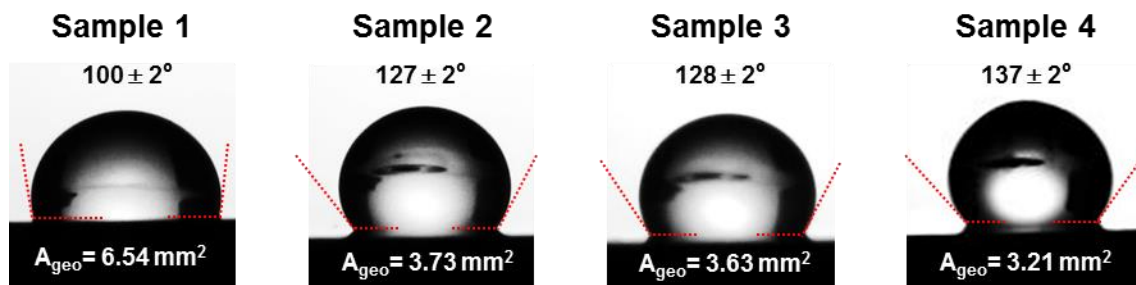


Figure 3.4: Contact angle and projected geometric area (A_{geo}) of the samples with increasing roughness from Sample 1 to Sample 4. Sample 1, 2, 3 and 4 correspond to GC substrates that have undergone O_2 plasma etching for 0, 2, 5, and 10 min, respectively.

3.3.1.3 Electrochemical wettability measurement

The double layer capacitance corresponding to the solid-liquid interfacial area under the droplet was electrochemically evaluated using cyclic voltammetry (CV), as shown in Figure 3.5 (a). The quasi-rectangular CV curves without any redox peaks indicate the capacitive property of the GC associated with charging and discharging of electric double layer²²¹. Depending on the energy dynamics, a droplet placed on a rough surface can be in a homogeneous or heterogeneous wetting state. In the homogeneous wetting mode, the liquid droplet is in full contact with the surface beneath the droplet and only the solid-liquid interface exists. For the heterogeneous wetting, the droplet is suspended on the tip of the roughness features trapping air underneath the liquid, leading to a mixture of solid-liquid and liquid-air interfaces. The presence of homogenous and heterogeneous interface under the droplet can be described using the Wenzel (Equation (1.2)) and the Cassie- Baxter (Equation (1.3)) model, respectively. These two models correlate the apparent contact angle (θ) and the intrinsic contact angle (θ_Y) based on the interfacial interaction of the solid and liquid phases.

The surface roughness parameter, r , in the Wenzel equation (Equation (1.2)) equals the ratio of the wetted area (A_{sl}) to the projected geometric area (A_{geo}), represented as A_{sl} / A_{geo} . Similarly, for the Cassie-Baxter equation, the parameter f_s can be approximated as A_{sl} / A_{geo} . In this case, Sample 1 has the smoothest surface with negligible roughness. Therefore the optically

measured contact angle of Sample 1 has been used as an approximation to the intrinsic contact angle (θ_y). Moreover, the A_{geo} of the droplet placed on Sample 1 has been regarded to be equal to the A_{sl} based on the assumption of negligible roughness feature. For Samples 2–4, the optically measured contact angle corresponds to the apparent contact angle (θ) in the Wenzel and Cassie-Baxter equations. In both equations, the parameters dependent on the S–L interfacial area (r for the Wenzel wetting and f_s for the Cassie-Baxter wetting) can be estimated based on the known θ and θ_y . The estimated values for both models are presented in the bar chart in Figure 3.5 (b).

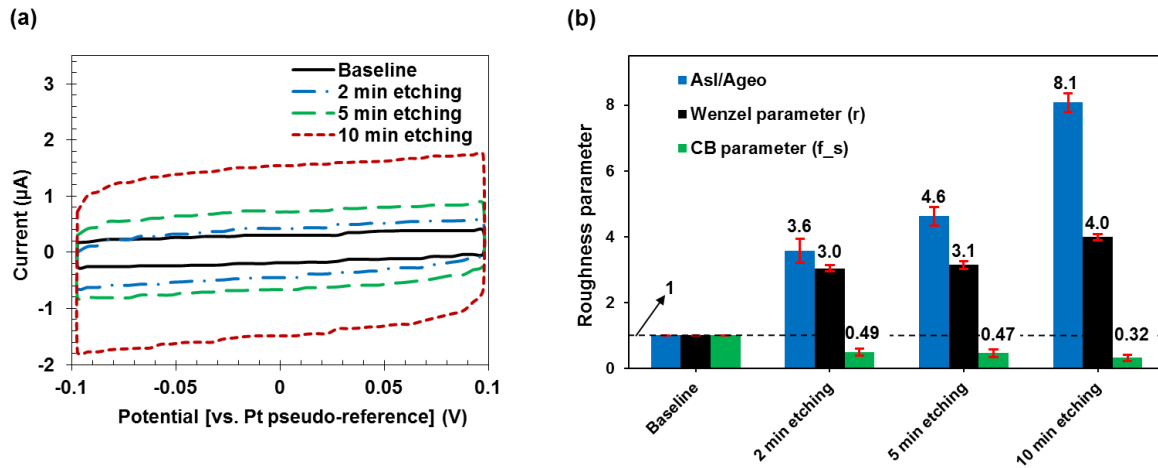


Figure 3.5: (a) Typical cyclic voltammetry curves for the plasma-treated samples obtained using a droplet of 10 μL 0.1 M Na_2SO_4 with a scan rate of 100 mV s^{-1} . (b) Comparison of the ratio of the S-L interfacial area to the projected geometric area (A_{sl} / A_{geo}) to the predicted values based on the Wenzel and Cassie-Baxter models.

The parameter r for the Wenzel equation increases with the surface roughness. In contrast, the parameter f_s from the Cassie-Baxter model decreases with an increase in the roughness. Therefore the contact angle increase upon introducing surface roughness can be described by both the Wenzel and the Cassie-Baxter models, in accordance with the case of an intrinsically hydrophobic surface depicted in Figure 3.1. In order to distinguish between these two wetting state, the electrochemical double layer capacitance is used to evaluate the ratio A_{sl} / A_{geo} .

As shown in Figure 3.5 (a), the area enclosed by the CV curve and thus the double layer capacitance increases with the surface roughness (Equation (3.1)). The electrochemical double layer capacitance (C) is proportional to the wetted area under the droplet (A_{sl}) and can be approximated as ²²²:

$$C = \frac{\varepsilon_0 \varepsilon_r}{d} A_{sl} \quad (3.2)$$

In this relation, ε_0 is the vacuum permittivity, ε_r is the relative electrolyte permittivity, and d is the double layer thickness. The characteristic double layer (diffuse layer) thickness (d), also referred to as the Debye length, can be approximated using the Debye-Hückel parameter (κ) given in the following equation ²²³:

$$d \approx \kappa^{-1} = \sqrt{\frac{\varepsilon_0 \varepsilon_r k_B T}{e^2 \sum c_i^0 z_i^2}} \quad (3.3)$$

Here k_B is the Boltzmann constant, T is the temperature, c_i^0 is the bulk electrolyte concentration, Z_i is the valency of ion i , and e is the elementary charge. The double layer thickness (d) depends on the ionic properties of the electrolyte, concentration, and temperature, all of which can be considered constant for the present system. Since the parameters ε_0 , ε_r , and d are constants, the change in the measured capacitance (C) with roughness is attributed to the change in the S-L interfacial area (A_{sl}). Applying the above concept, the ratio A_{sl} / A_{geo} has been evaluated as a roughness metric for the rough surfaces as:

$$\left. \frac{A_{sl}}{A_{geo}} \right|_{Rough} = \frac{C^R}{C^S} \times \frac{A_{geo}^S}{A_{geo}^R} \quad (3.4)$$

In the above representation, C^R and C^S are the electrochemical capacitance of the rough samples (Samples 2–4) and the smooth sample (Sample 1), respectively. The A_{geo}^S and A_{geo}^R are the projected geometric area of the droplet that is obtained from the droplet image. Sample 1 represents the smooth surface and therefore the A_{sl} is equal to A_{geo} . In other words, the A_{sl} / A_{geo} of the smooth surface baseline is equal to 1. The left-hand side of Equation (3.4) represents the ratio of S-L interfacial area to the geometric area for the rough surfaces (A_{sl} / A_{geo}) and is presented in

the bar chart in Figure 3.5 (b). From the plot, the A_{sl} / A_{geo} ratio increases with roughness and the values are greater than 1 for the rough surfaces (Samples 2–4). A higher wetted area as compared to the projected geometric area suggests the penetration of liquid into the roughness features and therefore points towards the Wenzel model. A quantitative comparison of the two parameters obtained from the Wenzel and Cassie-Baxter model (r and f_s) with the electrochemically extracted A_{sl} / A_{geo} is shown in Figure 3.5 (b). The Cassie-Baxter parameter (f_s) is smaller than 1 for all the samples. However, both r and A_{sl} / A_{geo} show values greater than 1 and increases from Sample 1 to Sample 4. From the similarity in the trend for r and A_{sl} / A_{geo} , the Wenzel model is a better representative of the wetting behaviour on the GC surface compared to the Cassie-Baxter model. Comparing the values of A_{sl} / A_{geo} with r shows that the relative difference in the predicted values increases with the roughness scale from Sample 2 to Sample 4. The percentage difference between A_{sl} / A_{geo} and r for Sample 2 is 17% while this difference increases to 43% for Sample 4 with the largest roughness.

Deviation of the wetting parameters predicted by the Wenzel and Cassie-Baxter models has been reported in previous studies^{192,224}. The optically measurable quantity does provide insights into the macroscopic features; however, validation of the models requires parameters which are otherwise inaccessible using the optical measurement. This additional parameter (A_{sl}) can bridge this information gap and facilitate resolving the model validity. Figure 3.6 summarizes the potential steps for quantitative assessment of the model predictions. Moreover, this approach is applicable for irregular roughness features and therefore can be used to study the wetting behaviour of different surface structures of stochastic nature. This work has significant implications as a tool to characterize and understand the wettability of rough surfaces as well as to facilitate the development of mechanistic and predictable mathematical models for surface wettability.

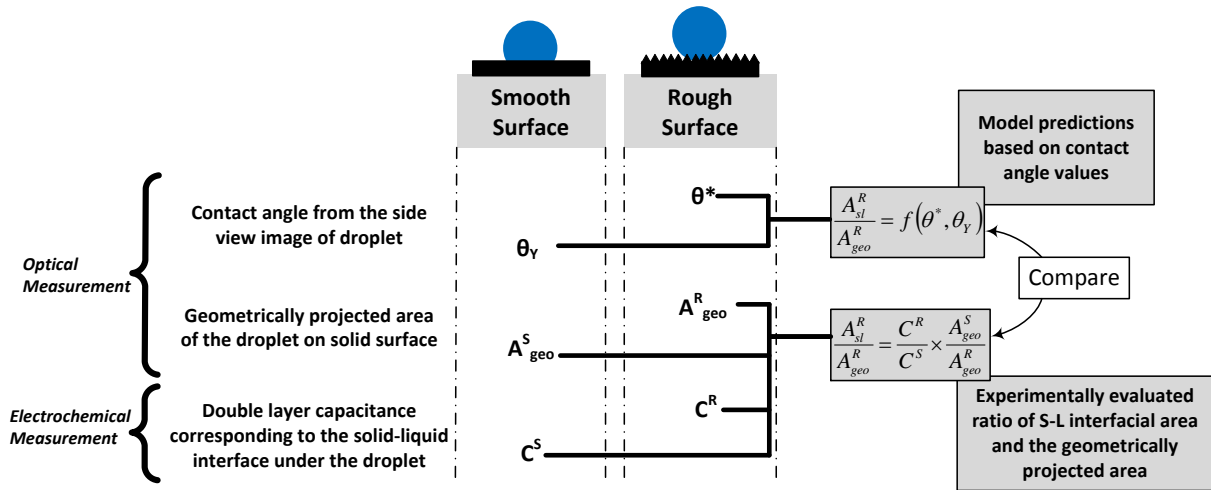


Figure 3.6: An experimental approach for validating theoretical wetting models.

3.3.2 Wettability measurement of mechanically polished GC substrates

3.3.2.1 Surface characterization

Figure 3.7 shows the SEM micrographs of the smooth (SS) baseline and mechanically polished rough (RS1 to RS3) samples at similar magnifications. For the smooth sample SS, minimal surface features were obtained as can be seen from the SEM micrograph. For the rough surfaces, irregularly distributed roughness features from the abrasion process can be observed. As reported in previous studies^{200,225}, different grit size of the abrasive papers produces varying roughness features on the surface. The AFM studies of these surfaces represent a similar trend. For the smooth sample, the dimension of roughness features is in the range of < 10 nm. However, the roughness scale shifts towards several hundreds of nanometer to microns with the mechanical polishing treatment. The distribution plots in Figure 3.7 clearly show an increase in the peak height position for the polished samples as compared to the smooth surface.

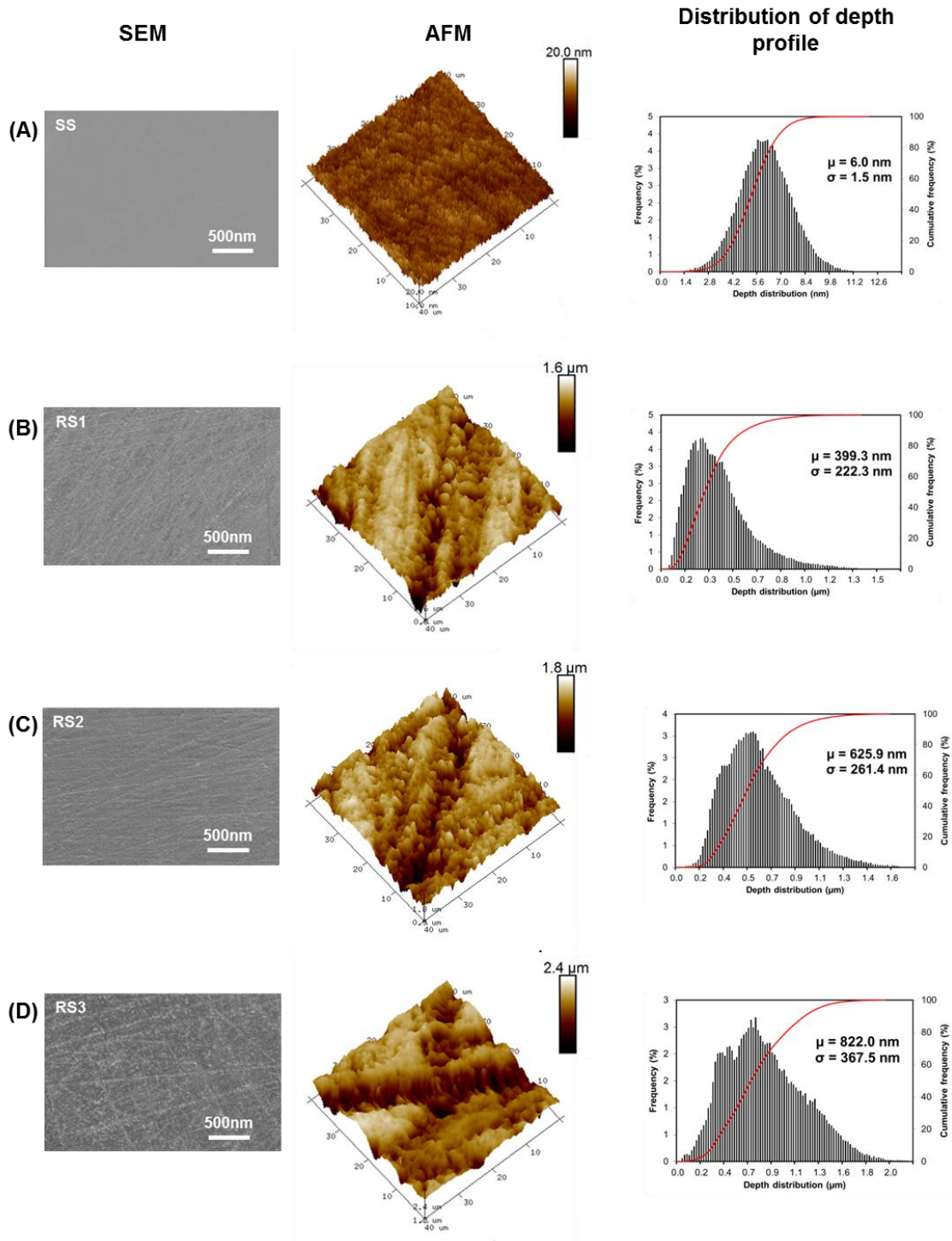


Figure 3.7: SEM micrographs and AFM analysis of the mechanically abraded GC samples. The histograms show the depth distribution of the irregular surface roughness detected by the AFM measurement. SS refers to smooth GC sample that was polished to mirror finish. RS1, RS2, and RS3 correspond to GC substrates that had been roughened using the abrasive papers of grit size 1200, 800, and 400, respectively.

3.3.2.2 Optical wettability measurement

The static contact angle was evaluated by analyzing the side view image of a 5 μ L droplet placed on the substrate. The average CA of three measurements is shown in Table 3.1 for all the samples. The CAs of rough surfaces RS1 to RS3 were found to be consistently greater (in the range of 81° and 92°) than the value obtained for the smooth sample SS representing the Young CA (62°). The CA correlates to the projected geometric area, and hence, the projected geometric area (A_{geo}) was assessed based on the projected base diameter of the droplet and is tabulated in Table 3.1. The A_{geo} for the sample SS is 6.9 mm², which is greater than those obtained for the rough samples. A larger CA and a lower A_{geo} correspond to hydrophobic behaviour, implying all the rough samples (RS1 to RS3) are more hydrophobic compared to the sample SS. The predictions of the roughness effect on the contact angle of a hydrophilic smooth surface based on the Wenzel and Cassie Baxter theories are summarized in Figure 3.1. In accordance with the Wenzel model (Equation (1.2)), an increase in the roughness factor (r) is accompanied by a decrease in the CA when the surface is intrinsically hydrophilic. On the other hand, an increase in the CA with roughness for a hydrophilic surface corresponds to the Cassie- Baxter wetting mode (Equation (1.3))⁵⁵. The rough samples in this study demonstrate an overall increase in the static CA with roughness, which hints towards the Cassie-Baxter wetting state. However, the dynamic CA and electrochemical measurements suggest Wenzel wetting.

Table 3.1: Surface wetting properties of mechanically polished samples

Sample	Static CA			Dynamic CA								
				Needle syringe						Evaporation		
	CA	±	A_{geo} (mm ²)	ACA	±	RCA	±	CAH	±	RCA	±	CAH _{evap}
SS	62.1	2.1	6.91	84.4	0.6	26.1	0.2	58.3	0.6	23.6	1.6	60.9
RS1	81.5	2.0	5.63	87.7	0.6	19.5	3.3	68.2	3.3	23.1	2.4	64.7
RS2	88.4	2.0	5.01	89.3	2.0	13.1	2.0	76.3	2.8	18.8	1.0	70.4
RS3	92.3	2.1	4.50	110.2	0.1	24.4	3.5	85.8	3.5	26.3	1.1	84.0

*All contact angle values are in degree.

The inadequacy of the static contact angle in describing the change in wetting behaviour following the alteration of surface roughness has been raised by several authors^{51,226,227}. Due to the existence of multiple Gibbs free energy minima, the static contact angle of a droplet placed on a surface is not unique. Rather, the static CA value would span a range bounded by the

advancing contact angle (ACA) and receding contact angle (RCA), depending on the location of droplet deposition and measurement method^{25,53}. We addressed this issue by measuring the ACA and RCA of all samples using the needle-syringe volume changing method, as described in the Section 3.2.2.1. Briefly, the contact line of the droplet could be pinned when the droplet volume is increased, giving rise to an increase in the apparent contact angle. The local contact line pinning is an embodiment of the presence of local energy barrier hindering the motion of advancing liquid meniscus. The CA increases to a maximum value at which subsequent volume injection would not alter the CA, but only the droplet diameter. This maximum CA value is referred to as the ACA^{228,229}. On the other hand, a continuous decrease in the CA is observed during the receding CA measurement of a hydrophilic surface^{66,210}. In the process of liquid retraction, the CA shows a sudden increase when the droplet diameter retracts from the initial pinning state^{213,217,230}. The RCA is assigned to the first immediate CA prior to the sudden CA increase.

Table 3.1 tabulates the ACA and RCA values of all samples obtained using the volume changing method. The ACA and RCA of the smooth sample (SS) are 84.4° and 26.1°, respectively. Although the sample SS has been polished to a mirror finish with minimal roughness features as shown by the SEM micrographs and AFM results (Figure 3.7), the existence of nano- or microscale roughness may lead to local contact line pinning and therefore give rise to the evolution of the ACA and RCA^{210,231}. Also, the static contact angle of the smooth sample lies in between the ACA and RCA, which agrees with other works in literature^{25,53,227}. The ACA of all the rough substrates is consistently greater than that of the smooth sample. The higher ACA relative to the smooth sample could be partly attributed to the presence of greater energy barrier induced by the introduction of surface roughness, thus offering greater resistance to droplet spreading during ACA measurement^{53,232}. The RCA of the rough samples lacks a clear trend as seen in Table 3.1. In general, the RCA is the largest for the smooth sample while the rough surfaces show lower RCA. The smaller RCA of the rough samples could be partly ascribed to the existence of a larger number of energy barriers that act as pinning points at the droplet periphery. During the receding motion, the liquid phase must disjoin from the solid surface to retract. For a droplet in Wenzel state where the liquid fills the surface asperities, the adhesive force between the solid and liquid phase is much greater compared to a droplet in the Cassie-Baxter state with minimal contact with the solid surface. Higher adhesion strength could

restraint the droplet receding motion, leading to trapping of liquid in the surface features. Therefore, the reduction in the RCA values of the rough samples relative to the smooth counterpart suggest the presence of stronger pinning force and point towards the existence of Wenzel wetting^{233,234}. The inconsistency in the RCA with sample roughness could be attributed to irregular contact line retraction as the RCA is more sensitive towards surface defects^{94,235,236}. From the ACA and RCA, the contact angle hysteresis (CAH) is calculated and shown in Table 3.1. The CAH shows a clear monotonic increasing trend with roughness. Numerous reports have also suggested that the large CAH is an indication of the Wenzel wetting state due to immobility of the droplet caused by contact line pinning^{98,112,237}.

As shown in Table 3.1, the evaporation method yields slightly different RCA values. With the exception of the smooth sample, a larger RCA was obtained based on the evaporation method as compared to the needle-syringe approach. Such a discrepancy between the two methods has been attributed to the different rate of liquid retraction during each measurement^{217,238,239}. While the evaporation provides the slowest and most steady rate, the needle-syringe method could have varied rates far from steady rate causing inaccurate RCA measurements. The CAH values based on the ACA from the needle-syringe method and RCA from the evaporation approach (CAH_{evap}) are listed in Table 3.1. Although the magnitude of the CAH has decreased by about $4.5 \pm 2.1\%$ relative to the needle-syringe case, the increasing trend with roughness still persists. The increasing trend in CAH further confirms that the rough samples in this study undergo Wenzel wetting^{112,240}. However, the observed increase in the static CA with a roughness which is typically observed for the Cassie-Baxter wetting state needs to be addressed. Hence, we utilize an electrochemical approach to estimate the wetted area underneath the droplet in an attempt to clarify the wetting mode.

3.3.2.3 Electrochemical wettability measurement

The double layer capacitance corresponding to the interfacial area under the droplet was evaluated using cyclic voltammetry (CV). Figure 3.8 shows the typical CV plots obtained for the GC samples using 0.1 M Na₂SO₄ electrolyte solution at the sweep rate of 100 mV s⁻¹. The quasi-rectangular CV curves with the absence of redox peaks indicate the capacitive nature of the GC electrodes arising from pure double layer charging process. In other words, the pseudocapacitive contribution from surface functionalities at the GC is minimal.

The capacitance, which scales with the charge enclosed by the CV curve, is higher for the rough samples than that obtained for a smooth sample (Figure 3.8). As indicated by Equation (3.2), the double layer capacitance (C) is proportional to the S-L interfacial area (A_{sl}). Here, we assumed that the A_{geo} equals to the A_{sl} for the sample SS with a smooth surface morphology at the nanoscale dimension. Based on the $C - A_{sl}$ proportionality, the interfacial area was calculated for the rough surfaces by correlating the two parameters as:

$$A_{sl}^{RS} = A_{sl}^{SS} \frac{C^{RS}}{C^{SS}} \quad (3.5)$$

Here the superscript SS and RS represent the smooth surface and the rough surfaces, respectively.

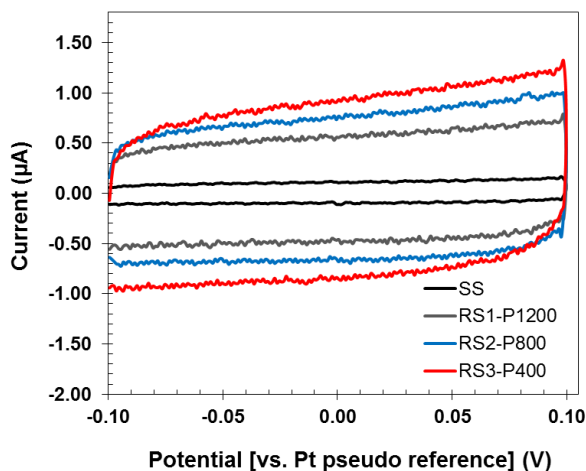


Figure 3.8: Typical cyclic voltammetry plots corresponding to a droplet volume of 5 µL, a sweep rate of 100 mV s⁻¹ and an electrolyte concentration of 0.1 M Na₂SO₄.

The magnitude of the capacitance, particularly for rough and porous surfaces, is highly dependent on the sweep rate and electrolyte concentration, which dictate the ion mobility and double layer thickness^{241–244}. Motivated by the potential implication of sweep rate and electrolyte concentration on the use of double layer capacitance for interpretation of interfacial area in this study, both parameters were varied and studied by introducing the normalized screening efficiency²⁴⁴. The screening efficiency is determined by dividing the A_{sl} / A_{geo} ratio at each sweep rate by the corresponding value at 10 mV s^{-1} , assuming complete ion access to all available surface sites at the lowest sweep rate. The cyclic voltammograms of smooth and rough samples at different sweep rates and electrolyte concentrations are presented in Appendix B.

Figure 3.9 illustrates the effect of sweep rate and electrolyte concentration on the screening efficiency for smooth and rough samples. Generally, the screening efficiency decreases with increasing sweep rate. This trend can be interpreted as a consequence of the limited mass transfer kinetics and ion penetration into the surface features at high sweep rates²⁴⁵. At high sweep rate, only the external surface of the roughness features or a small fraction of the total interfacial area is involved in the double layer charging process due to increase in ion diffusion resistance. The available time for the ions to diffuse from the bulk solution to the inner electrode surface sites is insufficient within the timeframe of each charging cycle. As a result of the shorter ion penetration depth, the inner roughness structure is practically inaccessible at higher scan rates^{246,247}. The measured capacitance originates mainly from the external surface only, leading to lower overall capacitance and reduced screening efficiency^{248,249}. In the context of surface wetting behaviour, the area within the internal structure of the roughness features is unavailable for ion adsorption at a high sweep rate, despite the liquid droplet being in full contact with the surface beneath the droplet (Wenzel wetting). Therefore, the capacitance at the lowest sweep rate resembles the closest to the full ion coverage of the electrode surface area, justifying the assumption of 100% screening efficiency at 10 mV s^{-1} . The significant difference between the screening efficiency for the rough samples at 10 and 500 mV s^{-1} offers additional proof that the droplets on rough samples are in Wenzel mode. The decreases in the screening efficiency for the rough samples are in the range of 28-34% using 1 M solution and 51-60% using 0.001 M solution. Yet the corresponding reductions for the smooth sample are significantly smaller, with 18% and 30% decrease for a droplet of 1 M and 0.001 M, respectively. The discrepancy in the

dependence of the screening efficiency on the sweep rate for smooth and rough surfaces corresponds to the variation in the ionic diffusion and double layer charging at the internal roughness features. Unlike the smooth sample that provides short ion diffusion path, the nano- and microscale roughness features in the rough samples give rise to constrained diffusion path hindering ion movement²⁴⁶. Longer time is needed for the ions to diffuse to the inner adsorption sites in the rough sample, which are inaccessible at the higher scan rate. Therefore the decrease in the screening efficiency with respect to sweep rate is greater for the rough samples. Such observation is only possible when the liquid is in contact with the solid surface inside the roughness features as for the case of Wenzel wetting state. If the droplet were in the Cassie-Baxter wetting state, the reductions in the screening efficiency for the smooth and rough samples would be expected to be similar. This is due to the absence of ionic diffusion into the internal roughness structures, which would be occupied by air pockets in Cassie-Baxter state. Therefore, for the case of Cassie-Baxter wetting, the effective area accessible for the double layer charging is restricted to the outer surface regardless of the sweep rate.

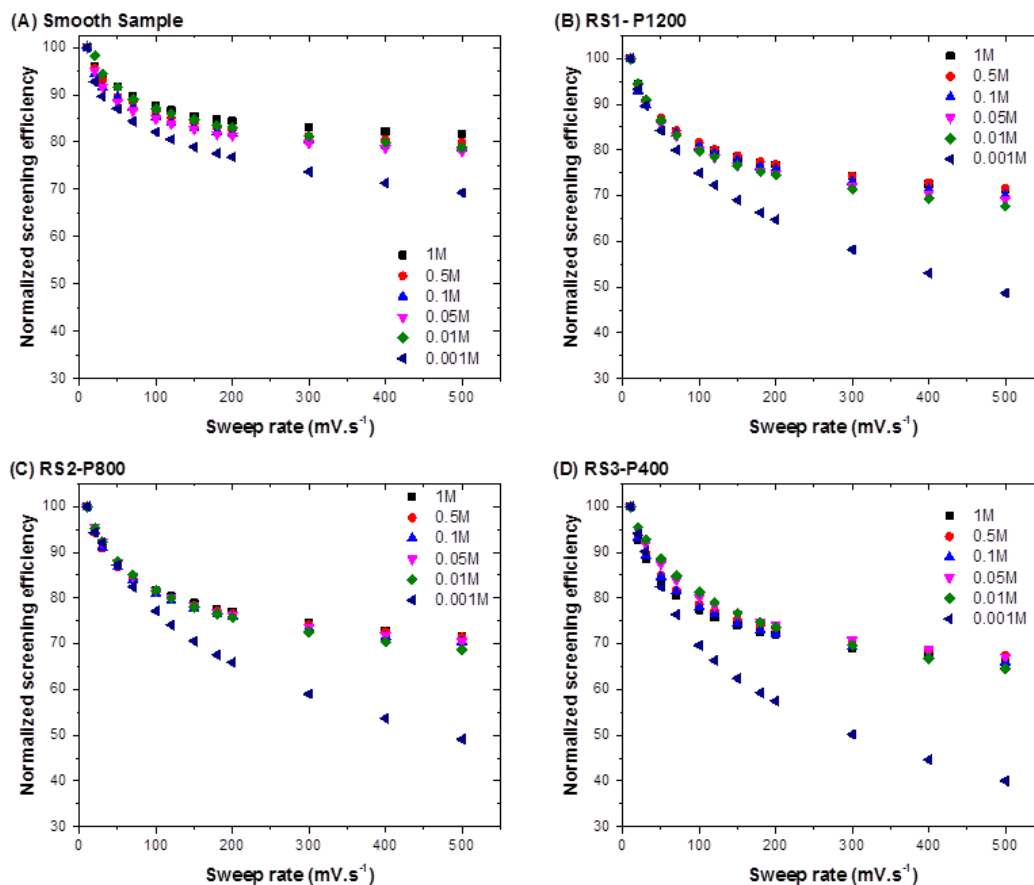


Figure 3.9: Effect of scan rate and electrolyte concentration on the screening efficiency (the A_{sl} / A_{geo} ratio normalized by the lowest sweep rate data at 10 mV s^{-1}). All plots are scaled to similar y-axis values.

For all samples, the screening efficiency using a $0.001 \text{ M Na}_2\text{SO}_4$ droplet, in comparison to a droplet of higher concentrations, has a greater dependence on the sweep rate (Figure 3.9). One possible reason for this observation is the ion-exclusion effect induced by overlapping of the double layer at low electrolyte concentrations^{245,250,251}. The Debye length representative of the double layer (diffuse layer) thickness depends solely on the electrolyte properties. Specifically, a lower electrolyte concentration would give rise to a thicker double layer^{252,253}.

On a rough surface with the presence of local curvature, it is possible for the double layers at adjacent solid surfaces to overlap, resulting in a decrease of the measured capacitance. This phenomenon is known as the shielding effect of the electric double layer and is illustrated in Figure 3.10. It has been reported that the shielding effect becomes important when the surface

roughness feature is of the same order of magnitude as the electrical double layer thickness^{250,254}. The 0.001 M Na₂SO₄ solution used in this study has a Debye length of approximately 1.8 nm at room temperature of 298 K^{223,255}. As illustrated in Figure 3.7, the depth distributions of the samples span over a wide range of few nanometers to a micrometer. Therefore, the observed underestimation of the capacitance in the case of 0.001 M Na₂SO₄ solution can be attributed to the interaction between the electrical double layers formed inside these nanoscale surfaces. The capacitance underestimation translates into lower screening efficiency because the contributions from the wetted area inside the roughness features become smaller.

Indeed the roughness-induced double layer overlapping and the resulting reduction in the measured capacitance further corroborate that the droplet is in the Wenzel wetting state. This is because the reduction in the measured capacitance from the overlapping double layer entails the establishment of electrode-electrolyte interface inside the nanoscale features. This interface is otherwise absent if the droplet is in the Cassie-Baxter wetting mode. In the Wenzel wetting state, the double layers are formed at both the outer surface as well as the inner roughness structure infiltrated by the electrolyte. Thus it is anticipated that the double layer overlapping would only come into effect for a droplet in Wenzel mode. In addition, the ionic mobility is larger at higher electrolyte concentration. The higher concentration gradient results in an enhanced mass transfer rate of ions from the bulk solution to the electrode surface during the charging process²⁴⁵. On the other hand, the electrolyte of low concentration contains an insufficient number of ions for effective charging of the double layer^{245,256}. Therefore, the measured capacitance and screening efficiency are greater at higher concentration.

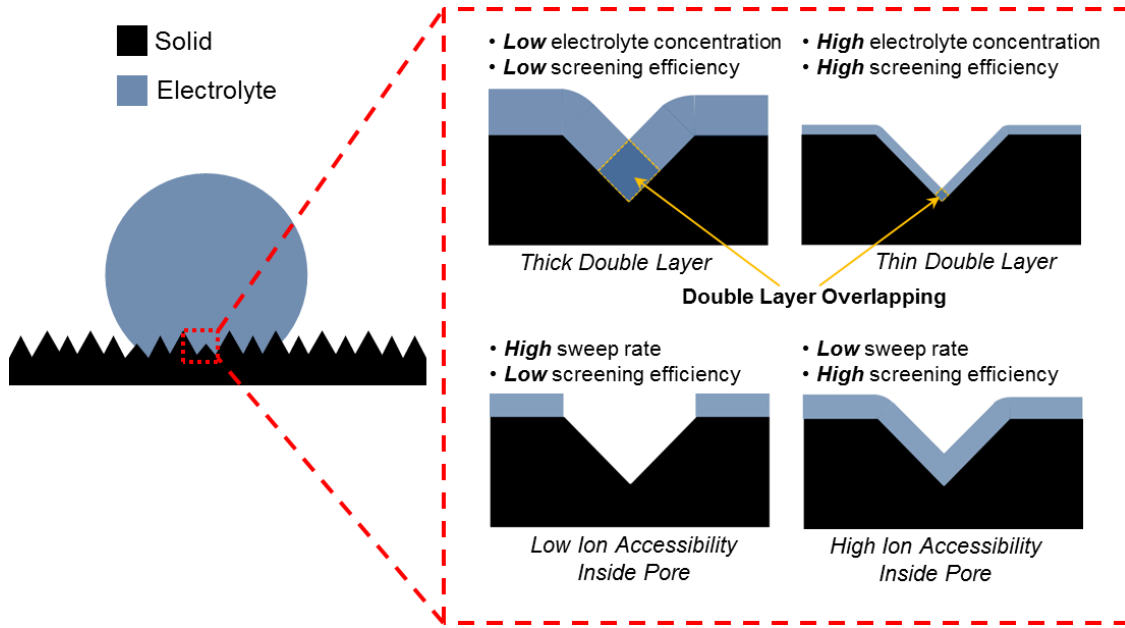


Figure 3.10: The influence of electrolyte concentration and sweep rate on the screening efficiency.

To summarize, the highest screening efficiency is achieved when a low sweep rate and high electrolyte concentration is used. When a high sweep rate and low electrolyte concentration are used, some roughness features of the solid surface could be neglected in the double layer capacitance-based interfacial area measurement, leading to low screening efficiency (Figure 3.10). Figure 3.11 demonstrates the range of A_{sl} / A_{geo} ratios obtained for each sample at varying sweep rates and electrolyte concentrations. According to the range plot, the ratio of S-L interfacial area to the geometrically projected area is larger than 1 for the rough samples under all testing conditions. This implies liquid intrusion into the roughness features for all rough samples RS1 to RS3. The A_{sl} / A_{geo} ratios of greater than unity are consistent with the aforementioned increasing trend in the CAH with roughness, suggesting the Wenzel wetting state. A quantitative real solution to the Wenzel equation is possible only when the values of $\frac{A_{sl}}{A_{geo}} \cos \theta_Y$ are less than 1. However, the values of $\frac{A_{sl}}{A_{geo}} \cos \theta_Y$ for the rough samples RS1 to RS3 are significantly higher than 1. Therefore, a real contact angle based on the relation between $\cos \theta_Y$ and A_{sl} / A_{geo} cannot be evaluated using the Wenzel equation. Even though the Wenzel

model has been presented as a general model to predict the contact angle, there exists a mathematical limitation on its applicability.

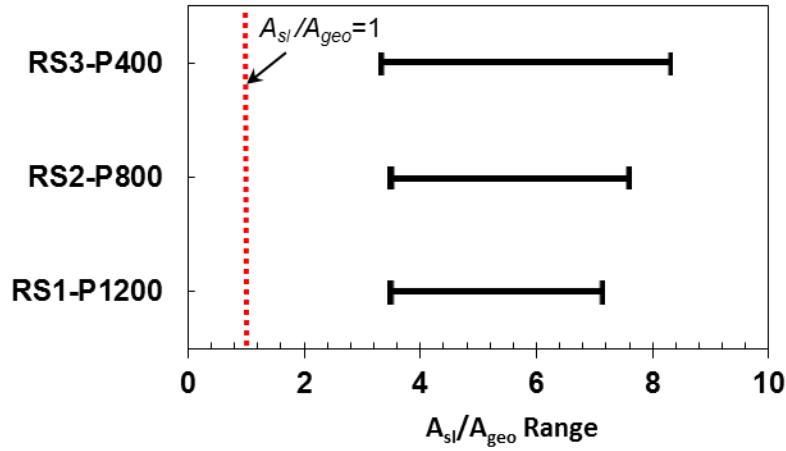


Figure 3.11: The ratio of the solid-liquid interfacial area (A_{sl}) to the geometrical area (A_{geo}) for droplet with electrolyte concentration of 0.001-1 M and sweep rate in the range of 10-500 mV s^{-1}

For intrinsically hydrophilic surfaces with apparent $CA < 90^\circ$, Wenzel state is the thermodynamically stable wetting state with a global free energy minimum²⁵⁷. The increase in A_{sl} for rough samples in this study suggests liquid intrusion into the roughness features. The liquid penetration corresponds to the description of the Wenzel model, based on which a reduction in the apparent CA should be observed. A higher CA compared to the smooth surface is an anomaly in the wetting behaviour for the rough hydrophilic surfaces, if the Wenzel model is accepted. However, an increase in the CA was observed consistently for all rough samples with irregular roughness created using different grit sizes of polishing paper. Therefore a decrease in the CA with an increase in the S-L interfacial area for a rough hydrophilic surface is not always valid. The experimental results emphasize the ineffectiveness of the Wenzel model in predicting the wetting behaviour on rough surfaces.

One possible explanation for the observed anomaly is that the three-phase contact line dictates the apparent contact angle of a droplet placed on a rough surface^{53,258}. Starting from the point when the liquid first comes in contact with the solid surface, the three-phase contact line advances until the droplet reaches a thermodynamic energy minimum²⁵. During the spreading of

the liquid droplet, the CA and the net free energy become smaller due to the formation of the S-L interface, which is dictated by the Gibbs free energy (G) of the solid- liquid-air system and is given by ⁵⁵:

$$G = \gamma_s A_s + \gamma_l A_l + \gamma_{sl} A_{sl} \quad (3.6)$$

Here, γ is the surface tension, A is the surface area and the subscripts s and l refer to the solid and liquid phases, respectively. Based on Equation (3.6), the net Gibbs free energy change depends on the solid surface area (A_s) being replaced by the liquid forming the solid-liquid interfacial area (A_{sl}) in order to minimize the Gibbs free energy of the system. The wetting models (Cassie-Baxter and Wenzel) take an average of the effect of heterogeneity to give a unique macroscopic CA, which corresponds to the global energy minimum ^{25,48,54}. Nevertheless, in addition to the global minimum, there exist multiple local Gibbs free energy minima for a rough surface, which can give rise to multiple metastable states ²²⁷. For these metastable states, the solid and liquid phases at the three-phase contact line are at equilibrium and the microscopic *actual* contact angle at the interface is equal to Young's contact angle, assuming negligible line tension ²⁵. Therefore there exists multiple metastable CA which could be measured optically for a rough surface, corresponding to the local energy minima. As the advancing liquid meniscus reaches a local minimum, the meniscus motion stops and a metastable CA larger than the value corresponding to the global energy minimum is obtained ⁵³. External energy input, such as in the form of vibration, is required to overcome the energy barrier so as to advance the droplet to the most stable wetting state. Physically, the trapping of the droplet in the metastable state results from frictional dissipation of the droplet kinetic energy during advancing of the contact line ²¹⁴. The contact line stops moving when all the kinetic energy is dissipated by friction arising from the surface heterogeneity representing the energy barrier. Overcoming the energy barrier de-pins and displaces the contact line. Nonetheless, the classical wetting models based on the global Gibbs free energy minimum do not account for the energy barrier which stops the advancing of the liquid meniscus at the three-phase contact line.

The hypothesis of the three-phase contact line governing the contact angle has been actively discussed and supported by several authors to explain the anomalous wetting behaviour in various studies for heterogeneous surfaces ^{53,73,227,259–265}. Bartell and Shepard tested the

application of Wenzel theory for water and glycerol droplets placed on smooth paraffin surface and partially cross-hatched paraffin⁵². The similarities of CA in both cases led the authors to conclude that the contact line has a dominating effect in controlling the contact angle⁵². Extrand studied lyophilic silicon surfaces containing lyophobic islands made of polystyrene⁴⁵. He showed that forcing the liquid beyond the lyophobic island by adding to the droplet volume results in the CA similar to that obtained for the homogenous periphery. His results showed that heterogeneity under the droplet does not affect the measured CA⁴⁵. Wetting behaviour on surfaces with two-component heterogeneity, consisting of a hydrophilic spot in a hydrophobic surrounding field and vice versa as well as a rough spot in a smooth surface by Gao and McCarthy, was also described using the three-phase contact line as the determining factor for CA as opposed to the contact area⁴⁶.

3.4 Summary

We have presented an experimental methodology based on simultaneous optical measurement of contact angle and electrochemical evaluation of the wetted area under a droplet for characterizing the surface wettability. The versatility of the opto-electrochemical technique was illustrated using two case studies. In the first case study, the experimental platform was used to determine the validity of theoretical models (Wenzel or Cassie-Baxter) in describing the wetting behaviour of the plasma-treated carbon substrates. Optical measurement of the droplet showed that the change in the surface wettability for the intrinsically hydrophobic samples can be predicted by both the Cassie-Baxter and the Wenzel model. In order to circumvent the limitation of the contact angle measurement, the electrochemical double layer capacitance is used as a metric to estimate the solid-liquid interfacial area under the droplet based on the proportionality between the two parameters. Using the electrochemical approach, it was deduced that the Wenzel model provides a better representation of the wetting behaviour than the Cassie-Baxter model. However, the ability of the Wenzel model in predicting the wetting behaviour was found to be dependent on the roughness. Compared to electrochemically derived A_{sl} / A_{geo} roughness ratio, the Wenzel roughness factor (r) shows an underestimation which increases with the roughness scale.

In another study, we report an anomalous wetting behaviour on intrinsically hydrophilic rough surfaces by correlating the wetted area under the droplet to the apparent contact angle. The

S-L interfacial area was determined using the similar electrochemical method described above. The wetted area is used in conjunction with the apparent contact angle as fitting parameters in the wetting models in an attempt to predict the wetting behaviour on these surfaces. Yet the observed increase in the apparent contact angle along with the S-L interfacial area with roughness contradicts the predictions by both the Wenzel and Cassie-Baxter equations. Increase in the static CA with roughness for a smooth hydrophilic surface corresponds to the Cassie-Baxter state. On the other hand, the CAH shows an increasing trend with the surface roughness, pointing towards the Wenzel wetting state. The electrochemical evaluation revealed that the ratio of S-L interfacial area to the geometrically projected area (A_{sl} / A_{geo}) is greater than 1 for the rough surfaces, regardless of the electrolyte concentration and potential sweep rate. The A_{sl} / A_{geo} ratio larger than unity suggests liquid intrusion into the roughness features, which is in line with the description of the Wenzel model. The observed anomaly is explained on the basis of the role of the S-L contact area and three-phase contact line in determining the contact angle. In fact, the dependence of the CA on the interfacial area beneath the droplet from which the wetting models are derived has been the subject of intense debate in the scientific community^{46,53,266–269}. Here we demonstrate that the electrochemical approach can play a complementary role to CA study in elucidating the wetting behaviour. The experimental results show that the solid-liquid interaction at the three-phase contact line, rather than the interfacial area, governs the apparent contact angle on a rough surface. The coupled optical and electrochemical analysis yields parameters that describe the wetting behaviour, but that is otherwise inaccessible using conventional optical method alone.

Typical studies on wetting phenomena and validity of theoretical wetting models have been performed on regularly patterned surfaces by taking advantage of the well-defined roughness features to simplify analysis. The experimental protocol involves evaluating the dimensions of the roughness features followed by calculating the S-L interfacial area for the two conditions corresponding to the Wenzel and the Cassie-Baxter models. However, extending the strategy for surfaces with irregular roughness becomes impractical to incorporate due to the stochastic nature of the roughness features. In practice, rough and irregular surfaces are more common than patterned surfaces, and they are present on a wide range of applications such as biomimetic surfaces^{270–272}, tribology²⁷³ and in-service engineering parts^{274,275}. Various attempts

have been dedicated to probing the interfacial interaction between the droplet and solid surface, including droplet visualization from top or bottom, high-resolution microscope imaging, environmental scanning microscopy, confocal scanning microscopy, reflection interference contrast microscopy, and X-rays^{199,225,276–279}. While these imaging techniques have the advantages of revealing the dynamics of the liquid meniscus during the wetting process, the applicability becomes limited for opaque materials and surfaces with irregular roughness. Another barrier hindering the progress is the unavailability of a parameter to represent the surface heterogeneity of an irregular rough surface and to link the metrics to the contact angle measurements. Following these practical limitations, the effect of irregular roughness on the contact angle and its compliance with wetting models remain largely unexplored. The electrochemical wettability characterization tool outlined in this work enables the study of surfaces with a stochastic topological distribution, circumventing the challenge of determining the dimensions of the roughness feature. Carbon surface has been used as the model system in this work, but the technique can be applied to a wide range of conductive materials which support the double layer formation. In addition, the possibility of creating rough surfaces with high contact angles while simultaneously enabling a large interfacial area, as observed in this study, could be particularly interesting for applications in droplet-based microreactors, high-throughput chemical analysis and liquid transportation^{280–283}. A large interfacial area enhances adhesiveness of droplet to minimize liquid loss whereas a high contact angle ensures small footprint and prevents excessive wetting that would otherwise obstruct the in situ analysis^{280,284}.

4 Electrochemical wettability control

4.1 Introduction

The ability to tune the surface wettability is of great interest as different wetting characteristics are desired to meet various application needs. A superwetting state with high water affinity is favourable to maximize electrode-electrolyte contact area in supercapacitor and electrolysis applications. In contrast, the water-repelling feature is the key criteria in the design of anti-icing and anti-fogging surfaces. In other instance, patterned wettability with alternate hydrophilic and hydrophobic regions proves to be useful, such as the case of water harvesting and fuel cell applications. A common strategy to alter the wetting property is to manipulate the chemical composition and surface morphology of the substrate²⁸⁵. Even though a wide range of wettability from superhydrophilic to superhydrophobic surfaces has been successfully attained, the wettability alteration achieved by tailoring the surface chemistry and structure is static in nature. To realize real-time control over the surface wettability, significant effort has been devoted to the development of stimuli-responsive surfaces with dynamically switchable and reversible wetting properties. These smart materials can span two opposing wetting states of superhydrophobicity and superhydrophilicity upon exposure to external stimuli, such as temperature, light pH and electric field. Despite recent progress in the development of switchable wettability surface, the degree of wetting switchability and reversibility, switching speed and durability still need to be improved for practical applications. In many cases, the use of tedious and complex processing steps, specialized fabrication facilities and the high cost of materials pose further challenges for the commercialization of these smart surfaces¹⁴⁵.

This chapter describes an electrochemical approach for precise and reversible in-situ modulation of the surface wettability and adhesion on a core-shell Cu-Cu_xO surface. The copper surface was prepared by means of a two-step electrodeposition technique without post-treatment using low surface energy coating material. By manipulating the oxidation state of the Cu_xO shell phase, the wetting switching from superhydrophobic to superhydrophilic regime could be accomplished within a few seconds to a few minutes by applying a low voltage (<1.5 V). Using different combinations of magnitude and duration of the applied voltage, the rate and extent of the wetting transition can be fully controlled. Moreover, the contact angle of the droplet obtained after the electrochemical manipulation was found to be stable when the applied potential was

removed. The initial superhydrophobicity is regained by air drying at room temperature for 1 hour or mild heat drying at 100°C for 30 min. Microstructural and electrochemical analysis revealed that the wetting transition is based on the Faradaic phase transformation of the surface-bound Cu_xO groups. The use of the in-situ wettability switching functionality of the Cu- Cu_xO dendritic core-shell structures was also demonstrated for gravity-driven separation of oil-water mixtures with efficiency greater than 98%.

4.2 Experimental methods

Section 4.2.1 and 4.2.2 outline the synthesis procedure and characterization techniques for both the copper plate and copper mesh. Section 4.2.3 summarizes the protocols of the contact angle measurements and electrochemical droplet manipulation on the copper plate. The experimental details for characterization of the water and oil wettability of the as-deposited copper mesh were reported in Section 4.2.4. Section 4.2.5 describes the electrochemical analysis on the mesh while Section 4.2.6 shows the methodology for using the copper mesh in separating oil-water mixtures.

4.2.1 Sample preparation

The stimuli-responsive copper oxide surface was synthesized by potentiostatic electrochemical deposition technique using a Solartron 1470E Cell Test System along with a Solartron SI 1260 Impedance/Gain-Phase analyzer. Electrodeposition of the dendritic copper was carried out on a polycrystalline copper plate in a three-electrode system with an Ag/AgCl reference electrode and a copper counter and working electrodes. The electrolyte solution consisted of a mixture of 0.1 M copper sulphate (CuSO_4) procured from BDH Chemicals, 0.1 M sodium sulphate (Na_2SO_4) procured from EMD Chemicals Inc., and 0.1 M sulfuric acid (H_2SO_4) procured from Sigma-Aldrich. The electrolyte solutions were prepared in Millipore water (18.2 $\text{M}\Omega\text{ cm}$) without any further purification. The bare copper substrate was first cleaned with acetone followed by isopropyl alcohol and Millipore water to remove any organic contaminant. Strips of copper were cut and their edges were covered with insulating Kapton polyimide tape leaving an exposed area of 2 cm^2 . The electrodeposition was carried out in two stages potentiostatically¹⁷². The first step consisted of an upper potential of -1.5 V versus Ag/AgCl reference electrode for 100 s, followed by a second step of the lower potential of -0.2 V vs Ag/AgCl for 20 s. The negative voltage induces a reduction potential that drives in the working

electrode a cathodic reaction. During the initial electrodeposition step at relatively high potential, loosely bound structures are formed due to the mass transfer limitation induced instabilities. By applying a secondary low potential step, these potentially loose structures have been found to be fixed more strongly¹⁷². After the deposition process, the copper working electrode was washed in Millipore water to remove any remaining residues, followed by air drying at room temperature for 1 h or at 100°C for at least 30 min.

For the oil-water separation experiments, copper mesh with a pore size of 140 μm was used. The copper mesh has an exposed geometric area of about 8 cm^2 with the edge covered by Kapton polyimide tape and a rubber layer. The solvent cleaning step, electrolyte mixture, electrodeposition conditions, and post-synthesis cleaning and drying procedures are similar to that adopted for the deposition of copper plate described above.

4.2.2 Material characterization

The morphology of the as-deposited and post-cycled samples was investigated using FEI Helios NanoLab 650 scanning electron microscope (SEM). A low accelerating voltage of 1 kV and 50 pA current was used to enable capturing of the top surface morphology. The size distribution of the secondary dendritic arms was obtained using SEM image analysis reported elsewhere²⁸⁶. The width at half maximum height of at least 200 features was used to generate the distribution histogram (Figure 4.2 (c)).

The crystal structure of the as-deposited and post-cycled samples was determined by X-ray diffraction (XRD) analysis. A Rigaku Rapid Axis X-ray Diffractometer with Cu $K\alpha$ ($\lambda = 1.5406 \text{ \AA}$) source was used for this purpose. In order to remove the interference effect of the Cu substrate, the electrodeposited layer was scraped off the substrate and placed on a sticky tape. High resolution (HR-TEM) and scanning transmission electron microscopy (STEM) with a probe diameter of 1 nm was used for investigating the nanoscale structure. High-angle annular dark field (HAADF) imaging was utilized to investigate the homogeneity of the structure in terms of constituent elements. The HAADF imaging technique is well-known for its sensitivity to atomic number (Z) in the structure. The STEM-HAADF technique combined with the energy dispersive X-ray spectroscopy (EDS) enabled high-resolution elemental mapping of the structure. A FEI Tecnai Osiris analytical STEM instrument operating at 200 kV was used for the

STEM analysis. EDS map quantification was performed using the Cliff–Lorimer approach implemented in the Bruker Esprit software.

The surface composition and the oxidation state at the top-most surface were evaluated using X-ray photoelectron spectroscopy (XPS). A Kratos Axis Ultra XPS instrument with a monochromatic aluminum source (Al K α , 1486.6 eV) operating at 150 W (10 mA emission current and 15 kV HT) was used for this purpose. Ar ion etching was used to obtain the profile below the top dendritic surface on the mesh. The analysis was conducted on a 700 \times 300 μm^2 area of the samples. High-resolution scans were collected at a 25 meV step size with a dwell time of 200 ms per step and pass energy of 20 eV. A Shirley background correction was applied to all XPS spectra.

4.2.3 Contact angle measurements and electrochemical wettability alteration on the copper plate

Dynamic tuning of the surface wettability mediated via redox reaction entails tracking the contact angle evolution during voltage application. In order to satisfy the concurrent needs of continuous contact angle evaluation and electrochemical measurements during the in-situ droplet manipulation, an in-house built opto-electrochemical setup was used. The experimental setup is similar to the system presented in Figure 3.2 of Section 3.2.2. The system works as a miniaturized three-electrode electrochemical cell consisting of a liquid droplet as the electrolyte medium, the as-deposited substrate as the working electrode, and two 25 μm platinum wires as the counter and pseudo-reference electrode, respectively. The experimental procedure involves placing a 10 μL droplet of 0.1 M Na₂SO₄ solution on the copper surface using a Hamilton syringe. After the droplet placement, the platinum wires are lowered into the droplet thereby completing the ionic circuit, followed by the application of a reduction potential. The changing contact angle of the droplet was captured continuously during the electrochemical droplet manipulation. Evaluation of the contact angle was performed based on the side view image of the droplet using a drop shape analysis algorithm from the image analysis software ImageJ²⁰⁸.

The ACA and RCA were measured using the volume changing method^{287–289}. A 0.1 M Na₂SO₄ droplet was gently deposited on the copper substrate using a syringe with a needle of 0.474 mm diameter. For the ACA measurement, the initial water droplet volume was 10 μL and

was increased incrementally up to 20 μL . The starting droplet volume for the RCA measurement was 20 μL , which was decreased in a stepwise manner to 10 μL . The syringe needle was lowered to the center of the droplet to ensure that the liquid injection or extraction during the dynamic contact angle measurement would occur in a symmetrical fashion. The syringe was connected to a Siskiyou MC401 controller with adjustable speed. The droplet size was manipulated via vertical motion of the syringe plunger induced by the controller, which was set at a specific speed to maintain a constant volumetric flow rate into or from the sessile droplet. Side-view image of the droplet was continuously captured during the volume increment (for ACA) or reduction (for RCA). The contact angle of the expanding and shrinking droplet was determined using the software ImageJ. The ACA and RCA were then deduced from the plot of CA versus droplet size.

4.2.4 Water and oil contact angle measurements on as-deposited copper mesh

The static contact angles (CA) of the water and oil droplets were determined by optical imaging of a 10 μL droplet placed on the copper mesh. The water and oil droplets were placed directly on the mesh surface in air to obtain the water contact angle (WCA) and oil contact angle (OCA), respectively. For the underwater oil contact angle (UWOCA) measurement, the substrate was submerged in a transparent container filled with Millipore water. The wettability of the copper mesh under high salt concentration resembling the conditions of seawater and industrial wastewater was also investigated. This was achieved by performing the CA measurements using 1 M Na_2SO_4 solution. The surface tension of 1 M Na_2SO_4 at 20°C is 74.67 mN m^{-1} , as compared to 72.76 mN m^{-1} for pure water²⁰⁹. The CA values using Millipore water and 1 M Na_2SO_4 solution are similar^{290,291}, illustrating the practical oil-water separation functionality of the mesh. For mixtures in which the oil is heavier than water, such as 1,2-dichloroethane, the oil droplet was placed directly onto the substrate. For oils with lower density compared to water, the oil droplet was placed under the substrate using an inverted needle. The side view images of the droplets were captured using a Canon T6i camera and were analyzed using the open access software ImageJ²⁰⁸. The CA measurements were performed at five different positions of the substrate to obtain the average CA value.

4.2.5 Electrochemical characterization of the as-deposited copper mesh

The electrochemical behaviours of the copper meshes were characterized using the cyclic voltammetry (CV) and electrochemical impedance spectroscopy (EIS). The CV and EIS measurements were conducted in a three-electrode setup with the copper mesh working electrode, Ag/AgCl reference electrode and platinum mesh counter electrode in 0.1 M sodium sulphate (Na_2SO_4) aqueous electrolyte solution. The CV was carried out within a potential window of 0 to -0.8 V vs Ag/AgCl at a scan rate of 30 mV s^{-1} . The impedance spectra were obtained in the frequency range of 100 kHz to 1 Hz at open circuit potential (OCP) with an AC amplitude of 10 mV and a sampling rate of 20 points per decade. The electrochemical measurements were carried out using a BioLogic SP-150 potentiostat at room temperature ($20 \pm 2 \text{ }^\circ\text{C}$). The EIS data were analyzed and fitted using the BioLogic EC-Lab software package.

4.2.6 Oil-water separation experiments

The as-prepared copper mesh was clamped between two glass funnels with diameters of 30 mm. For clarity, the oil and water were dyed with Oil red O and methylene blue, respectively. For separation of the heavy oil-water mixture, the mixture was poured into the upper funnels, and the separation process was achieved spontaneously on the as-deposited copper mesh. For separation of the light oil-water mixture, the process was triggered on-demand by applying a reduction voltage of 1.5 V on the copper mesh in a two-electrode configuration. The reduction voltage causes the reduction of surface-bound copper oxides into metallic copper, initiating the wetting transition for selective removal of water. A thin strap of carbon cloth was used as the counter electrode and the mesh as the working electrode. In both cases, the separation process was driven solely by gravity. In the oil-removing mode, the oil-water separation efficiency (η) was defined as the ratio between the mass of oil collected as filtrate after the separation (m) to the mass of oil in the original oil-water mixture before separation (m_0)^{292,293}:

$$\eta = \frac{m}{m_0} \times 100 \quad (4.1)$$

In the water-removing mode, the m and m_0 in Equation (4.1) represent the mass of water after the separation and the mass of water in the original oil-water mixture prior to the separation, respectively. Figure 4.1 demonstrates the separation process.

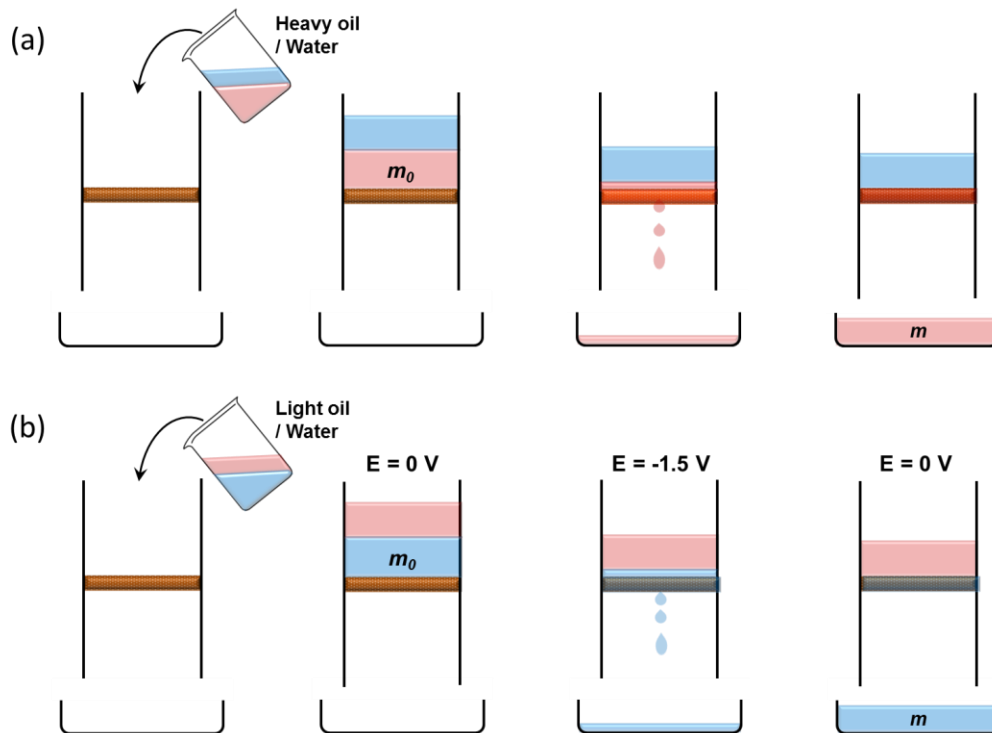


Figure 4.1: Schematic illustration of the oil-water separation process involving (a) heavy oil-water mixture in oil-removing mode and (b) light oil-water mixture in water-removing mode. The separation efficiency is determined as the ratio of the mass of oil or water phase collected (m) to the mass before (m_0) the separation.

4.3 Results and discussion

4.3.1 Surface characterization of electrodeposited copper surface

Figure 4.2 presents the surface morphology of the electrodeposited copper layer. The top-view SEM image in Figure 4.2(a) shows that the potentiostatic electrodeposition creates a layer of clustered features. At higher magnification, Figure 4.2(b) reveals that each cluster contains a dense distribution of dendritic structures. The formation of the leaf-like dendrites is in line with the previously reported results of copper electrodeposition at high potentials^{294,295}. The growth of the dendritic structures is governed by the chemical distribution of the reactive species at the growth front of particles, which is determined by the balance between the chemical diffusion and reaction rates²⁹⁶. The reaction rate determines the consumption of reactive ions whereas the diffusion rate determines the ion replenishment from the bulk solution. At sufficiently high applied potential at which the growth is diffusion limited, the ion consumption outpaces the

diffusive transport to the solid-liquid interface. The resulting concentration gradient forming at the interface leads to instability in the chemical distribution around the growth front of the particles, triggering the formation of protrusions and branch grow along the preferential directions to form dendrites^{296–299}. The histogram in Figure 4.2 (c) shows the average (μ) and standard deviation (σ) of the width (w) of individual secondary dendritic arms (as depicted in the schematic in Figure 4.2 (c)). The majority of the dendritic arms are about 290 nm in width; however, there exist some arms as wide as 700 nm.

In order to identify the crystal structure of the deposited film, X-ray diffraction (XRD) was performed. Figure 4.2 (d) shows the XRD pattern of the as-deposited layer. The XRD confirms that the structure of the as-deposited layer contains metallic copper as the main constituent. Moreover, this XRD pattern shows the absence of any crystalline copper oxide component in the structure of the as-deposited layer. However, the presence of the oxide as an amorphous or nanocrystalline phase cannot be ruled out as XRD is known for poor detection of such phases^{300,301}. The arrow in the XRD plot and the inset graph show a small peak that most likely corresponds to the CuO (111) peak. The formation of amorphous or nanocrystalline copper oxide during and after the electrodeposition has been suggested in several works^{302,303}. The peak centered at around 41.4° corresponds to a phase (indicated by the solid circle) which cannot be identified. Beside copper oxides and sulphides, trace amounts of Al, Si, and Sn have been reported in the structure of as-received copper sheet³⁰⁴. However, none of these phases and their alloy counterparts can be attributed to this peak. Based on the two major Cu peaks, a rough estimate of the crystallite size can be obtained using the Scherrer equation:

$$L = \frac{k\lambda}{\beta \cos \theta_{\max}} \quad (4.2)$$

L is the crystallite size, λ is the X-ray wavelength for Cu $\kappa\alpha$ ($\lambda = 1.5406 \text{ \AA}$), θ_{\max} is the position of the peak maximum and β is the full width at half-maximum intensity (FWHM) in radians. Based on the average values of the two observed peaks in Figure 4.2 (d), the electrodeposited copper has a grain size of $77.6 \pm 1.4 \text{ nm}$. A rough comparison of this grain size with the width of the individual dendritic branch (Figure 4.2 (c)) reveals that each branch consists of at least four to five copper crystallites. The presence of multiple grains and hence, grain boundaries in each arm makes them more prone to surface oxidation.

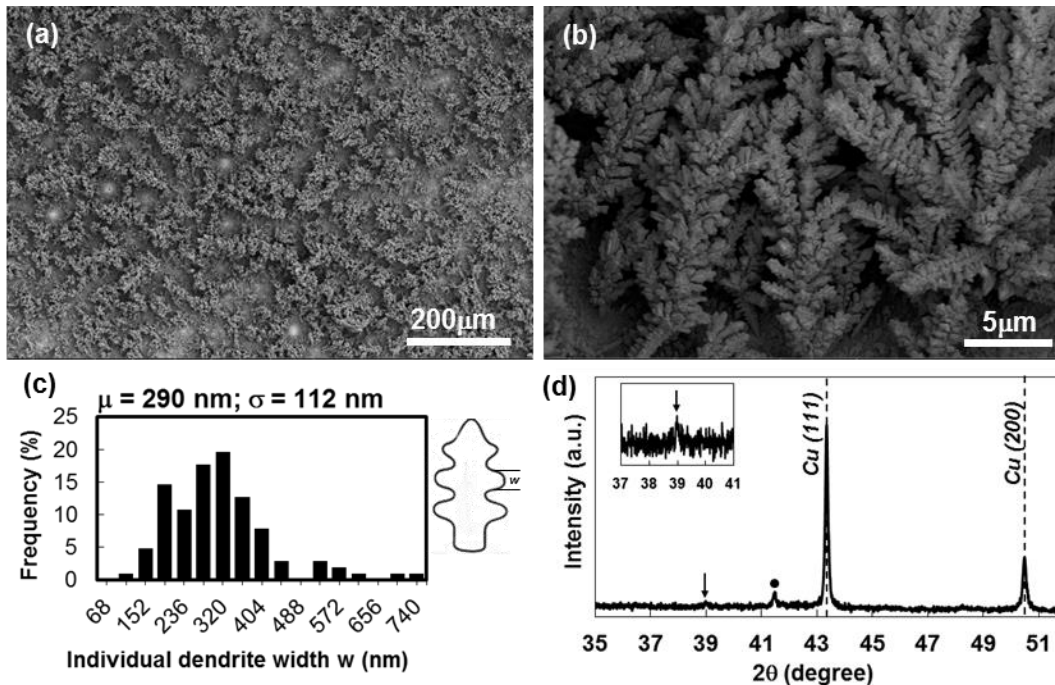


Figure 4.2: The microstructure of the as-deposited copper affects the surface wettability. The SEM micrograph shows the structure of the as-deposited copper structure at (a) low and (b) high magnification. (c) A bar chart showing the average (μ) and standard deviation (σ) of the width of individual dendritic arms (w). (d) The crystal structure of the as-deposited sample studied using XRD. The dashed lines represent the copper XRD peaks, the arrow corresponds to an amorphous/nanocrystalline CuO and the solid circle is an unidentified phase.

Although XRD does not reveal conclusive evidence of any copper oxide phase formation, there still remains the possibility of a thin nanocrystalline or amorphous oxide surface layer on the dendritic structures. This was further investigated with the aid of STEM-EDS mapping as shown in Figure 4.3. Figure 4.3 (a) shows the HAADF micrograph of a single dendrite. As suggested by the intense contrast which is directly related to the atomic number (Z) of the existing element, a uniform dispersion of single elemental grains can be observed. The presence of dark regions corresponds to the larger relative thickness of the interior crystallites. Coupling the HAADF imaging with the EDS allows for obtaining an elemental mapping, which reveals the elements present in the structure. Figure 4.3 (b)-(d) are the EDS maps of the Cu and O elements for a single dendritic structure. As can be seen in the elemental map, the interior regions of the dendrite contain high concentrations of Cu. On the other hand, the oxygen concentration tends to increase towards the exterior surface of the dendrite. Higher magnification HAADF micrographs

along with the elemental mappings from two adjacent secondary dendritic arms are shown in Figure 4.3 (e)-(h). The presence of a highly concentrated oxygen layer is evident near the surface. These results suggest that there exist a < 10 nm thick layer of an oxygen-rich layer on the surface of the as-deposited dendritic structure. The oxygen-rich layer can arise from the formation of surface oxides or the presence of adsorbed molecular O_2 or oxygen-containing species such as OH groups²⁹⁵. In fact, adsorbed O_2 upon the exposure of electrodeposited copper structures to ambient air has been attributed as the basis for their hydrophobic properties^{172,173}.

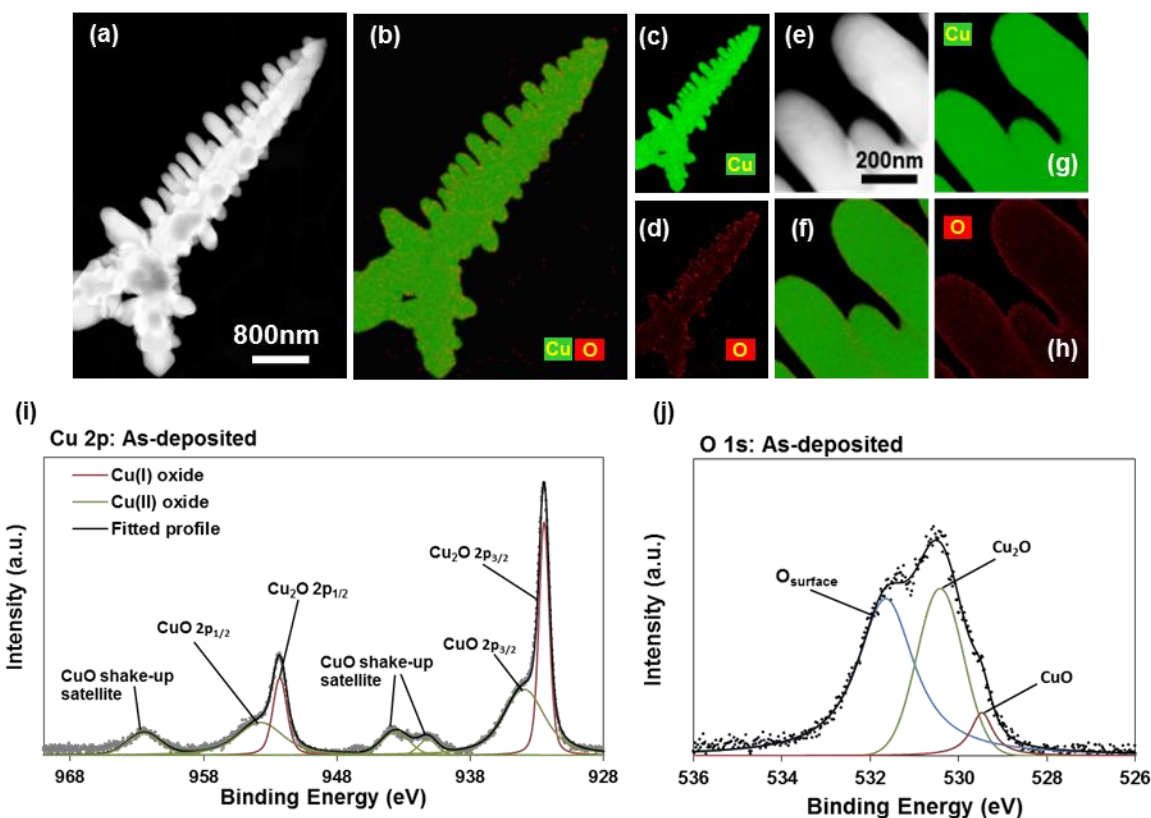


Figure 4.3: Surface composition of the dendritic structure contributes towards the hydrophobic behaviour. (a) STEM-HAADF micrographs of the as-deposited dendrite structure. (b) STEM-EDS overlapping Cu and O and individual (c) Cu and (d) O elemental mapping. (e) STEM-HAADF of dendritic secondary arms. (f) Corresponding STEM-EDS overlapping and (g) Cu and (h) O mapping. (i) High-resolution XPS spectrum of Cu 2p and (j) O 1s signal from the as-deposited sample showing the presence of oxygen in the copper lattice as well as surface oxygen groups.

XPS was applied to identify the chemical state of the copper near the top surface of the dendritic structure. The Cu 2p spectrum is the most commonly used signal for identifying the Cu oxidation state and is shown in Figure 4.3 (i). The XPS profile shows two major broad peaks indicating the Cu 2p_{1/2} and Cu 2p_{3/2} signals with a clear shoulder and satellite structures. The appearance of the satellite structures at around 943.8 and 962.5 eV binding energies arises from the open 3d⁹ shell of the CuO phase^{305–307}. The deconvolution of the Cu 2p region also indicates the existence of two overlapping signals corresponding to Cu²⁺ and Cu¹⁺ phases^{170,308,309}. The spin-orbit splitting of the two peaks assigned to the CuO phase is 19.7 eV which is in good agreement with that reported in the literature^{307,310}. The 2p signals from the metallic Cu and the Cu₂O are typically within a narrow range of binding energy^{295,308}. However, the binding energy of the Cu₂O phase generally lies at a slightly lower binding energy^{310,311}. In our case, the binding energy of the peak assigned to Cu₂O is at 932.2 eV which is lower than the typical 933 eV reported for metallic Cu. The O 1s signal was also evaluated to clarify the presence of the metal-bound oxygen on the surface. Figure 4.3 (j) shows the O1s XPS profile of the as-deposited sample. The broad O 1s peak after the deconvolution process shows three separate signals. Based on the literature, the small shoulder at the lower binding energy of 529.5 eV corresponds to the CuO phase^{312–315}. The peak centered at 530.6 eV corresponds to the oxygen in the Cu₂O lattice^{308,312}. The signal at a higher binding energy of 531.7 eV has been attributed to the chemisorbed or dissociated oxygen species at the surface^{312,313,315,316}. From these results, it can be concluded that the surface of the as-deposited dendrites contains surface oxides mixture (CuO and Cu₂O), which is in agreement with the STEM-EDS results.

4.3.2 Wettability of as-prepared copper surface

The wetting properties of the as-deposited structure were determined using the sessile droplet method at which the side-view image of a droplet was used to evaluate the CA. As Figure 4.4 (a) shows, the CA of a droplet placed on the electrodeposited copper is approximately 157.9 ± 4.5° based on over 10 measurements. Figure 4.4 (b) demonstrates an experiment in which a droplet was dropped from a centimeter height onto the as-deposited copper to examine the adhesiveness of the surface. Multiple images have been taken during the fall and bounce of the water droplet and the motion trajectory is shown by juxtaposing multiple images as a demonstration of the low adhesion induced roll-off effect. In order to further elucidate this

behaviour, advancing (ACA) and receding (RCA) contact angle measurements were performed. Figure 4.4 (c) depicts the ACA and RCA over the range of volume variation from 10 to 20 μL and the corresponding droplet diameter. The ACA is almost constant (161.8°) with a small variation of 0.9° . Similarly, the RCA also has a small variation of 1.5° during the extraction of the liquid with an average value of 157.1° . The contact angle hysteresis (CAH), calculated based on the difference between the ACA and RCA, is $4.7 \pm 1.8^\circ$. Such a low CAH ($< 10^\circ$) combined with the $\text{CA} > 150^\circ$ have been attributed as the characteristic of a superhydrophobic surface with easy roll-off behaviour^{98,237,317}. The easy roll-off behaviour is also demonstrated in Appendix C (Figure C1) showing the time-lapsed motion of the droplet when the Pt wires are removed from the droplet. The superhydrophobic behaviour and low droplet adhesion correspond to the Cassie-Baxter wetting state^{98,112}. Under such conditions, the droplet is suspended on the roughness features, thereby minimizing the solid-liquid contact area under the droplet.

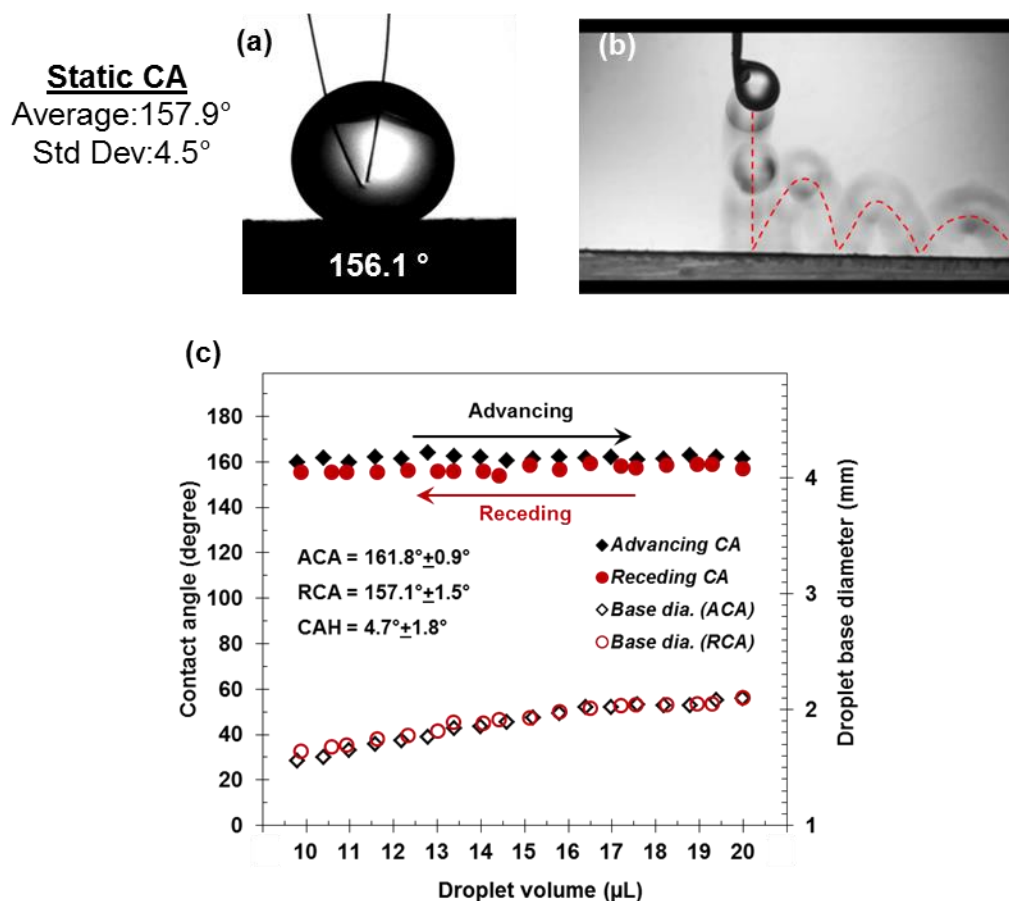


Figure 4.4: The electrodeposited copper yields a surface that exhibits superhydrophobic behaviour. This behaviour is characterized by large contact angles (a) and droplet bouncing when dropped on the surface (b) showing the low adhesion easy roll-off properties. (c) Advancing (ACA) and receding (RCA) contact angle measurements obtained by varying the droplet volume between 10 to 20 μL . The contact angle hysteresis (CAH) of the copper surface is $4.7 \pm 1.8^\circ$.

The extreme hydrophobicity with easy roll-off properties observed in Figure 4.4 arises from the synergistic effect of surface topography and chemical composition. Superhydrophobic rough surfaces without any low energy chemical additive obtained from electrodeposition of copper have also been reported in earlier studies¹⁷². High electrodeposition voltage ($> 1\text{ V}$) is typically used to induce morphological instabilities during the electrodeposition process. The resulting unstable growth imparts hydrophobicity to the surface following the introduction of surface roughness³¹⁸. In the present study, the dendritic morphologies of the electrodeposited copper offer the required roughness, as shown in the SEM micrographs (Figure 4.2). Moreover,

the secondary branching from the dendritic structure introduces multiscale roughness similar to the lotus leaf effect ³¹⁹, which further enhances the surface hydrophobicity. In addition to the roughness features, the chemical composition of the surface also plays an important role in the superhydrophobic behaviour. Pure copper in the presence of ambient air undergoes surface oxidation leading to the formation of surface-bound copper oxides comprising of CuO and Cu₂O mixture ^{170,172}. Moreover, any CuO phase on the surface tends to undergo partial de-oxidation to Cu₂O phase ¹⁵⁹. Among all the oxidation states of copper (CuO, Cu and Cu₂O), the Cu₂O phase is the most hydrophobic with apparent water CA of about 110° for a smooth surface (with roughness ≤ 10nm) ¹⁵⁹. For the present study, as confirmed by STEM-EDS mapping and XPS analysis, there exists a thin surface bound oxygen-rich layer. Correlating the water-repellent nature of the as-deposited surface with the STEM-EDS and XPS results, it is plausible to attribute such oxygen-rich layer to the presence of Cu₂O phase, which is in agreement with the previous study ¹⁵⁹. Overall, the hydrophobic Cu₂O phase, in addition to the multiscale roughness arising from the dendritic structures, imparts the superhydrophobic behaviour with low adhesion and easy roll-off to the electrodeposited surface.

4.3.3 Electrochemical wettability control: Effect of applied voltage and time duration

A redox reaction mediated electrochemical alteration of the surface chemistry can induce rapid changes in the oxidation states. In order to track the changes in surface wettability in response to alteration of the oxidation state, a reduction potential was applied to the substrate (working electrode) while simultaneously evaluating the CA. The experimental setup design is similar to the capacitive wettability evaluation setup illustrated in Figure 3.2. The as-deposited surface was used as the working electrode with two platinum wires as the counter and pseudo-reference electrodes (Figure 4.5 (a)).

Prior to the voltage application, the copper surface is extremely hydrophobic with the easy roll-off property because the droplet is in the Cassie-Baxter wetting state. As the reduction potential is applied, a gradual reduction in the CA was observed. Different reduction potential in the range of -0.7 V to -1 V vs. Pt pseudo-reference electrode was applied and the CA was measured in an interval of 60 seconds. Figure 4.5 (b) shows the reduction in the CA as a function of time at different applied potentials. As it can be observed from this plot, the rate of CA

decrease strongly depends on the reduction potential. The reduction potential determines the rate of the electrochemical reaction occurring at the solid-liquid interface and therefore affects the rate of CA decrease³²⁰. The percentage decrease in the CA under -1 V was found to be 79% and the corresponding decrease was only 6% under -0.7 V over the period of 420 seconds. These findings highlight that the CA alteration can be effectively controlled based on the applied potential.

In order to achieve an active control over the wetting behaviour, it is important that the CA remains stable after the desired CA is achieved. A stable droplet represents that the droplet should cease spreading when the potential is removed. Figure 4.5 (c) demonstrates the results of an illustrative experiment where the droplet system is alternately subject to a step input of a constant potential for a specified duration and a rest period at which no potential is applied for 2 min in a repetitive manner. The main objective of such an experiment is to demonstrate that any given CA can be achieved using the rate curves in Figure 4.5 (b) as guidelines for tuning the variation in CA. As can be seen in Figure 4.5 (c), the droplet spreads onto the surface and the CA decreases upon applying the potential. However, the spreading is halted upon removal of the potential. No significant variation in the CA was observed when no potential was applied. Upon re-applying the potential, the CA starts to reduce until the potential is removed. By applying different step potential between -0.8 and -1 V, different CA values down to 30° were achieved (the point at which the droplet lost contact with the Pt wires). The high potential can lead to a faster and a larger change in the CA. Conversely, a lower potential causes a slower change and therefore a small change in the magnitude of CA can be achieved in a controlled manner. The analogy of such procedure is to consider the high potentials for coarse tuning and the low potentials as the fine-tuning factors for the wettability alteration. These results demonstrate the capability of the electrochemical process to manipulate the CA to any desired value.

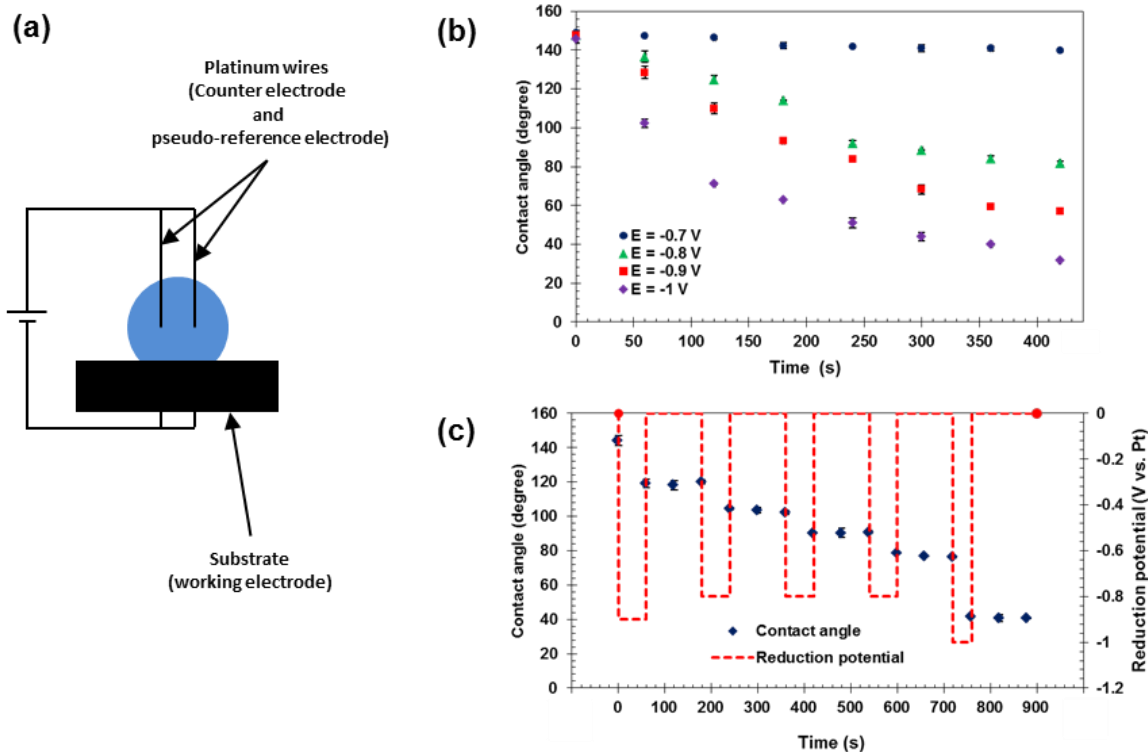


Figure 4.5: Modulation of the magnitude and duration of the applied voltage enables precise control over the rate and extent of the wetting transition. The potential represented here is referred with respect to that of the platinum pseudo-reference electrode (a) A conceptual representation of the electrochemical system where the substrate acts as the working electrode and two platinum wires as the counter and pseudo-reference electrode, respectively (b) Experimental results showing the change in the CA with time at varying reduction potentials. (c) Results showing the stability of the CA achieved after the application of the potential. The CA reduces upon the application of reduction potential but remains stable when the potential is removed.

4.3.4 Mechanism of the electrochemical wettability control

The mechanism for the wetting alteration is an outcome of two interdependent aspects, i.e. the electrochemical and physical mechanism. The surface of the dendritic structure contains copper species with different oxidation states. The wettability modulation described above is a direct consequence of an electrochemical change in oxidation state of the copper surface, which highlights the electrochemical mechanism. The change in the chemical composition drives the interaction of the liquid phase with the roughness features underneath the droplet, which corresponds to the physical mechanism. In order to elucidate on the electrochemical mechanism underlying the surface wettability manipulation, cyclic voltammetry (CV) studies were conducted on the copper oxide sample. Figure 4.6 (a) shows the CV curve of an as-deposited sample immersed in a beaker as the working electrode with Ag/AgCl and carbon plate as the reference and counter electrodes, respectively. A scan rate of 30 mV s^{-1} was used to track the redox reaction. A $0.1 \text{ M Na}_2\text{SO}_4$ solution was used as the electrolyte. The plot resembles a typical redox behaviour of copper as reported previously^{321,322}. As can be seen in this plot, the as-deposited structure undergoes two-step reduction reactions denoted as peak A and B. In general, two reduction mechanisms have been proposed³²². In a one-step reduction mechanism, CuO is directly converted into Cu. A two-step reduction mechanism involves the reduction of CuO into Cu₂O, followed by reduction of Cu₂O into Cu. Qualitative comparison of the two distinct reduction peak areas reveals the underlying mechanism in the present system. In the two-step mechanism, the Cu₂O being converted to Cu originates from the initial Cu₂O species present on the sample and the Cu₂O generated from first-step CuO reduction reaction. Thus the peak area for the reduction of Cu₂O is expected to be greater than that of the CuO reduction³²², which is reflected in the CV plot in Figure 4.6 (a). Peak A can be attributed to the reduction of CuO to the lower oxidation state Cu₂O according to Equation (4.3)³²¹⁻³²³. Further reduction to metallic Cu occurs at higher reduction potentials (peak B) as indicated by Equation (4.4)^{322,323}:



The oxidation peak at about -0.2 V (peak C) can be attributed to the oxidation of the metallic phase into the corresponding oxide states. The small shoulder peak at about -0.5 V has been correlated to the adsorption of oxygen in previous study^{324,325}.

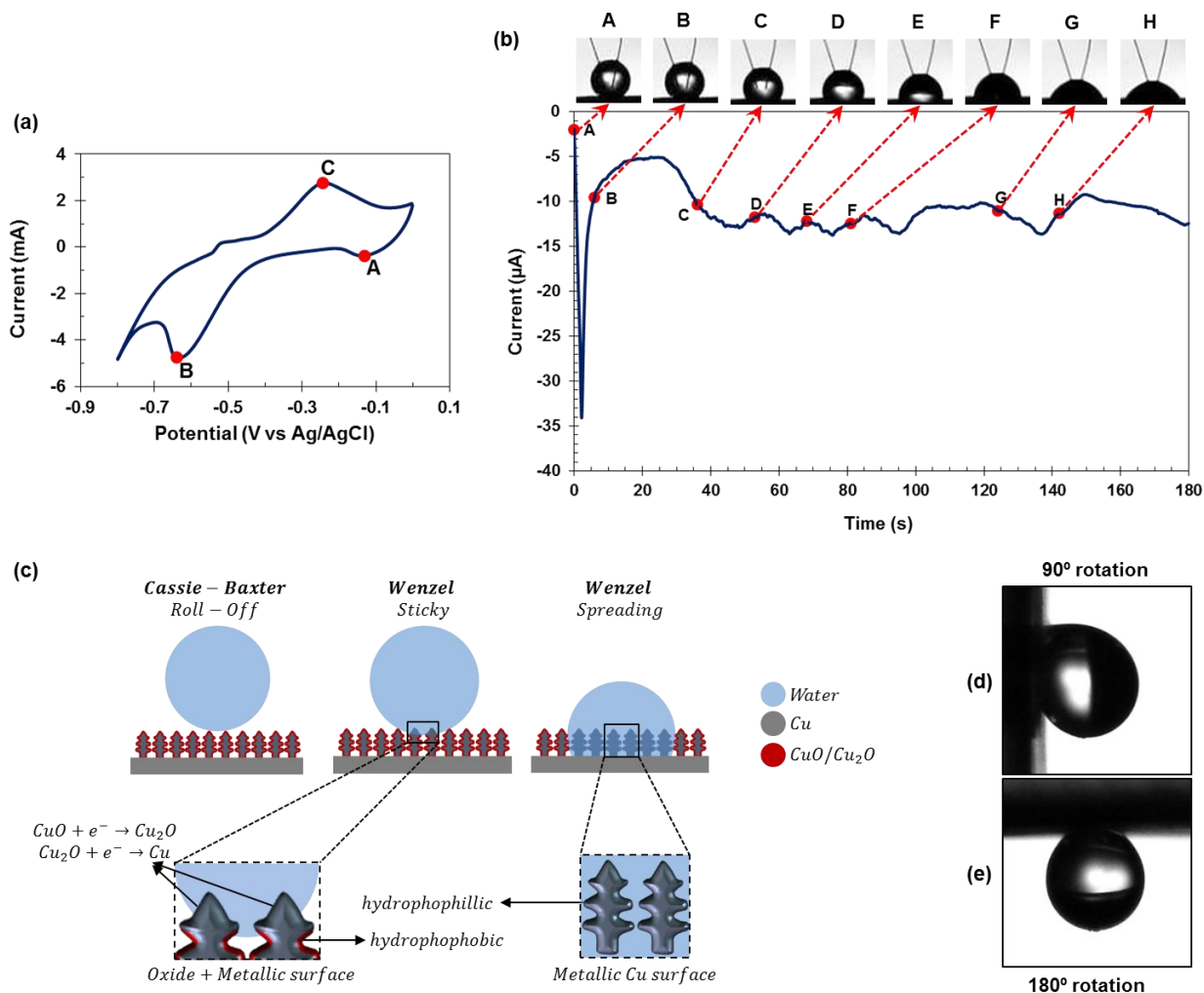


Figure 4.6: The change in the contact angle and alteration of wettability occurs due to the electrochemical change in the oxidation state of copper. (a) Cyclic voltammogram of the as-prepared 2 cm² copper strip sample in 0.1 M Na₂SO₄ electrolyte solution conducted with a potential scan rate of 30 mV s⁻¹. (b) The current vs. time profile corresponding to a droplet under a constant reduction potential of -1 V. The sequence of images from A to H shows the evolution of the droplet shape over 180 seconds of the test. (c) A conceptual representation of the underlying mechanism for the contact angle alteration. Negative potential induces the reduction of Cu₂O to Cu and the droplet penetrates into the roughness features. Further application of the reduction potential causes the three-phase contact line of the droplet to spread leading to further reduction in the contact angle. The contact angle of the droplet after the first current peak corresponding to point B in (b) at the rotation angle of (d) 90° and (e) 180° shows the transition from roll-off to sticky surface with high adhesion.

The dynamic current-time profile during the electrochemical wetting alteration revealed further insights into the two-stage dynamic transition of the droplet CA reduction. Figure 4.6 (b) shows a sequence of droplet images along with the corresponding current profile during the introduction of constant -1 V vs Pt to the droplet. During the initial phase of the applied voltage, the current increases, reaching a maximum after which the current reduces. The increase in the current corresponds to a rapid increase in the accessible solid-liquid (S-L) interfacial area occurring during the transition from the Cassie-Baxter to the Wenzel wetting state, as illustrated in Figure 4.6 (c). This stage corresponds to the transition of the surface oxide to the metallic state, which causes the penetration of water into the roughness features. After this transition, most of the unreacted hydrophobic oxide surface resides at the periphery of the droplet and the reactions occur predominantly at the three-phase contact line. Various studies have shown that the three-phase contact line plays a key role in determining the CA of a surface^{53,93}. During the first stage, the area available for the redox reaction is higher and includes area under the droplet, as compared to later stages where the reaction is confined to the periphery of the droplet. The difference in the S-L interfacial area during each stage of wetting transition results in a current peak, followed by smaller currents in later stages. Over time, the droplet CA switches from a superhydrophobic ($> 150^\circ$) to a fully wetting state ($< 40^\circ$) until the loss of electrical contact of the Pt microelectrodes with the droplet.

A droplet in a Cassie-Baxter wetting state has a lower adhesion to the surface as compared to the Wenzel wetting state³²⁶. The droplet shapes before (point A) and after (point B) the initial current peak are shown in the inset of the current profile of Figure 4.6 (b). The reduction in the CA was found to be relatively small with initial CA of approximately 157° and decrease to about 135° . However, the droplet adhesion to the surface was enhanced as can be observed in Figure 4.6 (d) and (e). The droplet remains adhered to the surface even at a tilt angle of 90° and 180° . Conversely, a droplet placed on the substrate before the electro-reduction rolled off easily (Figure C1), reflecting the low adhesion of the as-deposited sample. The increase in the adhesion and pinning of the droplet further supports the fact that during the initial stages of the CA change, the transition of the Cassie-Baxter to Wenzel wetting state occurs.

In general, CA alteration at low voltage can be achieved following two pathways, either by charge accumulation or by a change in the surface chemistry. CA alteration arising from the

charge accumulation following the Young-Lippmann equation requires the substrate to have low intrinsic electroactivity (e.g. steel and gold)^{156,157}. Conversely, in the present work, the bias potential alters the surface chemistry in accordance with the electrochemical reactions as described by Equation (4.3) and (4.4), which is the underlying cause for the change in the CA. Additionally, the wetting transition shows multiple distinct features, suggesting that the wettability switching mechanism is different from the traditional electrowetting process. In contrast with the electrowetting phenomenon where a stable CA is obtained for a bias potential, the contact angle in this study was found to decrease continuously under the reduction potential till the droplet loses contact with the counter electrode. The steady reduction in the CA and absence of stable CA suggests that the wetting alteration is dependent on the Faradaic activity resulting from the electro-reduction of surface oxide. Moreover, conventional electrowetting, which is based on the charge accumulation, is weakly dependent on the polarity of the applied potential in accordance with the Young-Lippmann equation^{152,153,327}. To investigate the impact of the potential polarity on the present system, a positive bias potential of +0.5 V vs. the Pt reference was applied. Although we did not observe a significant change in the CA and droplet profile even after 5 min of voltage application, the droplet transformed from the easy roll-off to adhesive state as shown in Figure C2 (a) and (b). In comparison to the negative potential, the CA change was negligible, which further confirms the wetting to be dependent on the potential polarity and the underlying mechanism to be different from the electrowetting phenomenon. The transition from easy roll-off to the adhesive state can be explained based on the reversible redox reactions shown in Figure 4.6 (a). The application of positive potential drives the oxidation of Cu₂O species initially present on the as-deposited substrate to CuO. Increase in the surface concentration of the more hydrophilic CuO enhances the adhesion of droplet. Any further increase in the positive potential resulted in the electrolyte decomposition accompanied by bubble formation on the Pt counter electrode¹⁵⁸.

It has been reported that exposure of copper oxides surfaces to ambient environment causes accumulation of the adventitious carbon species that promote hydrophobicity³²⁸⁻³³⁰. In order to investigate the contribution of airborne hydrocarbon adsorption during the drying process, the changes in the surface composition at the mid-point (electrochemical transition at -0.8 V vs. Ag/AgCl for 200 s) and the end of wetting transition were determined through the XPS analysis. Figure D1 (a) compares the XPS survey scans of these samples to the as-deposited

structure. As seen in the XPS results, no significant variation in the surface composition was observed. The impact of such carbon contamination at the surface was further studied by comparing the C 1s signal for the three samples in the as-deposited, mid-point and the end of wetting transition³¹⁶. Figure D1 (b) shows that all samples possess adsorbed carbon and hydrocarbon species at the surface. However, the carbon content at different stages of wetting transition seems to remain unchanged. Although the adsorbed hydrocarbon can play a role in the enhancement of the observed hydrophobic behaviour, the mechanism for the CA transition is independent of the adsorbed hydrocarbon and only depends on the copper oxidation states.

4.3.5 Reversibility of wetting alteration

4.3.5.1 Multi-cycle wetting transformation test

The as-deposited sample showed excellent underwater hydrophobicity. Figure 4.7 (a) shows the inclined angle image of the electrodeposited sample immersed in the electrolyte solution of 0.1 M Na₂SO₄. The silvery appearance of the submerged sample observed here arises due to the internal reflection of incident light at the air-water interface corresponding to the trapped air pockets within the dendritic structures of the substrate. Upon applying a potential of -0.6 V vs. Ag/AgCl reference electrode, the surface gradually becomes hydrophilic and water intrudes into the roughness features by displacing the trapped air, leading to the loss for reflectivity (Figure 4.7 (b)). The applied potential of -0.6V vs the Ag/AgCl reference electrode corresponds approximately to -0.85 V vs. the Pt pseudo-reference electrode. This electrochemically controlled underwater hydrophobicity can be important in the design and development of the smart membranes and applications requiring control over the underwater gas bubble dynamics on a solid surface.

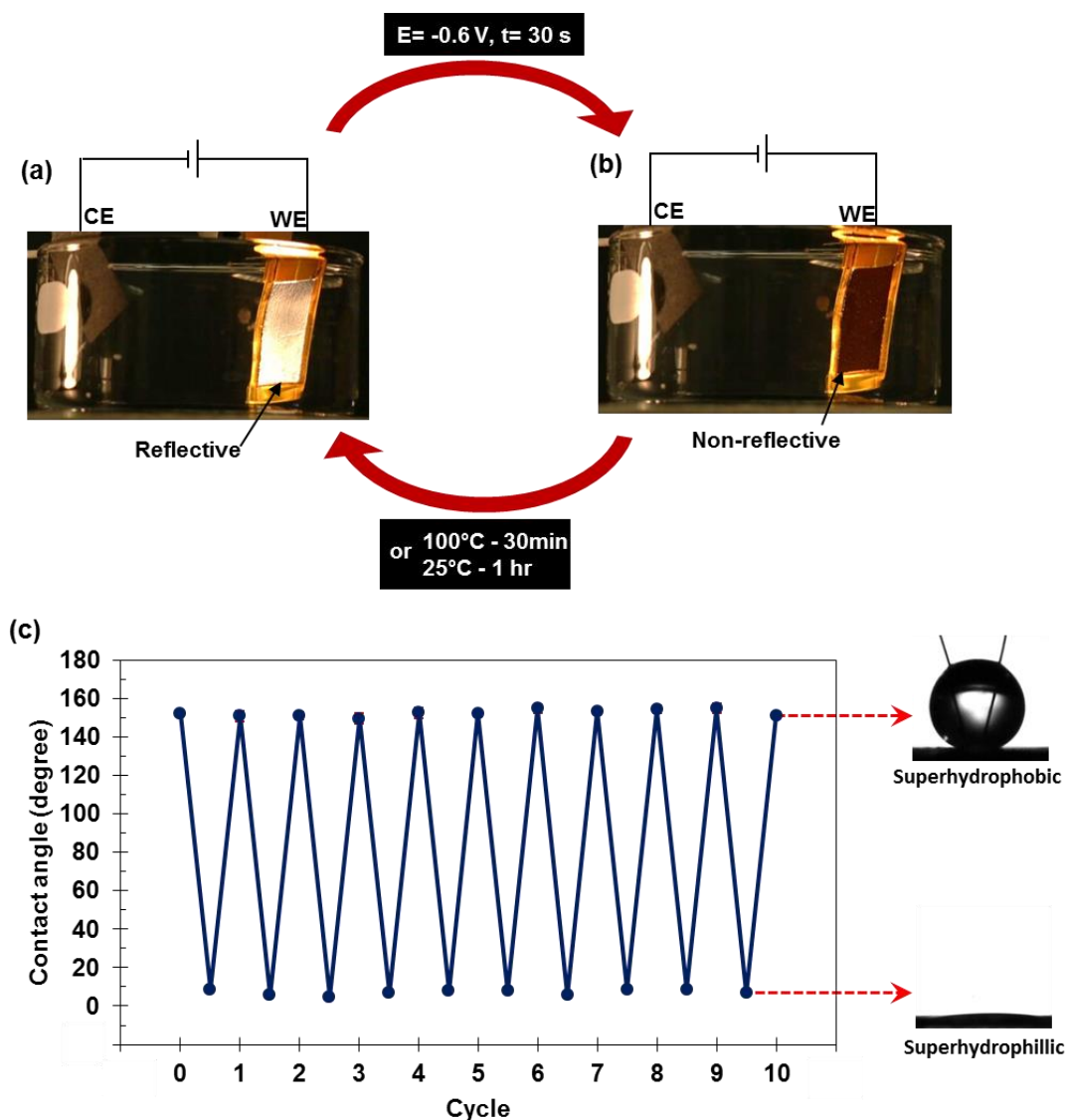


Figure 4.7: Experimental results illustrating the electrochemically controllable underwater hydrophobicity on the copper sample. The wettability alteration was found to be reversible. (a) The as-prepared sample on the copper strip immersed in 0.1 M Na_2SO_4 electrolyte shows a reflective surface due to superhydrophobicity. In the representation, WE and CE denote the working and counter electrodes. (b) The same sample as in (a) after 30 s under a reduction potential of -0.6 V vs. the Ag/AgCl reference electrode. (c) The contact angle of the copper sample measured for 10 consecutive transition cycles. Following the application of reduction potential, the sample showed superhydrophilic behaviour. After heating at 100°C for 30 min or at room temperature (25°C) for 1 hour, the initial superhydrophobic behaviour was regained.

The durability and wetting reversibility of the surface is important to allow reuse of the substrate. In order to evaluate the reversibility of the hydrophobic properties, underwater wetting transitions were performed. Following the wetting alteration, the sample was extracted from the electrolyte and washed thoroughly with DI water. The excess water was removed and the CA was measured to be around 10° demonstrating superhydrophilicity. Then, the substrate was dried using a blower followed by mild heat drying at 100°C in the air for 30 min. The CA of the surface was measured again after the drying step and the initial superhydrophobicity is fully regained. Figure 4.7 (c) shows the CA measured for the dried sample after wetting transition and after heating the sample at 100°C in the air, evaluated for 10 consecutive cycles. The CA returned to the superhydrophobic regime after the heat drying process.

4.3.5.2 Surface structure and composition after wetting transition cycles

As discussed earlier, the pure copper surface gets oxidized mostly in the form of $\text{Cu}_2\text{O}/\text{CuO}$ mixture under ambient environment as corroborated by XPS. The wetting transition occurs predominantly through simultaneous two-step reduction of the mixed oxide species into the metallic phase. Figure 4.8 (a) shows the SEM micrograph of a sample which has undergone 10 cycles of wetting transitions. A comparison of this micrograph with that obtained from the as-deposited sample (Figure 4.2) suggests that the dendritic microstructure of the sample remains intact after the wetting alteration and cycling. The STEM-HAADF and STEM-EDS mappings of the individual dendritic arm are shown in Figure 4.8 (b)-(d). The O_2 -rich region near the exterior surface of the dendrites is still observed for the post-cycled structure, as indicated in Figure 4.8 (c) and (d). The presence of this O_2 layer shows that oxygen adsorption and/or formation of copper oxide species still happens after the electrochemical reduction reaction. The crystallite size of the copper phase was also determined via Scherrer analysis of the two major copper XRD peaks, as shown in Figure 4.8 (e). The grain size does not show significant growth after the cycling when compared to the as-deposited structure (80.8 nm vs. 77.6 nm). The unidentified XRD peak at 41.4° remains intact. The introduction of the electrochemical redox reaction does not seem to have any impact on the removal of the unidentified phase corresponding to this reflection. In addition, XPS was incorporated to identify the chemical state of copper near the top surface of the dendritic structure. The XPS results obtained from the post-cycled structure is shown in Figure 4.8 (f). Similar to the as-deposited sample, the top surface is composed of mixed

oxide species of Cu_2O and CuO . These findings verify that the process of electrochemical wetting transition does not induce any microstructural alteration to the sample.

The underlying mechanism for the reversibility follows the fact that the application of reduction potential converts the oxygen-rich surface layer into pure copper. Heat drying of the sample at 100°C after the wetting transition promotes the atmospheric oxygen to react with the copper phase, thereby converting the surface into a mixture of copper oxides³³¹, as exemplified in Figure 4.8. Oxidation of the copper surface upon heating in the air as discussed in prior work³²² is the underlying reason for the substrate to regain their hydrophobicity after the heating step. It is to be noted that regenerating the hydrophobic behaviour via this heating step requires significantly shorter time (within 30 minutes) as compared to the regeneration step for the UV light based wettability alteration (as long as 2 weeks)¹⁷³.

The influence of the mild thermal drying (100°C) on the composition of the copper sample was also investigated. Two samples were prepared after the wetting transition by drying at room temperature (air-dried, 1 hr) and under 100°C (heat-dried, 30 min). The survey scan of the two samples is shown in Figure D1 (c). Comparison of the two XPS profiles reveals no change in the surface composition. The O 1s signal of these samples was also compared against that of the as-deposited structure in Figure D1 (d). As can be seen in the O 1s spectra, drying at 100°C does not introduce additional oxide species. The CA of the air-dried and heat-dried sample also shows negligible variation, as shown in the inset of Figure D1 (c). These results further confirm that the mild heat treatment only serves to accelerate the drying of surfaces as compared to the room temperature drying process.

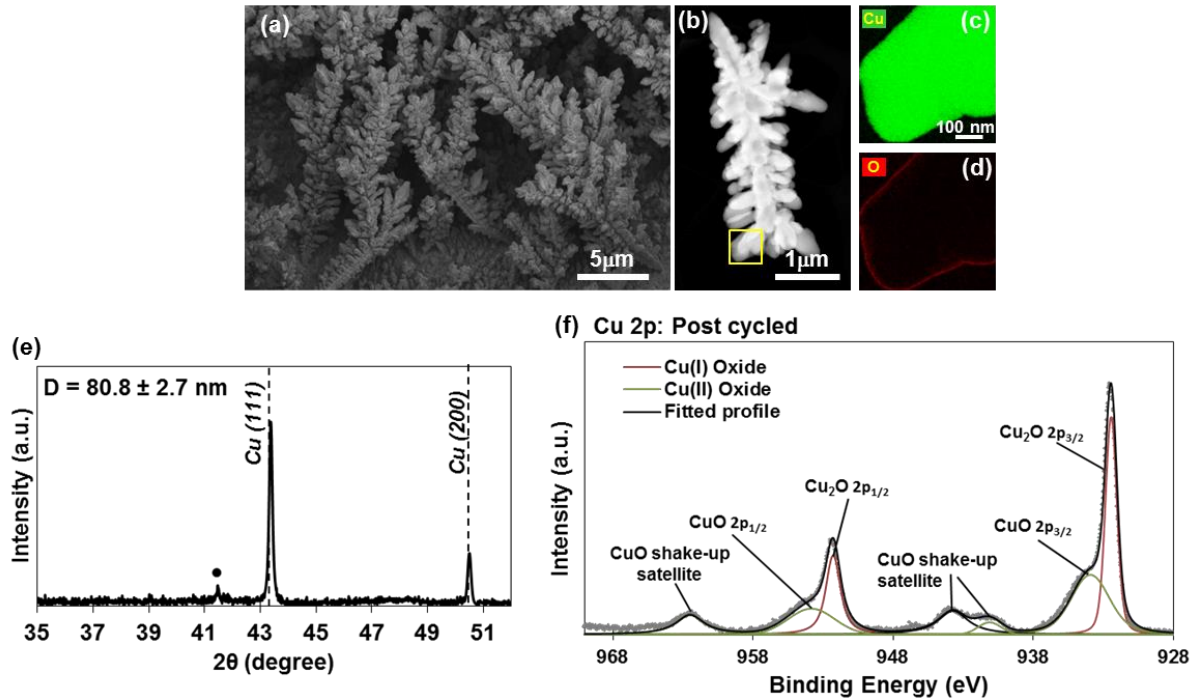


Figure 4.8: Surface properties of the copper sample which has undergone 10 consecutive wetting transition cycles resembles that of the as-deposited counterpart. (a) The SEM micrographs of the post-cycled structure. (b) STEM-HAADF micrographs of the dendrite structure after cycling. The STEM-EDS mapping of (c) Cu and (d) O for individual secondary arm indicated by the square in (b). (e) The XRD pattern of the post-cycled structure. The dashed lines represent the copper XRD peaks, the solid circle is an unidentified phase. (f) XPS spectrum of Cu 2p region for the post-cycled sample reveals similar copper oxide species as those in the as-deposited sample.

4.3.6 Application of electrochemical wettability control for on-demand oil-water separation

4.3.6.1 Surface characterization of electrodeposited copper mesh

Figure 4.9 represents the microstructure of the copper mesh before and after the electrodeposition. As can be seen in Figure 4.9 (a), the pristine Cu mesh consists of interwoven Cu wires resembling a fairly smooth surface. The presence of minor mechanical damage due to the sample handling prior to the electrodeposition is also observed. After the electrodeposition, the Cu wires are fully covered with a rough layer approximately 10-30 μm in thickness, as shown in Figure 4.9 (b) and (c). Higher magnification micrograph of the electrodeposited layer (inset in Figure 4.9 (b)) reveals that the layer contains dendritic structures similar to what has been observed previously and the copper plate^{294,295}. The dendritic structure forms due to the supersaturation of the copper metal reduced in the vicinity of the surface of the substrate which is directly proportional to the crystal growth rate²⁹⁴. Figure 4.9 (c) shows a full coverage of the electrodeposited dendritic structure on a single copper wire. The dashed line in this image represents an estimated location of the wire periphery under the electrodeposited layer.

The crystal structure of the electrodeposited layer was investigated using XRD. As Figure 4.9 (d) shows, the dendritic structure consists of metallic copper as the main constituent. The major XRD reflections of the face-centered cubic copper (FCC-Cu) are shown in this plot. The formation of metallic copper dendrites during the high overpotential of -1.5 V in an acidic electrolyte is expected and in agreement with previous studies^{294,295,332}. However, XRD is not capable of identifying the formation of any nanocrystalline oxide layer at the topmost layer^{333,334}. Hence, electron microscopy and XPS were utilized to investigate the possibility of oxide formation at the top surface layer of dendritic structures.

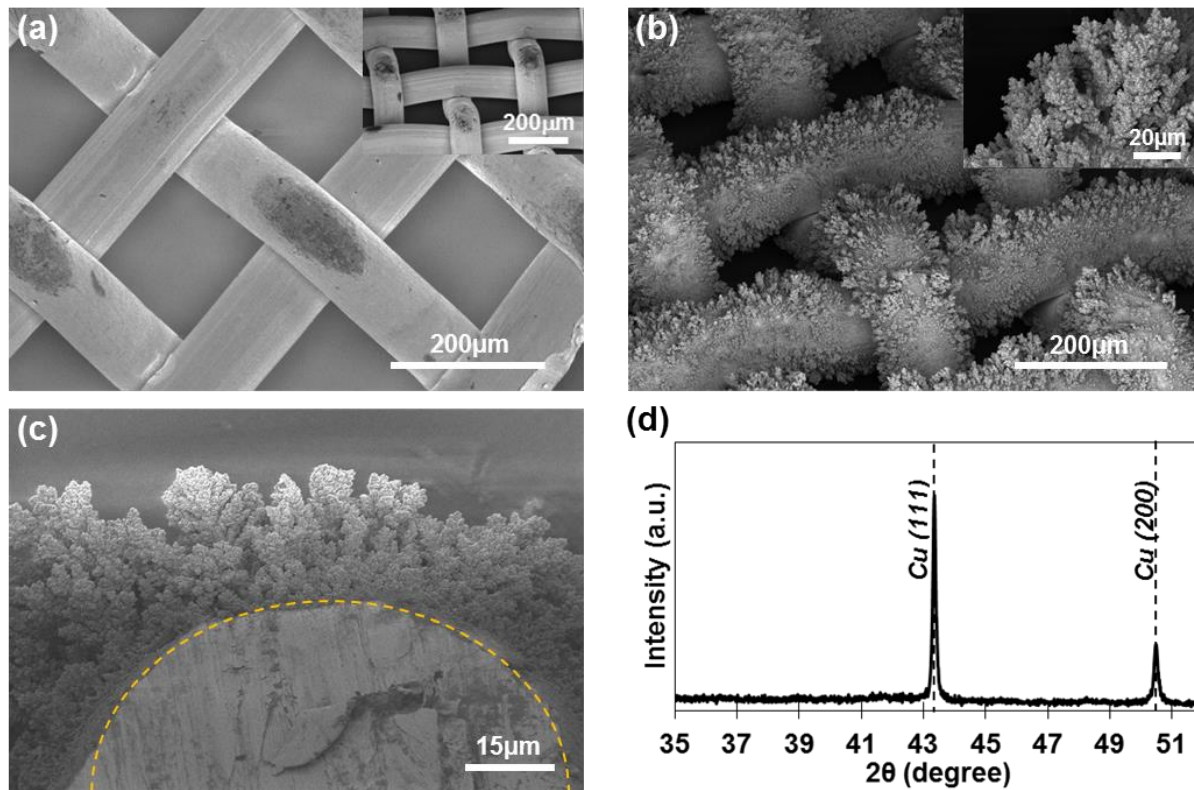


Figure 4.9: Microstructure of the (a) pristine and (b) as-deposited copper mesh. The inset shows the high magnification of the dendritic structure formed during electrodeposition. (c) The cross-section of a single Cu wire with the full coverage of dendritic structures. The thickness of the deposited layer ranges from 10 to 30 μm . (d) The XRD pattern of the dendritic structure shows a single FCC-Cu crystal structure.

Figure 4.10 (a-i) and (a-ii) shows the STEM-HAADF and STEM-EDS mapping of a single dendritic branch. Figure 4.10 (a-i) is the STEM-HAADF micrograph of dendrite cluster demonstrating multiple branching during the electrodeposition process. As suggested by the intense contrast which is directly related to the atomic number (Z) of the existing element, a uniform dispersion of single elemental grains can be observed. The presence of some dark regions corresponds to the larger relative thickness of the interior crystallites. Figure 4.10 (a-ii) shows the STEM-EDS maps of the Cu and O elements for a portion of the dendritic structures indicated by the box in Figure 4.10 (a-i). As can be seen in the elemental map, the interior regions of the dendrite contain high concentrations of Cu. On the other hand, the oxygen concentration tends to increase towards the exterior surface of dendrite forming a <10 nm oxygen-concentrated layer. Such a layer can arise from the formation of surface oxides or the

presence of adsorbed molecular O₂ or oxygen-containing species such as OH groups²⁹⁵. High-resolution TEM (HR-TEM) imaging of the near-surface regions indicated by the two arrows in Figure 4.10 (a-i) is depicted in Figure 4.10 (a-iii) and (a-iv), respectively. The corresponding Fast Fourier Transform (FFT) of each micrograph is also shown as an inset. Mixed lattice fringe spacing was observed for both regions. Based on the FFT analysis, the major spacing values of 2.32 Å and 2.46 Å was observed in Figure 4.10 (a-iii). The lattice spacing of 2.32 Å is most likely corresponding to the monoclinic CuO (111) interplanar spacing and has been previously reported^{335,336}. On the other hand, the 2.46 Å lattice fringes corresponding to the Cu₂O (111) spacing are also reported elsewhere^{337,338}. The observed lattice fringes of 2.32 Å and 2.09 Å in Figure 4.10 (a-iv) are also in line with the CuO (111) and Cu (111) planes, respectively^{335,337}. These observations corroborate the presence of mixed copper oxide shell on the copper core dendritic structure.

The XPS analysis was utilized to obtain the chemical states of the copper near the top surface of dendritic structures. Figure 4.10 (b-i) shows a typical high-resolution XPS profile near the Cu 2p region. This profile shows two major broad peaks indicating the Cu 2p_{1/2} and Cu 2p_{3/2} signals with a clear shoulder and satellite structures. The appearance of the satellite structures at around 943.9 and 962.8 eV binding energies arises from the open 3d⁹ shell of the CuO phase^{305,307,339}. The deconvolution of the Cu 2p region also indicates the existence of two overlapping signals corresponding to Cu²⁺ and Cu¹⁺ phases^{170,308,309}. The spin-orbit splitting of the two peaks assigned to the CuO phase is 19.6 eV, which is in agreement with that reported in literature^{307,310}. The 2p signals from the metallic Cu and the Cu₂O are typically within a narrow range of binding energy^{295,308}. However, the binding energy of the Cu₂O phase generally lies at a slightly lower binding energy^{310,311}. In our case, the binding energy of the peak assigned of Cu₂O is at 932.3 eV, which is lower than the typical 933 eV reported for metallic Cu. Figure 4.10 (b-ii) shows the same Cu 2p region after exposure to Ar ion etching in order to remove the top layer. As indicated in this plot, the satellite signature of the CuO phase is diminished. Moreover, the 2p_{3/2} signal is shifted toward slightly higher binding energies around 933 eV. Comparison of this binding energy with those observed for Cu₂O phase shown in Figure 4.10 (b-i) suggests that the etched surface mostly consists of the metallic copper phase. However, the presence of a trace amount of oxygen in the lattice cannot be ruled out based on the analysis of the O 1s signal described below.

The O 1s signal was also evaluated to clarify the presence of metal-bound oxygen on the surface. Figure 4.10 (b-iii) shows the O1s XPS profile of the as-deposited sample. The broad O 1s peak after the deconvolution process shows three separate signals. Based on the literature, the small shoulder at the lower binding energy of 529.5 eV corresponds to the CuO phase³¹²⁻³¹⁵. The peak centered at 530.6 eV corresponds to the oxygen in the Cu₂O lattice^{308,312}. The signal at higher binding energies (531.7 eV) has been attributed to the chemisorbed or dissociated oxygen species at the surface^{312,313,315,340}. After the etching process, the intensity of the surface-bound oxygen species decreases as shown in Figure 4.10 (b-iv). Moreover, there is a decreased amount of oxygen in the copper lattice. These results suggest that the surface of the as-deposited dendrites contains mixed oxides species of CuO and Cu₂O, which is in agreement with the STEM-EDS and HR-TEM results. The mixed copper oxide phase will be referred to as Cu_xO in the following text.

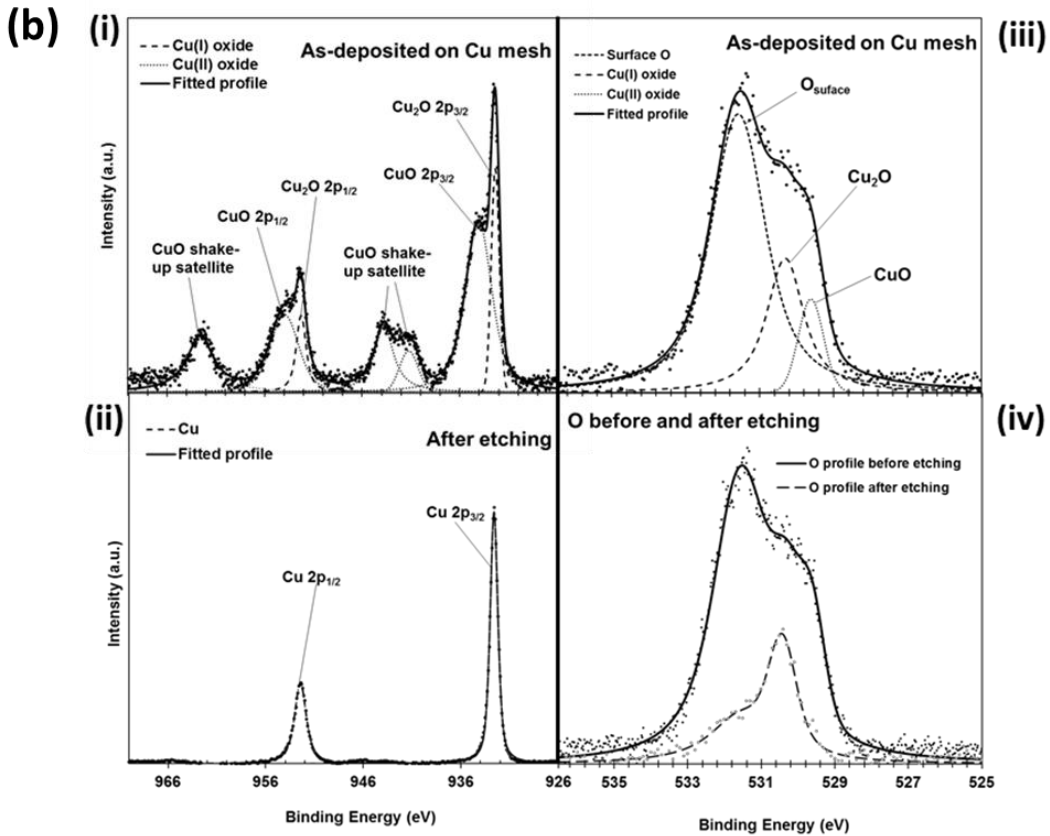
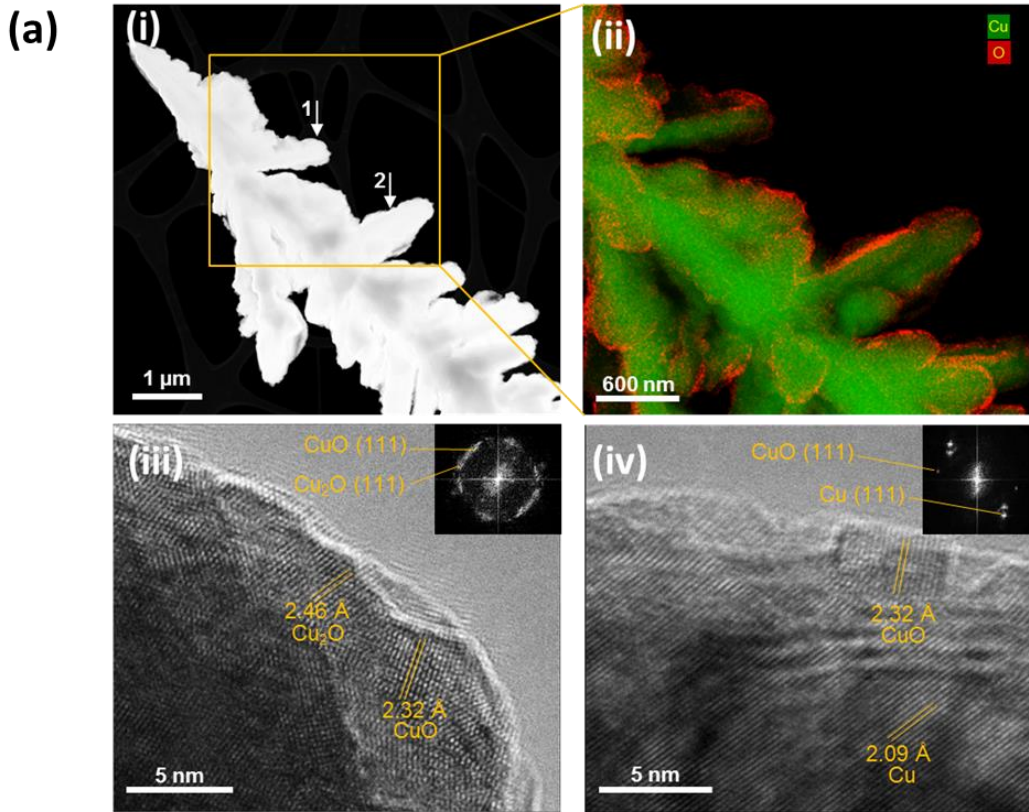


Figure 4.10: **(a)**: (a-i) STEM-HAADF of a dendritic cluster with multiple branches. (a-ii) The STEM-EDS mapping of Cu and O on single dendrite branches indicated by the box in (a-i). The concentration of oxygen tends to increase from the interior towards the exterior regions of the dendrite. (a-iii) and (a-iv) HR-TEM of the near-surface regions indicated by arrow 1 and 2 in (a-i), respectively. The insets show the corresponding FFT to identify the lattice spacing. The surface consists of a mixture of CuO and Cu₂O phases while the interior regions contain metallic copper phase. **(b)**: (b-i) XPS profile of the Cu 2p region indicates the presence of Cu(I) and Cu(II) oxide species. (b-ii) The Cu 2p region after the Ar etching indicates the removal of the oxide species. (b-iii) O 1s XPS signal from the as-deposited sample shows the presence of oxygen in the copper lattice and surface oxygen groups. (b-iv) Comparison of the O 1s signal before and after the Ar ion etching shows the removal of the surface oxygen and decreased trace of oxygen in the copper lattice.

4.3.6.2 Wettability of as-prepared copper mesh

The wetting properties of the as-deposited copper mesh towards water and oil were evaluated through the static CA, as shown in Figure 4.11 (a-i). The as-deposited copper mesh is superhydrophobic with WCA of $160.8 \pm 1.9^\circ$. The oil droplet (1,2-dichloroethane) spreads out rapidly with OCA of nearly 0° , demonstrating superoleophilicity in the air. Similar superoleophilic behaviour is observed when the mesh is placed in water with UWOCA of $7.4 \pm 1.0^\circ$. The superhydrophobicity of the as-deposited copper mesh can be attributed to the synergistic effect of the chemical composition and surface topography³⁴¹. As confirmed by the STEM-EDS mapping and XPS analysis, the dendritic structure consists of the metallic copper core and copper oxides shell phase. Among different oxidation states of copper (Cu, Cu₂O, and CuO), Cu₂O is the most hydrophobic phase with WCA of approximately 110° on a smooth surface¹⁵⁹. In ambient air, pure copper undergoes surface oxidation to form surface-bound copper oxides (Cu₂O and CuO mixture). Moreover, the CuO phase undergoes partial deoxidation to Cu₂O phase. In addition to the chemical composition, the presence of micro- and nanoscale hierarchical roughness endowed by the pores between the copper fibre mesh network and the dendritic structures further amplifies the surface hydrophobicity³¹⁹. Air trapped between the branches of the dendrites on the porous copper mesh significantly reduces the contact area between the water and the mesh surface, resulting in enhanced water repellent property³⁴². When

a water droplet is placed on such surface, the trapped air leads to a heterogeneous liquid-solid and liquid-air interfaces under the droplet. This superhydrophobic behaviour can be described using the Cassie-Baxter wetting model^{36,342,343}.

The dendritic structure restricts the permeation of water into the roughness features, which leads to a decrease in the solid-liquid (S-L) interfacial area and subsequent contact angle rise. In contrast, the oil droplet spreads on the copper mesh surface in both air and water (Figure 4.11 (a-i)). This is a consequence of the low surface tension of the oil phase and the multiscale surface morphology of the copper mesh. Driven by the low surface free energy of the mesh surface and capillary effect, the oil droplet would spontaneously wet and penetrate into the dendritic structures^{344,345}. The dendritic structures on the surfaces resemble a random network of capillary channels through which a wicking phenomenon (hemi-wicking) occurs³⁴⁶. The capillary-driven imbibition of the oil phase into the interspaces between the dendrites extends from the droplet, leading to suppression of the droplet height³⁴⁷. Liquid impregnation into the surface textures, in conjunction with the macroscopic radial propagation of the droplet meniscus, give rise to the in-air and underwater superoleophilicity.

When the superhydrophobic mesh is underwater, the air pockets remain trapped in the roughness features (Cassie-Baxter conditions). When the oil droplet is brought in contact with the solid surface, the air trapped in the microstructure gets displaced by the oil. Therefore, the wetting behaviour is expected to show a close resemblance to the behaviour observed for the oil droplet in the air. Even though the interaction shows superoleophilic behaviour, the spreading of the oil on the copper microstructure is slightly restricted as compared to the oil in the air system. This can be observed in Figure 4.11 (a-i), where a visible oil meniscus is observed for the underwater condition, while no such meniscus is observed when the oil is brought in contact with the substrate in air. This restricted spreading is the result of a liquid-solid interface where the tip of the dendritic structures are in contact with the water, which is evident from the finite conductivity when a bias potential is applied, as will be discussed in Section 4.3.6.3. In conventional wicking, a thin film of the liquid precedes the spreading of the macroscopic meniscus²³⁴. However, when the oil is brought in contact with the surface underwater, the advancing movement of the droplet meniscus following the precursor film is restricted by the

wetted tips of the dendritic structure. The restricted motion of the meniscus results in the observable meniscus and the incomplete spreading on the surface.

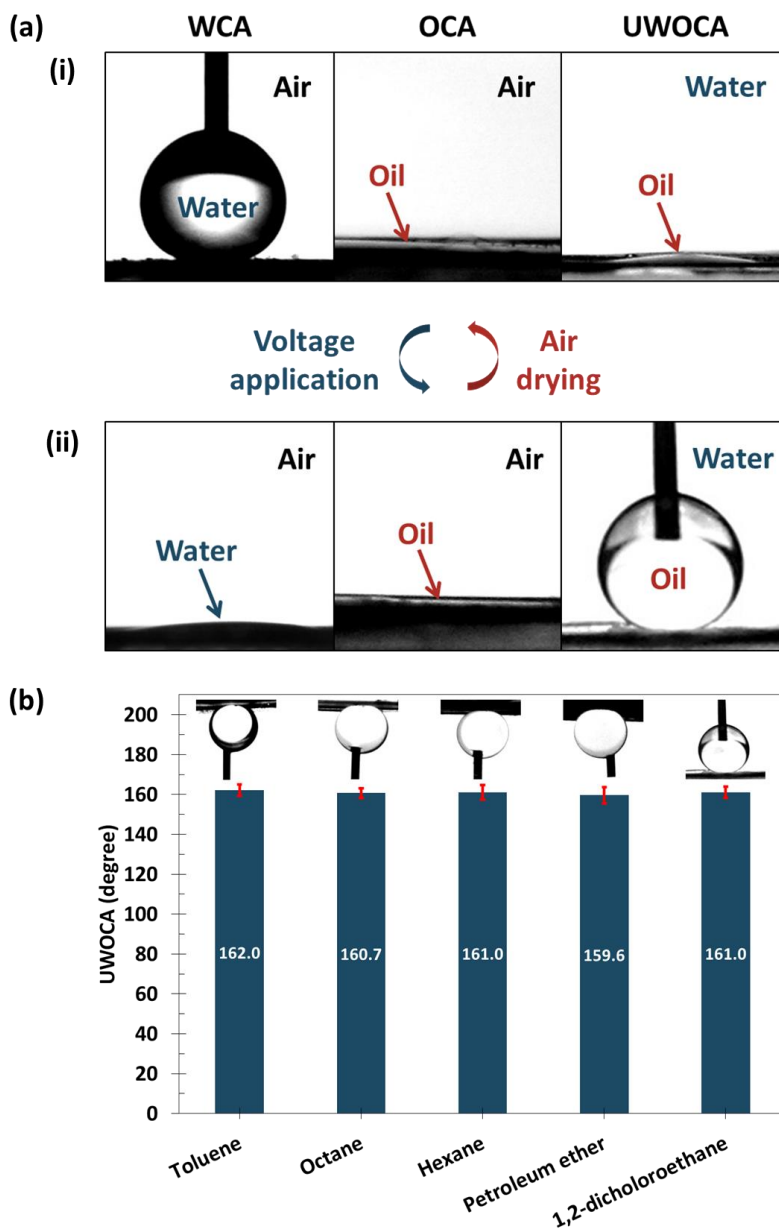


Figure 4.11: (a) The water contact angle (WCA), oil contact angle (OCA) and underwater oil contact angle (UWOCA) on the copper mesh after (a-i) air drying and (a-ii) voltage application. The OCA and UWOCA are determined using 1,2-dichloroethane. (b) High underwater oil contact angle (UWOCA) of different oils on the electrochemically modified copper mesh via voltage application illustrates the applicability of the mesh as a separator for oil of different densities and viscosities.

Following the application of reduction potential, the copper mesh exhibits superamphiphilicity in the air. As shown in Figure 4.11 (a-ii), the water and oil droplets instantaneously spread when brought into contact with the copper mesh, displaying WCA and OCA of $11.5 \pm 2.7^\circ$ and nearly 0° , respectively. In contrast to the strong affinity towards oil in the air, the copper mesh shows underwater superoleophobicity with UWOCA of $161.0 \pm 2.8^\circ$ in a water environment. The two extremes in the wettability range of the oil droplet in the air and in water can be described by the interfacial tension relations at the three-phase interface of the oil droplet^{348,349}:

$$\cos \theta_{ow} = \frac{\gamma_o \cos \theta_o - \gamma_w \cos \theta_w}{\gamma_{ow}} \quad (4.5)$$

In Equation (4.5), γ_o , γ_w and γ_{ow} represent the interfacial tensions of the oil-air, water-air, and oil-water interfaces, respectively; θ_o and θ_w are the OCA and WCA in the air; θ_{ow} is the UWOCA. For a hydrophobic and oleophilic surface, an underwater oleophilic property with $\theta_{ow} < 90^\circ$ is expected. This is in agreement with our experimental result shown in Figure 4.11 (a-i). The oil surface tension typically lies in the range of $20\text{-}30 \text{ mN m}^{-1}$, which is much lower compared to the water surface tension of 73 mN m^{-1} ³⁵⁰. As a result, the copper mesh exhibiting both superhydrophilicity and superoleophilicity in the air becomes superoleophobic underwater because the term $\gamma_o \cos \theta_o - \gamma_w \cos \theta_w$ is always negative. In general, a surface demonstrating a superhydrophilic behaviour in the air will present an underwater superoleophobic behaviour, which is an indirect outcome of the oil-water immiscibility³⁴². Physically, this behaviour arises as the water infiltrates and gets trapped between the dendritic structures due to high water affinity to reach a low-energy Wenzel state, as exemplified by the low WCA in Figure 4.11 (a-ii). The spontaneous formation of a continuous water film within the dendritic structure creates a barrier, minimizing the contact area between the copper mesh and the oil phase³⁵¹. The replacement of the water molecules on the mesh surface by oil molecules is energetically unfavourable due to repulsion between the oil and water phase^{345,352}. Therefore the superhydrophilic mesh surface is shielded from contacting the oil. Instead, the evolution of a spherical oil droplet is favourable to minimize the surface energy. The decrease in the contact area between the oil and copper mesh surface, in combination with the immiscibility between the polar water and non-polar oil phases, results in an amplified UWOCA^{350,353}.

After air drying for approximately an hour, the initial superhydrophobic-superoleophilic properties of the mesh are restored. The ease of wettability tuning between superhydrophobic-superoleophilic and superhydrophilic-superoleophobic (underwater) by alternate air drying and voltage application offers a mechanism for realizing selective removal of oil or water on a single filtration mesh. This can be achieved by smart switching between the wetting states to target the isolation of the oil phase from water or vice versa. The UWOCA of a series of oils, including toluene, octane, hexane and petroleum ether, was examined. The purpose of repeating the UWOCA measurement for different oils is to confirm that the underwater superoleophobic behaviour as shown in Figure 4.11 (a) arises independently of the viscosity and density of the oil phase. As confirmed in Figure 4.11 (b), the copper mesh possesses underwater superoleophobicity for different types of oil, and all the UWOCA values were higher than 160° . The universality in the underwater superoleophobic property towards different oils further corroborates the suitability of the copper mesh as a separator for a wide range of oils.

4.3.6.3 Electrochemical alteration of the surface oxidation state

The cyclic voltammetry (CV) and electrochemical impedance spectroscopy (EIS) were used as an in-situ technique to investigate the electrochemical wettability switching process. Figure 4.12 (a) shows the CV profile of the copper mesh in the as-deposited state over a potential range suitable for inducing the reduction process. The CV plot of the copper mesh resembles that obtained on the copper plate in Figure 4.6 (a). As described earlier, the two peaks A and B in Figure 4.12 (a) correspond to two distinct reduction processes on the as-deposited copper mesh, which can be described by Equation (4.3) and (4.4).

In the first step, the copper surface with the highest oxidation number (CuO) undergoes a partial reduction and is transformed into the Cu_2O phase (peak A). Upon continuous application of the reduction potential, the Cu_2O phase converts into the pure metallic Cu phase (peak B). On the other hand, the application of a positive potential leads to the oxidation of the surface to form CuO phase, as indicated by peak C in the CV profile (Figure 4.12 (a)). The transition of the wetting properties from the superhydrophobic to superhydrophilic state occurs during the electrochemical reduction of the mixed oxide surface to pure copper surface. The typical contact angle of a water droplet in the air before and after the transition is also shown in the inset of the CV curve (Figure 4.12 (a)).

EIS measurements were performed on the mesh surface before (superhydrophobic) and after the reduction (superhydrophilic) to elucidate the mechanism of the electrochemical switching and properties of the surface. Due to its real-time and non-invasive nature, EIS provides a means to probe the mesh-electrolyte interfacial interaction in-situ while preserving the surface properties. Figure 4.12 (b) and (c) show the EIS profile of the surface in both states in the form of Nyquist and Bode plots, respectively. The Nyquist plot of the superhydrophobic surface features a depressed semicircle, which could be attributed to double layer charging and charge transfer process on the hierarchical structure of the mesh ³⁵⁴. The impedance $|Z|$ value of the superhydrophobic surface is greater than that of the superhydrophilic surface over the entire frequency range (Figure 4.12 (c)). The high impedance $|Z|$ arises from the existence of trapped air pockets underneath the dendritic structure of the as-deposited mesh, which hinder penetration of electrolyte medium into the surface ³⁵⁵. The decrease in the impedance $|Z|$ following the electrochemical reduction also confirms the transition from Cassie-Baxter to Wenzel wetting state ³⁵⁶.

The EIS data were analyzed by fitting with the equivalent electrical circuits (EECs) shown in Figure 4.12 (d). Similar EECs have been used in several studies for elucidating the interfacial behaviour of electrode with and without film coating ^{354,357–359}. R_s is the ohmic resistance related to the ionic resistance of electrolyte solution, intrinsic resistance of the electrode material and the contact resistance at the interface of the electrode and current collector ³⁶⁰. R_{ct} is the interfacial charge transfer resistance, CPE_{dl} is the constant phase element corresponding to the double layer capacitance at the interface, R_f is the pore resistance associated with the ionic pathway through the oxide film, and CPE_f is the constant phase element corresponding to the capacitance of the copper oxide film ^{354,357}. Here the capacitance is substituted with the constant phase element (CPE) to account for the arc depression and non-ideal capacitive behaviour (deviation from the vertical line) observed in the Nyquist plot ^{358,361}. The use of CPE has been shown to provide a better approximation for rough electrode surface with distributed resistance and capacitance ^{357,362}. As shown in the Nyquist and Bode plots, there is a good agreement between experimental and simulated impedance spectra. Even though the copper oxide layer exhibits a lower electrical conductivity compared to the metallic copper, R_s of the superhydrophobic surface ($45.9 \Omega \text{ cm}^2$) is only higher than the reduced surface ($42.0 \Omega \text{ cm}^2$)

by about 9%. Indeed such a small difference in R_s is expected since the copper oxide phase is only present on the topmost layer of the mesh with metallic copper as the core phase. The R_{ct} and CPE_{dl} of the superhydrophobic surface are $74.8 \text{ k}\Omega \text{ cm}^2$ and $3.2 \text{ }\mu\text{F cm}^{-2}$, respectively. On the other hand, the superhydrophilic surface has R_{ct} of $1.7 \text{ k}\Omega \text{ cm}^2$ and CPE_{dl} of 1.3 mF cm^{-2} . In agreement with the literature, the R_{ct} value increases and the CPE_{dl} decreases with an increase in the surface hydrophobicity^{354,362}. The lower capacitance suggests a smaller electrode-electrolyte interfacial area whereas a higher R_{ct} is indicative of a surface with greater water repellency at which the electron transfer process is hindered^{363,364}. Prior to the electrochemical reduction, the Cu_xO (Cu_2O and CuO) surface film and trapped air layer in the dendritic structure act as a diffusion barrier between the electrolyte medium and metallic Cu surface. The minimal contact between the electrolyte and metal surface thus results in higher R_{ct} and lower CPE_{dl} ³⁵⁷. After reduction of the surface oxide layer, the electrolyte solution penetrates into the copper mesh structure and the contact area between the mesh surface and electrolyte increases. Subsequently, a lower R_{ct} and a higher CPE_{dl} are observed.

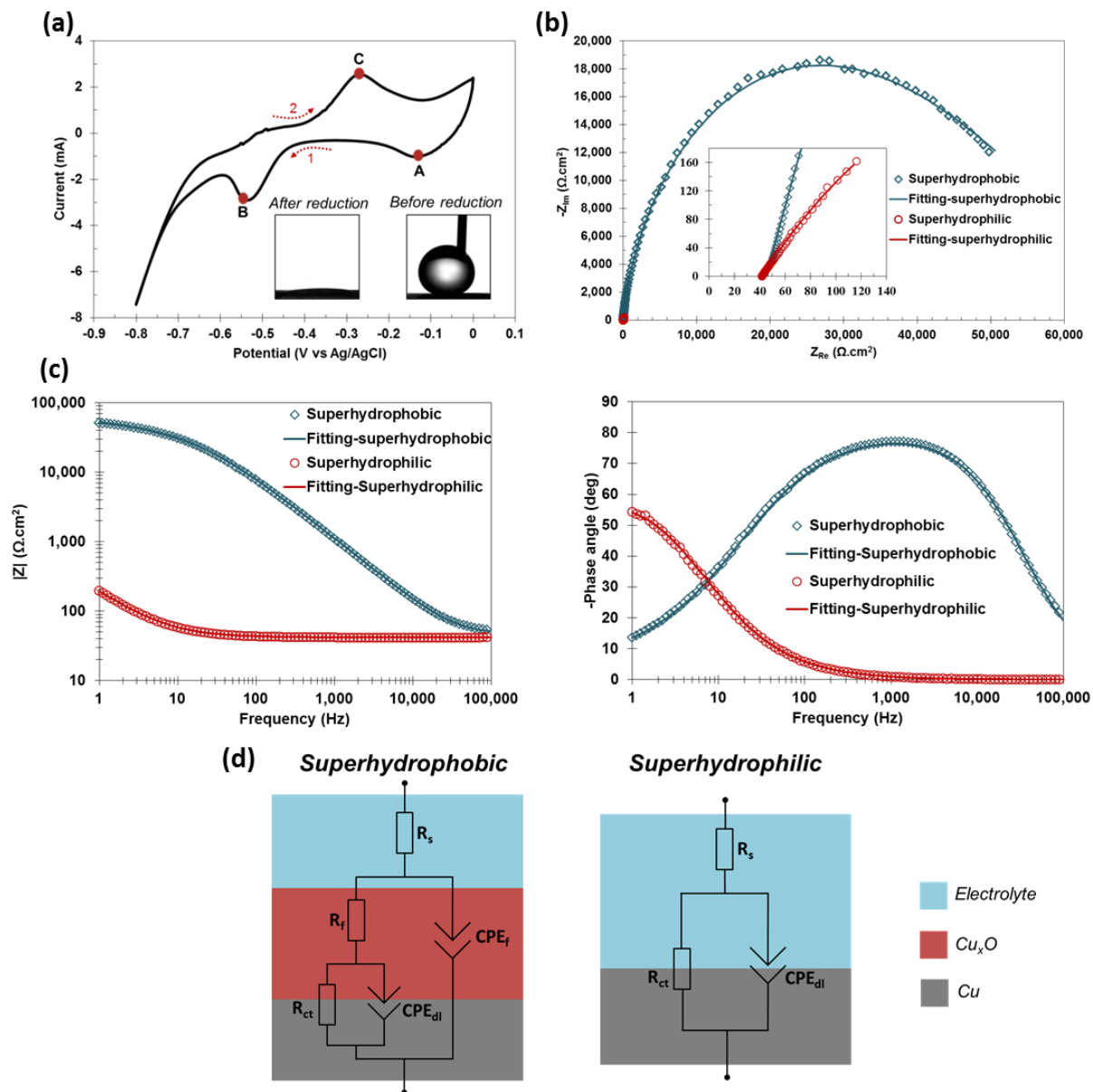


Figure 4.12: (a) CV profile the copper mesh over a reduction potential range of 0 to -0.8 V vs. Ag/AgCl reference. The inset shows the water contact angle of the mesh in the air before and after the electrochemical reduction. The mesh is superhydrophobic prior to the reduction reaction and turns superhydrophilic following voltage application of -1.5 V. The arrow 1 and 2 denote the forward scan from 0 V to -0.8 V and reverse scan from -0.8 to 0 V, respectively. (b) Nyquist and (c) Bode plots for the mesh surface before and after the reduction process at open circuit potential. (d) Equivalent electrical circuits used to model the impedance data of the superhydrophobic (before wetting transition) and superhydrophilic (after wetting transition) copper mesh surface.

4.3.6.4 Controllable oil-water separation in water-removing and oil-removing mode

In view of the selective superwetting-superantiwetting properties towards oil and water discussed in the previous section, the copper mesh can enable on-demand separation of light or heavy oils and water mixtures. The reversible switching between opposing wetting properties presents an opportunity to selectively remove oil or water from oil-water mixtures by operating in either oil-removing or water-removing states, depending on the relative density of the oil and water phase. When the oil phase to be separated is denser than the water phase, the superhydrophobic/superoleophilic nature of the as-deposited or air-dried copper mesh can be exploited for selective separation of heavy oil from water. The heavy oil will pass through the copper mesh due to its superoleophilic nature while the water will be intercepted. The superhydrophilic-underwater superoleophobic properties are not optimal in this case as the heavy oil tends to settle below the water, forming a barrier layer that hinders water permeation³⁶⁵. On the other hand, the concurrent superhydrophilicity and underwater superoleophobicity of the electrochemically altered copper mesh are ideal for separation of light oil-water mixture. The water accumulated in the bottom layer would permeate while the oil phase would be retained above the mesh. Accordingly, both types of separation could be achieved by smart tuning of the wettability of the copper mesh.

A series of proof-of-concept studies were carried out to assess the oil-water separation capability of the copper mesh. For separating the heavy oil from water, the heavy oil-water mixture was poured onto the as-deposited copper mesh without further modification or onto the air-dried mesh. As shown in Figure 4.13 (a), the heavy oil (dyed by Oil red O) permeates due to superoleophilicity of the nanostructured layer while the water (dyed by methylene blue) is retained in the upper funnel because of the superhydrophobicity of the copper mesh. To separate water from light oil, a reduction potential of 1.5 V is applied to alter the wettability of the copper mesh via electrochemical transformation of the oxidation state of the copper oxide shell. The current profile of the mesh during this transition is shown in Figure 4.13 (c). The initial increase in the magnitude of the current is due to the increasing dendritic surface area in contact with the water as the reduction reaction occurs and electrolyte penetrates into the roughness feature. Owing to the superhydrophilicity and underwater superoleophobicity of the electrochemically

reduced copper mesh, the mesh is permeable to water but not to oil. Therefore, water will pass through while the oil will be blocked. In both cases, the separation process is solely driven by the gravity without the application of external force. Through the facile control over the selective permeation of oil or water, the copper mesh can be adapted to separate different oil-water mixtures with different densities and viscosities.

For practical applications (e.g., oily wastewater cleanup), the mesh must possess the flexibility to initiate the separation process on-demand with simple operating procedures. Figure 4.13 (b) shows a series of images illustrating the capability of the copper mesh for continuous on-demand oil-water separation. Prior to the application of voltage, the oil-water mixture stays on the mesh and the water (or 1 M Na_2SO_4 electrolyte) with higher density is at the bottom layer. Upon application of reduction potential, the water permeates through the mesh instantaneously. The light oil that remains on the mesh can then be collected separately. The voltage input can be turned off at this stage since the copper mesh has completed the transition from the oil-removing to the water-removing state. In addition, the separation process can be reactivated by pouring more oil-water mixture into the existing batch, initiating the next separation cycle. As shown in Figure 4.13 (b), the mesh only allows the newly added water to pass through while repelling the oil. Subsequently, the separation process can be repeated for multiple cycles as required, eliminating the need for any regeneration or cleaning steps.

The quality of the separation process is quantified using the separation efficiency, which is determined based on the mass ratio of the rejected phase before and after the separation (Equation (4.1)). The mixture of heavy oil (1,2-dichloroethane) and water was separated using the as-deposited or air-dried copper mesh operating in the oil-removing mode. The light oil-water mixture was separated using copper mesh in the water-removing mode. Figure 4.13 (d) shows that the separation efficiency of all the light oil-water and heavy oil-water mixtures are higher than 98%. The high separation efficiency can be attributed to the distinctive wetting behaviour towards oil and water.

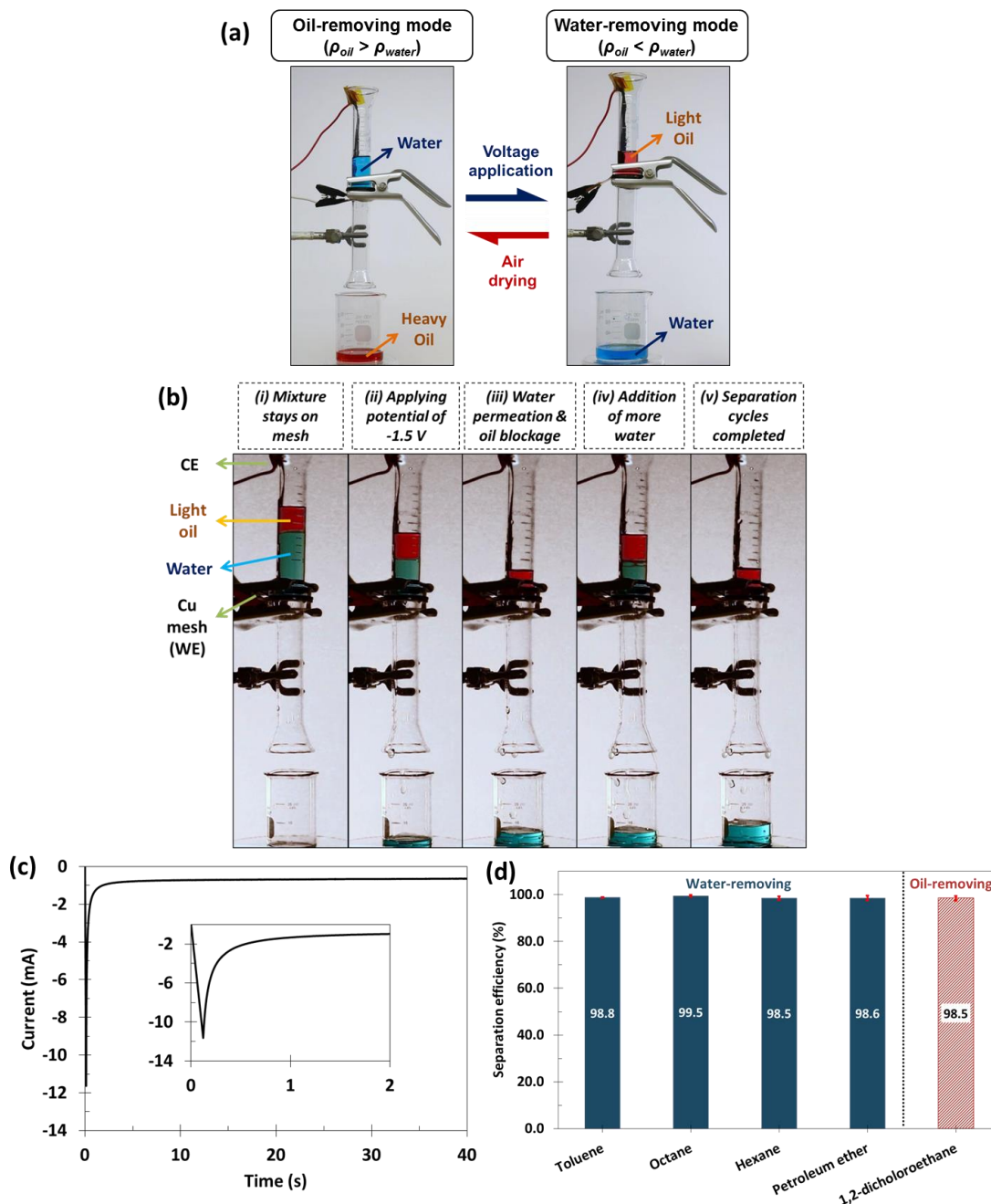


Figure 4.13: (a) Reversible oil-water separation in oil-removing and water-removing mode triggered by air drying and voltage application (b) Series of images illustrating the on-demand separation of light oil-water mixture via voltage application and the use of the mesh for multiple separation cycles. CE and WE stand for counter and working electrodes, respectively. (c) The current profile of the mesh as it undergoes the wetting transition following application of reduction voltage of 1.5 V. (d) Separation efficiency of the copper mesh operating in both water-removing and oil-removing modes are higher than 98% for different oil-water mixtures.

4.3.6.5 Mechanism of selective removal of water and oil

One of the pivotal aspects of the oil-water separation system is the on-demand alteration of the surface wettability. The ability to switch between superhydrophobic-superoleophilic and superhydrophilic-superoleophobic behaviour allows the separation of heavy oil and water as well as light oil and water. Mechanistically, the overall effectiveness of the mesh in separating oil and water arises from the interplay of the morphologies from the woven wires and the dendritic structures. The multiscale roughness plays an essential role in the observed water- and oil-repelling qualities^{366,367}. When the material is in the phobic state (hydrophobic or oleophobic), the re-entrant structure arising from the circular cross-section of the wires leads to an enhanced phobic state for both water and oil³⁶⁸. In addition, the nano- and microscale roughness originating from the hierarchical dendrites minimize the solid-liquid contact area by retaining air pockets, thus impeding liquid propagation.

The separation process in oil-removing and water-removing modes is shown schematically in Figure 4.14. The as-prepared mesh demonstrates a superhydrophobic behaviour in agreement with the condition of the Cassie-Baxter wetting state. This implies that the water is suspended on top of the dendritic structures and there exists a cushion of air underneath the water phase. When a mixture of water and heavy oil is poured into the separation vessel, the heavy oil will sink at the bottom due to its higher density until it touches the mesh. As the oil comes in contact with the solid surface, the oil phase spreads on the wireframe of the mesh due to the capillary wicking (hemi-wicking) and eventually penetrates the mesh. The heavy oil permeates through the mesh not by overcoming the trans-membrane pressure, but by wicking-assisted spreading^{346,347}. As the spreading occurs, the gravity acts on the droplet forming on the bottom side of the mesh leading to the oil droplet detachment, which is governed by the balance between the surface tension and gravity. Any external stimuli do not instigate the separation in the oil-removing mode. Following the oil permeation, the hierarchical dendrites would be infused with a thin film of oil molecules (Figure 4.14 (a)). Accordingly, the water layer on top of the oil does not come in contact directly with the underlying solid surface but with an oil film. The immiscibility of the oil and water restricts any further passage of water through the mesh. This effect regulates the selective oil permeation while blocking the water access. Although the oil film shielding the dendritic structure is not recovered, the trapped oil is not a recurring loss. For

any further separations, the oil permeation takes place once the oil comes in contact with the impregnated oil film. Therefore the efficiency is not affected during continuous operation of the separation process.

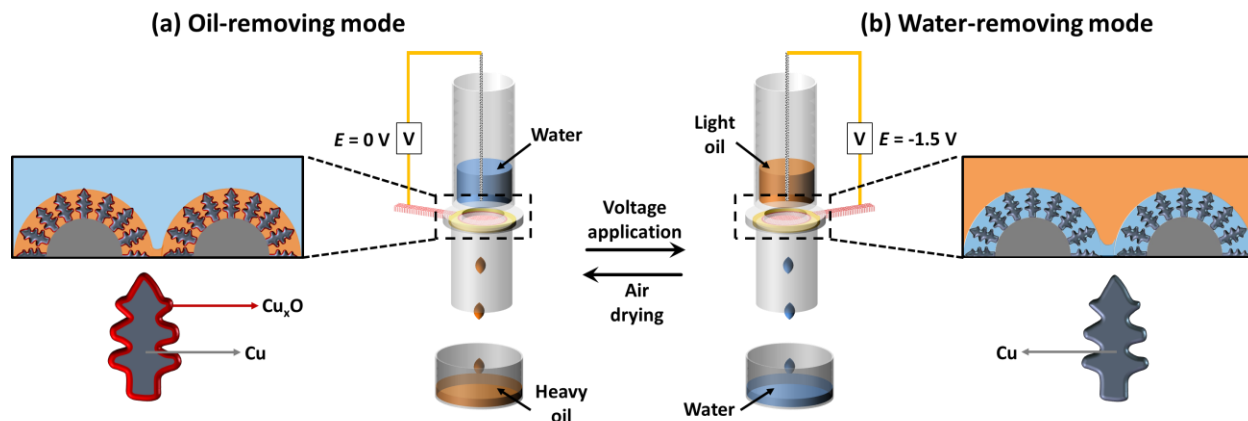


Figure 4.14: Schematic illustration of the separation process of (a) heavy oil-water mixture in oil-removing mode and (b) light oil-water mixture in water-removing mode. In both oil-removing and water-removing modes, liquid permeation begins by capillary-driven wicking into the dendritic structures followed by gravity-assisted flow through the mesh. At the end of the separation, the dendrite surface is infused with a thin film of oil (water) that restricts penetration of water (oil).

While the separation of the heavy oil and water mixture occurs without any external stimuli, the separation of the light oil-water mixture can be assisted via electrical stimuli. The light oil with lower density floats on top of the water layer when a light oil-water mixture is poured into the separation vessel. Since the surface is in the superhydrophobic Cassie-Baxter state, the water is supported on the mesh. At this stage, none of the liquids are permeating through the mesh. The electrochemical switching of the wettability of the mesh is induced by applying a reduction potential of 1.5 V, initiating the separation process. Following the voltage application, the oxide species on the surface (Cu_xO) get converted into the metallic phase (Cu) as an outcome of the electrochemical reduction. In response to the change in the surface chemistry, the water layer first imbibes the dendritic structure, leading to a transition from the Cassie-Baxter to the Wenzel wetting state. After this transition, the macroscopic three-phase contact line advances along the curved surface of the wire and forms a continuous water film. The movement of the water through the dendritic structures resembles that of the wicking mechanism with the

distinction of being assisted by the electrical potential, which causes the water to move through the capillary network formed by the dendritic structures³⁴⁶. The water propagates through the wire surface and emerges on the bottom side of the mesh. As the water accumulates at the bottom, gravity overcomes the tension forces, and the water is removed as drops. Some residual water is left impregnating the surface of the dendrites after the water is completely drained. The oil layer that eventually contacts the water-impregnated dendritic structures would not be able to permeate due to the repulsion between the oil and water phases (Figure 4.14 (b)). The behaviour is the inverse of what is observed for the separation of the heavy oil and water where oil-impregnated dendritic structures prevent the passage of water.

The gravity-driven separation processes have low energy consumption. The oil-water separation process and the permeation occur not by overcoming the trans-membrane pressure, but by the solid-liquid interfacial interactions. Nevertheless, gravity does serve a few essential functions, such as the layer formation for the two immiscible liquids (oil and water) based on their difference in density, and the droplet detachment from the underside of the mesh once the liquid has permeated the mesh structure.

4.3.6.6 Recyclability of copper mesh

The recyclability and durability of the copper mesh were evaluated through the measurement of contact angle and separation efficiency for 30 consecutive cycles. The WCA in air or UWOCA was obtained before each separation test to verify the reversibility of the wetting state. Figure 4.15 (a) shows that the wetting transition between superhydrophobicity and underwater superoleophobicity is fully reversible by consecutive air drying and voltage application. In the oil-removing mode, the WCA remains consistently above 160° with a slight fluctuation of 4%. Moreover, the mesh fully regains the underwater superoleophobicity after voltage application. The UWOCAs of the electrochemically altered copper mesh are above 158° with a variation of 5% for all water-removing cycles. In line with the reversible transition in the WCA and UWOCA, the mesh retains high separation efficiency exceeding 98% for multiple separation cycles in both oil-removing and water-removing states (Figure 4.15 (b)). The high recyclability of the copper mesh lies upon the structural integrity of the dendrites and chemical reversibility of the topmost oxide layer. As shown in Figure E1, the surface microstructure and chemical composition of the copper mesh after the wetting transition cycles are similar to that of

the as-deposited mesh. The stability of the wetting behaviour and separation efficiency demonstrate the reusability of the copper mesh.

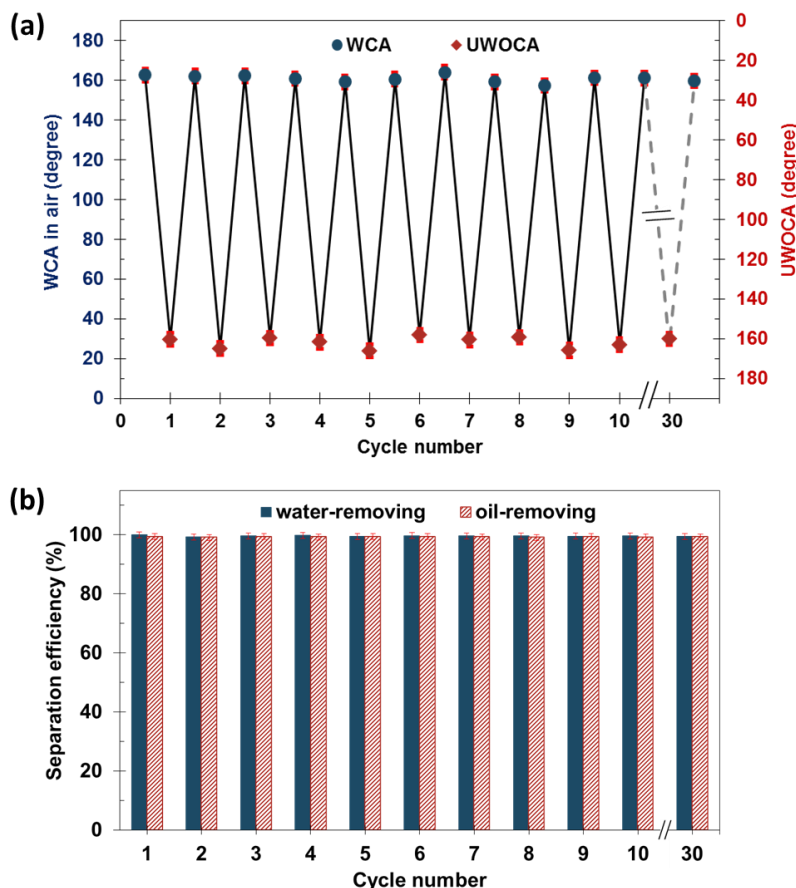


Figure 4.15: (a) WCA in air and UWOCA for 30 cycles of reversible transition between superhydrophobic/superoleophilic and superhydrophilic/underwater superoleophobic states induced by alternate air drying and voltage application. (b) The separation efficiency of the copper mesh in water-removing and oil-removing mode for 30 separation cycles. Toluene and 1, 2-dichloroethane are used as the representative light and heavy oil, respectively.

4.4 Summary

A facile approach for electrochemical alteration of the surface wettability of electrodeposited copper structures was demonstrated. By varying the copper oxidation state, the entire wettability range spanning superhydrophobicity (contact angle $> 150^\circ$) to superhydrophilicity (contact angle $< 10^\circ$) can be precisely adjusted in-situ. During the wetting transitions, the surface transforms from a low adhesive rolling state (lotus effect) to high

adhesive pinning state (petal effect), and eventually to superhydrophilic state with a water-absorbing ability (fish scale wetting). The wetting alteration was found to be reversible and the original hydrophobic behaviour was retained after multiple cycles of wetting alterations. The reversal to the initial superhydrophobicity was achieved by either leaving the sample in ambient air for an hour or by mild heat drying at 100 °C for 30 min. A combination of surface and structure characterization revealed the presence of mixed oxide species (CuO and Cu₂O) on the as-prepared samples as well as the cycled samples. The electrochemical wettability modulation involves reduction of the surface-bound oxide groups into their metallic counterpart as corroborated by the cyclic voltammetry. The mechanism was found to be distinct from the low-voltage electrowetting, which is governed by charge accumulation at the solid-liquid interface.

The switchable wetting properties of the core-shell copper-copper oxide structure were further applied in the preparation of a copper mesh for on-demand separation of heavy oil-water and light oil-water mixtures. The as-deposited mesh possesses simultaneous superhydrophobic and superoleophilic behaviour suitable for selective removal of heavy oil from water. Upon application of small electrochemical reduction voltage (<1.5 V), the mesh becomes superhydrophilic and underwater superoleophobic, which is ideal for water permeation while blocking the flow of light oil. The wettability of the copper mesh can be tuned between superhydrophobic-superoleophilic and superhydrophilic-underwater superoleophobic by air drying and voltage application. Extensive microstructural characterization revealed that the composition of the outmost surface, as well as the roughness features of the dendrites, play a key role in achieving the switchable wetting and oil-water separation. The underlying mechanism of the wetting transition was elucidated based on the Cassie-Baxter and Wenzel theories. The separation efficiency of the system operating under both oil-removing and water-removing states is higher than 98% for a series of oil-water mixtures. Moreover, the mesh retains the wetting behaviour and high separation efficiency after 30 consecutive cycles of oil-water separation.

5 Conclusions and future considerations

5.1 Conclusions

The conventional method for surface wettability evaluation is based on measurement of contact angle at the solid-liquid-air interface. Although the contact angle measurement provides a fast and cost-effective tool for wettability characterization, the application of contact angle as wettability parameter poses several limitations, including the multiplicity of contact angle values for a rough surface, the elusive role of the contact area and contact line, and droplet size dependence of the contact angle values. These complications in the optical wettability characterization have resulted in the discrepancy in the experimental results and theoretical predictions. For practical applications, different types of wetting behaviour are desired. For example, the gas diffusion layer in the hydrogen fuel cell is typically coated with a hydrophobic agent to prevent water flooding. On the other hand, a hydrophilic surface is favourable in water electrolysis application to maximize the electrode-electrolyte contact area and to minimize gas bubble blocking. As such, a thorough understanding of wetting phenomena would facilitate the development of the structure-property-function relationship to prescribe the design of functional materials with special wettability. In view of the limitations of contact angle, there is a need for a robust wettability characterization technique and wetting metric.

Thanks to the advances in material processing and fabrication technology, a large number of artificial surfaces with different wetting properties have been synthesized. In general, there are two ways to control the surface wettability: the passive and active means. The passive wetting tuning involves modification of the surface morphology and chemical composition. Nevertheless, the obtained wettability is static in nature. In other words, the wetting behaviour of the material cannot be changed unless further surface modification steps are applied. Dynamic control over the wettability is desirable in applications such as microfluidic tools, lab-on-chip devices, and smart membranes. For such active wettability alteration, smart surfaces showing adaptive properties upon external stimulation are used. Despite extensive progress, several aspects of the switchable materials and approaches entail further study for scale-up applications. Among them are the complexity and cost of the fabrication process, use of the chemical additive, the range of wettability conversion, contact angle switching speed, and time required for wetting recovery.

In an attempt to resolve the aforementioned challenges, this thesis describes the use of electrochemical approaches to quantify the surface wettability and to achieve smart control over the wetting behaviour of copper oxide surface. In Chapter 3, an experimental platform for wettability characterization based on the double layer capacitance is presented. The electrochemical technique utilizes the proportionality between the electric double layer capacitance and solid-liquid interfacial area to evaluate the wetted area under the droplet. In comparison to the conventionally used contact angle measurement, the electrochemical approach is more sensitive towards change in the surface roughness. In the proof-of-concept experiment based on intrinsically hydrophobic surfaces, the contact angle results showed that the increase in the surface wettability can be predicted by either the Cassie-Baxter (heterogeneous wetting) or Wenzel (homogeneous wetting) model. Using the electrochemically derived solid-liquid interfacial area as wettability metric, the Wenzel model was identified to be a better representation of the wetting behaviour.

In another study using mechanically polished surfaces, the static and dynamic contact angle results show contradictory wetting behaviour. Compared to the intrinsically hydrophilic smooth surface, the static contact angle of mechanically abraded rough samples increased, suggesting the Cassie-Baxter wetting state. However, the dynamic contact angle measurements hinted towards the Wenzel state because an increase in the contact angle hysteresis values with roughness was observed. The electrochemical evaluation revealed an increase in the wetted area with the roughness scale, which is in line with the contact angle hysteresis trend. Therefore, by coupling the electrochemical and optical analysis, we have successfully unveiled the interfacial interaction between the liquid and solid surface. The results can also aid in the elucidation of the ongoing debate in the surface scientific community over the role of interfacial area and three-phase contact line, as well as the validity of the Wenzel and Cassie-Baxter wetting models. We have provided experimental evidence that the apparent contact angle has a rather weak dependence on the area under the droplet. Instead, the three-phase contact line controls the apparent contact angle on a rough surface. Overall, the studies demonstrate the potential use of the electrochemical approach as a complementary characterization tool to the optical methods.

Chapter 4 describes an electrochemical approach for dynamic control over the wetting behaviour of the electrodeposited copper structure. The copper-copper oxide core-shell structure

was synthesized using a controllable, cost-effective, and scalable electrochemical deposition process without any chemical additive. The magnitude and duration of applied reduction voltage control precisely the rate and extent of the contact angle reduction. By manipulating the oxidation state of the oxide shell phase, the entire wettability range from superhydrophobicity (contact angle $> 150^\circ$) and superhydrophilicity (contact angle $< 10^\circ$) can be precisely controlled in-situ within a few seconds to a few minutes. The electrochemical analysis shows that the wetting transition is based on the Faradaic phase transformation of the surface-bound oxide groups to the metallic counterpart. Moreover, the wetting alteration is reversible by air-drying at room temperature for an hour or by mild heat drying at 100°C for 30 min. In comparison to other potential-induced wetting alteration such as electrowetting, the approach presented in this thesis controls the surface wettability by changing the surface chemistry. The rate of the electrochemical reduction of the surface oxide is determined by the applied reduction voltage. Thus there is a high level of controllability over the wetting state, which could be accomplished with relatively low voltage ($<1.5\text{ V}$) operable by the conventional alkaline battery.

The reversibly redox-driven wettability conversion is demonstrated for controllable separation of oil-water mixtures. The as-deposited copper mesh possesses simultaneous superhydrophobic and superoleophilic behaviour suitable for selective removal of heavy oil from water. Upon application of small electrochemical reduction voltage ($<1.5\text{ V}$), the mesh becomes superhydrophilic and underwater superoleophobic, which is ideal for water permeation while blocking the light oil. As a result, the mesh can be tuned between the oil-removing and water-removing mode through air drying and voltage application for selective removal of light or heavy oil. The underlying mechanism of the wetting transition and oil-water separation was explained based on the Cassie-Baxter and Wenzel wetting models. In addition, the mesh retains the wetting properties and separation efficiency of over 98% after 30 consecutive cycles of oil-water separation. Owing to the simple preparation procedure, ease of wetting transition, and durability of the copper structure, the mesh has the potential to be used for oily wastewater treatment, fuel purification, and oil spills clean up.

5.2 Future work and recommendations

The findings presented in this work have unveiled several areas that worth further investigations to expand the potential of the electrochemical technique. The following are the recommendations for future studies:

- **Application of electrochemical wettability metric for characterization of porous materials**

Porous carbon fibre substrate is used in many electrochemical conversion and storage technologies, such as fuel cell, supercapacitor, and redox flow battery. Conventional methods to study the solid-liquid interaction in the porous structure often require highly specialized equipment or lack the sensitivity in detecting a difference in the internal structure. Thus the successful extension of the electrochemical wettability metric and characterization method for porous carbon material would provide the avenue for enhancing the performance in these technologies. Similar to the glassy carbon substrate used in this work, the carbon fibre substrate is conductive and can support the formation of the electric double layer. Accordingly, a similar parameter based on the double-layer capacitance could potentially be applied with minor modifications. The high sensitivity of the electrochemical technique towards the surface properties, as demonstrated in this thesis, would also facilitate the study of wetting dynamics in porous materials.

- **Application of plasma treatment technique for surface wettability modification**

The plasma treatment method was used to prepare uniformly distributed nanoscale roughness feature on the glassy carbon substrates in this work. In addition to the roughness contribution, it was found that the surface can also be rendered hydrophobic while preserving the surface morphology through deposition of fluorine-containing groups (e.g. SF₆, CF, CF₂, CF₃). Thus there is a potential to fine-tune the surface wettability by controlling the process parameters, such as the treatment time, process gas type, flow rate, and power. Our initial attempt on fibrous carbon layer used in the hydrogen fuel cell indicated that the plasma modification is effective in creating water removal pathway, thus boosting the performance at high current load.

- **Comparison of the effective area determination based on double layer capacitance and measurement using redox probe**

This thesis work describes the measurement of double layer capacitance to infer the wetting behaviour through determination of the solid-liquid interfacial area. Another electrochemical method that can be used to estimate the effective area is based on an evaluation of the peak current of well-characterized redox reaction using the Randles-Sevcik equation. An example of such a redox probe is the ferrocene/ferrocenium couple. Gira et al. have shown that the measurement on metal thin films based on the redox couple tends to underestimate the surface area due to the convolution effect of diffusion layer thickness for rough samples. In order to establish the electrochemical technique as a tool for wettability characterization, there is a need to perform a systematic comparison of the measurements based on double layer capacitance and redox probe on different systems, including the carbonaceous, metallic and oxide surfaces. Extension of the electrochemical methods to study surfaces with more complex morphologies would also facilitate the establishment of structure-property relationship to guide the design and development of artificial wetting systems.

- **Integration of double layer capacitance evaluation with impedance measurement for probing intermediate wetting state and quantification of effective wetted area**

While the comparison of the capacitance values offers insight on the solid-liquid interfacial interaction under the droplet, it does not allow quantification of the liquid penetration depth. In particular, the increase in the interfacial area shown in Section 3.3 may represent partial liquid penetration with air pockets still trapped underneath the roughness feature. Due to lack of a robust wetting model for describing the intermediate wetting state, only the cases of non-penetration (Cassie-Baxter) and complete penetration (Wenzel) are considered in this study. Tuberquia et al. have demonstrated the application of electrochemical impedance spectroscopy (EIS) to determine the liquid penetration depth³⁵⁶. Combination of the impedance-based method with the double layer capacitance measurement presents the opportunity to monitor in real time the wetting state and to quantify the effective wetted area.

- **Investigation of different transition metal oxide surfaces for wetting switching based on oxidation state transformation**

This work has demonstrated the wettability switching on the electrodeposited copper surface by controlling the oxidation state. Copper is used as the model substrate for this

study due to its low cost and abundance. Similar wetting alteration could possibly be observed on other transition metal oxides or mixed oxides which exhibit multiple oxidation states. A systematic study on the intrinsic wettability of different oxidation states of various oxides is needed.

- **Exploring applications of low-voltage redox-driven wettability switching**

Stimuli-responsive materials with controlled reversible wettability find diverse technological applications in microfluidic devices, lab-on-a-chip systems, and smart membrane. Compared to other wetting alteration methods, the electrochemical approach presented in this thesis has the advantages of low switching requirement, fast response, and high controllability. Therefore it is of interest to investigate the use of the electrochemical switching technique in other areas.

- **Optimization of mesh structure for separation efficiency and capacity**

A systematic design of the membrane structure is required to optimize the permeation rate and separation efficiency. Several studies have revealed the contradictory impact of pore size on the separation process^{369–371}. The flux increases with the pore size, thus generating a greater separation capacity. However, a larger pore size reduces the breakthrough pressure. The breakthrough pressure characterizes the maximum height of the repelled phase that the membrane can support. Subsequently, the decrease in the maximum supporting height leads to lower separation efficiency due to undesired infiltration of the repelled phase and limits the applicability of the oil-water separator.

- **Large-scale field testing of smart oil-water membrane**

The smart copper membrane described in Chapter 4 showed that the mesh retains high separation efficiency after 30 wetting cycles. However, for scale-up application, it is necessary to investigate the durability of the membrane under actual-use testing conditions. The stability of the mesh under harsh environmental conditions (elevated temperature and corrosive solution) needs to be evaluated. The operation of the membrane in continuous mode also needs to be tested to meet the target treatment capacity for industrial requirements. In addition, evaluation of the membrane separation technology for industrial uses entails a comprehensive techno-economic analysis.

Bibliography

1. Bonn, D., Eggers, J., Indekeu, J. & Meunier, J. Wetting and spreading. *Rev. Mod. Phys.* **81**, 739–805 (2009).
2. Israelachvili, J. N. *Intermolecular and surface forces*. (Academic Press, 2011).
3. Molnar, I. L., O'Carroll, D. M. & Gerhard, J. I. Impact of surfactant-induced wettability alterations on DNAPL invasion in quartz and iron oxide-coated sand systems. *J. Contam. Hydrol.* **119**, 1–12 (2011).
4. Prabhu, K. N., Fernades, P. & Kumar, G. Effect of substrate surface roughness on wetting behaviour of vegetable oils. *Mater. Des.* **30**, 297–305 (2009).
5. Kubiak, K. J., Wilson, M. C. T., Mathia, T. G. & Carval, P. Wettability versus roughness of engineering surfaces. *Wear* **271**, 523–528 (2011).
6. Jackson, R. G. *et al.* Effect of surface wettability on carbon nanotube water-based nanofluid droplet impingement heat transfer. *J. Phys. Conf. Ser.* **525**, 012024 (2014).
7. Banerjee, S., Dionysiou, D. D. & Pillai, S. C. Self-cleaning applications of TiO₂ by photo-induced hydrophilicity and photocatalysis. *Appl. Catal. B Environ.* **176–177**, 396–428 (2015).
8. Kwok, D. Y. & Neumann, a. W. *Contact angle measurement and contact angle interpretation. Advances in Colloid and Interface Science* **81**, (1999).
9. Sharma, P. K. & Hanumantha Rao, K. Analysis of different approaches for evaluation of surface energy of microbial cells by contact angle goniometry. *Adv. Colloid Interface Sci.* **98**, 341–463 (2002).
10. Chung, J. Y., Youngblood, J. P. & Stafford, C. M. Anisotropic wetting on tunable micro-wrinkled surfaces. *Soft Matter* **3**, 1163 (2007).
11. Marmur, A. Soft contact: measurement and interpretation of contact angles. *Soft Matter* **2**, 12 (2006).

12. Verplanck, N., Coffinier, Y., Thomy, V. & Boukherroub, R. Wettability switching techniques on superhydrophobic surfaces. *Nanoscale Res. Lett.* **2**, 577–596 (2007).
13. Dorrer, C. & R??he, J. Drops on microstructured surfaces coated with hydrophilic polymers: Wenzel’s model and beyond. *Langmuir* **24**, 1959–1964 (2008).
14. Lamour, G. *et al.* Contact angle measurements using a simplified experimental setup. *J. Chem. Educ.* **87**, 1403–1407 (2010).
15. Garai, R. M. *et al.* Study on the effect of raw material composition on water-repellent capacity of paraffin wax emulsions on wood. *J. Dispers. Sci. Technol.* **26**, 9–18 (2005).
16. Zhang, F. & Low, H. Y. Anisotropic wettability on imprinted hierarchical structures. *Langmuir* **23**, 7793–7798 (2007).
17. Khandekar, S., Panigrahi, P. K., Lefèvre, F. & Bonjour, J. Local Hydrodynamics of Flow in a Pulsating Heat Pipe: a Review. *Front. Heat Pipes* **1**, (2010).
18. Law, K. Definitions for Hydrophilicity, Hydrophobicity, and Superhydrophobicity: Getting the Basics Right. *J. Phys. Chem. Lett.* **5**, 686–688 (2014).
19. Gao, L. & Mccarthy, T. J. Teflon is hydrophilic. commnets on definitions of hydrophobic, shear versus Tensile Hydrophobicity , and Wettability Characterization. **24**, 9183–9188 (2008).
20. Amirfazli, A. & Neumann, A. W. Status of the three-phase line tension: A review. *Adv. Colloid Interface Sci.* **110**, 121–141 (2004).
21. Lin, F. Y. H. & Li, D. The effect of surface heterogeneity on the drop size dependence of contact angles. *Chem. Eng. Sci.* **50**, 2633–2639 (1995).
22. Marmur, A. Wetting on hydrophobic rough surfaces: To be heterogeneous or not to be? *Langmuir* **19**, 8343–8348 (2003).
23. Meiron, T. S., Marmur, A. & Saguy, I. S. Contact angle measurement on rough surfaces. *J. Colloid Interface Sci.* **274**, 637–644 (2004).

24. Aksay, I. a., Hoge, C. E. & Pask, J. a. Wetting under chemical equilibrium and nonequilibrium conditions. *J. Phys. Chem.* **78**, 1178–1183 (1974).
25. Marmur, A. Soft contact: measurement and interpretation of contact angles. *Soft Matter* **2**, 12–17 (2006).
26. Marmur, A. Hydro- hygro- oleo- omni-phobic? Terminology of wettability classification. *Soft Matter* **8**, 6867 (2012).
27. Vafaei, S. & Podowski, M. Z. Analysis of the relationship between liquid droplet size and contact angle. *Adv. Colloid Interface Sci.* **113**, 133–146 (2005).
28. Zhang, X., Wang, L. & Levänen, E. Superhydrophobic surfaces for the reduction of bacterial adhesion. *RSC Adv.* **3**, 12003 (2013).
29. Young, T. An Essay on the Cohesion of Fluids. *Philos. Trans. R. Soc. London* **95**, 65–87 (1805).
30. Nakajima, A. Design of hydrophobic surfaces for liquid droplet control. *NPG Asia Mater.* **3**, 49–56 (2011).
31. Ruiz-Cabello, F. J. M., Rodriguez-Valverde, M. A. & Cabrerizo-Vilchez, M. A. Equilibrium contact angle or the most-stable contact angle? *Adv. Colloid Interface Sci.* **206**, 320–327 (2014).
32. Bhushan, B. & Jung, Y. C. Micro- and nanoscale characterization of hydrophobic and hydrophilic leaf surfaces. *Nanotechnology* **17**, 2758–2772 (2006).
33. Chen, S., Wang, J. & Chen, D. States of a water droplet on nanostructured surfaces. *J. Phys. Chem. C* **118**, 18529–18536 (2014).
34. Butt, H.-J., Graf, K. & Kappl, M. *Physics and Chemistry of Interfaces*. (Wiley-VCH Verlag GmbH & Co. KGaA, 2003). doi:10.1002/3527602313
35. Wenzel, R. N. Resistance of solid surfaces to wetting by water. *J. Ind. Eng. Chem. (Washington, D. C.)* **28**, 988–994 (1936).

36. Cassie, A. B. D. & Baxter, S. Wettability of porous surfaces. *Trans. Faraday Soc.* **40**, 546 (1944).
37. Dorrer, C. & R uhe, J. Some thoughts on superhydrophobic wetting. *Soft Matter* **5**, 51 (2009).
38. Feng, X. & Jiang, L. Design and creation of superwetting/antiwetting surfaces. *Adv. Mater.* **18**, 3063–3078 (2006).
39. Wolansky, G. & Marmur, A. Apparent contact angles on rough surfaces: The Wenzel equation revisited. *Colloids Surfaces A Physicochem. Eng. Asp.* **156**, 381–388 (1999).
40. Bahadur, V. & Garimella, S. V. Electrowetting-based control of static droplet states on rough surfaces. *Langmuir* **23**, 4918–4924 (2007).
41. Qu er , D. Non-sticking drops. *Reports Prog. Phys.* **68**, 2495–2532 (2005).
42. Gennes, Pierre-Gilles de; Brochard-Wyart, Fran oise; Qu er , D. *Capillarity and Wetting Phenomena: Drops, Bubbles, Pearls, Waves.* (Springer, 2004). doi:10.1007/978-0-387-21656-0
43. Good, R. J. A Thermodynamic Derivation of Wenzel’s Modification of Young’s Equation for Contact Angles; Together with a Theory of Hysteresis. *J. Am. Chem. Soc.* **74**, 5041–5042 (1952).
44. Bico, J., Thiele, U. & Qu er , D. Wetting of textured surfaces. *Colloids Surfaces A Physicochem. Eng. Asp.* **206**, 41–46 (2002).
45. Extrand, C. W. Contact angles and hysteresis on surfaces with chemically heterogeneous islands. *Langmuir* **19**, 3793–3796 (2003).
46. Gao, L. & McCarthy, T. J. How Wenzel and Cassie were wrong. *Langmuir* **23**, 3762–3765 (2007).
47. Tran, P. A. & Webster, T. J. Understanding the wetting properties of nanostructured selenium coatings: The role of nanostructured surface roughness and air-pocket formation. *Int. J. Nanomedicine* **8**, 2001–2009 (2013).

48. McHale, G. Cassie and Wenzel: Were they really so wrong? *Langmuir* **23**, 8200–8205 (2007).
49. Sun, Y. *et al.* The most stable state of a droplet on anisotropic patterns: Support for a missing link. *Surf. Innov.* **6**, 133–140 (2018).
50. Gaydos, J. & Neumann, A. W. The dependence of contact angles on drop size and line tension. *J. Colloid Interface Sci.* **120**, 76–86 (1987).
51. Oner, D. & McCarthy, T. J. Ultra-Hydrophobic Surfaces: Effects of Topography Length Scales on Wettability. *Langmuir* **16**, 7777–7782 (2000).
52. Bartell, F. E. & Shepard, J. W. Surface roughness as related to hysteresis of contact angles. I. The system paraffin-water-air. *J. Phys. Chem.* **57**, 211–215 (1953).
53. Erbil, H. Y. The debate on the dependence of apparent contact angles on drop contact area or three-phase contact line: A review. *Surf. Sci. Rep.* **69**, 325–365 (2014).
54. Marmur, A. & Bittoun, E. When wenzel and cassie are right: Reconciling local and global considerations. *Langmuir* **25**, 1277–1281 (2009).
55. Marmur, A. From hydrophilic to superhydrophobic: Theoretical conditions for making high-contact-angle surfaces from low-contact-angle materials. *Langmuir* **24**, 7573–7579 (2008).
56. Johnson, R. E. & Dettre, R. H. Contact Angle Hysteresis. III. Study of an Idealized Heterogeneous Surface. *J. Phys. Chem.* **68**, 1744–1750 (1964).
57. Li, D. Drop size dependence of contact angles and line tensions of solid-liquid systems. *Colloids Surfaces A Physicochem. Eng. Asp.* **116**, 1–23 (1996).
58. Chen, Y., He, B., Lee, J. & Patankar, N. A. Anisotropy in the wetting of rough surfaces. *J. Colloid Interface Sci.* **281**, 458–464 (2005).
59. Marmur, A. Contact-angle hysteresis on heterogeneous smooth surfaces: Theoretical comparison of the captive bubble and drop methods. *Colloids Surfaces A Physicochem. Eng. Asp.* **136**, 209–215 (1998).

60. Shahraz, A., Borhan, A. & Fichthorn, K. A. A theory for the morphological dependence of wetting on a physically patterned solid surface. *Langmuir* **28**, 14227–14237 (2012).
61. Lafuma, A. & Quéré, D. Superhydrophobic states. *Nat. Mater.* **2**, 457–60 (2003).
62. Bormashenko, E., Pogreb, R., Whyman, G., Bormashenko, Y. & Erlich, M. Vibration-induced Cassie-Wenzel wetting transition on rough surfaces. *Appl. Phys. Lett.* **90**, 51–53 (2007).
63. Boreyko, J. B. & Chen, C. H. Restoring superhydrophobicity of lotus leaves with vibration-induced dewetting. *Phys. Rev. Lett.* **103**, 1–4 (2009).
64. Law, K.-Y. & Zhao, H. *Surface Wetting. Langmuir* **27**, (Springer International Publishing, 2016).
65. Marmur, A. Solid-Surface Characterization by Wetting. *Annu. Rev. Mater. Res.* **39**, 473–489 (2009).
66. Kusumaatmaja, H., Vrancken, R. J., Bastiaansen, C. W. M. & Yeomans, J. M. Anisotropic drop morphologies on corrugated surfaces. *Langmuir* **24**, 7299–7308 (2008).
67. Brandon, S., Haimovich, N., Yeger, E. & Marmur, A. Partial wetting of chemically patterned surfaces: The effect of drop size. *J. Colloid Interface Sci.* **263**, 237–243 (2003).
68. Ruiz-Cabello, F. J. M., Rodríguez-Valverde, M. a. & Cabrerizo-Vílchez, M. A new method for evaluating the most-stable contact angle using mechanical vibration. *Soft Matter* **7**, 10457 (2011).
69. Gadelmawla, E. S., Koura, M. M., Maksoud, T. M. A., Elewa, I. M. & Soliman, H. H. Roughness parameters. *J. Mater. Process. Technol.* **123**, 133–145 (2002).
70. Marmur, A. & Krasovitski, B. Line tension on curved surfaces: Liquid drops on solid micro-and nanospheres. *Langmuir* **18**, 8919–8923 (2002).
71. Pompe, T., Fery, A. & Herminghaus, S. Measurement of contact line tension by analysis of the three-phase boundary with nanometer resolution. *J. Adhes. Sci. Technol.* **13**, 1155–1164 (1999).

72. Marmur, A. Line Tension and the Intrinsic Contact Angle in Solid-Liquid-Fluid Systems. *J. Colloid Interface Sci.* **186**, 462–6 (1997).
73. Gao, L. & McCarthy, T. J. An attempt to correct the faulty intuition perpetuated by the wenzel and cassie ‘laws’. *Langmuir* **25**, 7249–7255 (2009).
74. Park, J. *et al.* Direct and accurate measurement of size dependent wetting behaviors for sessile water droplets. *Sci. Rep.* **5**, 18150 (2015).
75. Amirfazli, A., Kwok, D. Y., Gaydos, J. & Neumann, A. W. Line Tension Measurements through Drop Size Dependence of Contact Angle. *J. Colloid Interface Sci.* **205**, 1–11 (1998).
76. Lin, F.Y.H; Li, D; Neumann, A. . Effect of Surface Roughness on the Dependence of Contact Angles on Drop Size. *J. Colloid Interface Sci.* **159**, 86–95 (1993).
77. Ponter, a. B. & Boyes, a. P. The Relation between Contact Angle and Drop Size for Water at its Boiling Point for a Pressure Range 50–760 Torr. *Can. J. Chem.* **50**, 2419–2422 (1972).
78. Boyes, A. P. & Ponter, A. B. The Influence of Condensate Drop Size on the Dropwise Filmwise Transition for Pure Vapors. *J. Chem. Eng. Japan* **7**, 314–316 (1974).
79. Good, R. J. & Koo, M. N. The effect of drop size on contact angle. *J. Colloid Interface Sci.* **71**, 283–292 (1979).
80. Wallace, J. A. & Schürch, S. Line tension of a sessile drop on a fluid-fluid interface modified by a phospholipid monolayer. *J. Colloid Interface Sci.* **124**, 452–461 (1988).
81. Yekta-Fard, M. & Ponter, A. B. The influences of vapor environment and temperature on the contact angle-drop size relationship. *J. Colloid Interface Sci.* **126**, 134–140 (1988).
82. Li, D. & Neumann, a. W. Determination of line tension from the drop size dependence of contact angles. *Colloids and Surfaces* **43**, 195–206 (1990).
83. Jacqueline, A. W. & Schürch, S. Line tension of sessile drops placed on a phospholipid monolayer at the water-fluorocarbon interface. *Colloids and Surfaces* **43**, 207–221 (1990).

84. Wolansky, G. & Marmur, A. The Actual Contact Angle on a Heterogeneous Rough Surface in Three Dimensions. *Langmuir* **14**, 5292–5297 (1998).
85. Koch, W., Dietrich, S. & Napiórkowski, M. Morphology and line tension of liquid films adsorbed on chemically structured substrates. *Phys. Rev. E* **51**, 3300–3317 (1995).
86. Aveyard, R. & Clint, J. H. Liquid Droplets And Solid Particles At Surfactant Solution Interfaces. *J. Chem. Soc. Trans.* **91**, 2681–2697 (1995).
87. Gibbs, J. W. *Scientific Papers*. (Dover Publications, 1961).
88. Boruvka, L. & Neumann, a. W. Generalization of the classical theory of capillarity. *J. Chem. Phys.* **66**, 5464 (1977).
89. Letellier, P., Mayaffre, A. & Turmine, M. Drop size effect on contact angle explained by nonextensive thermodynamics . Young ’ s equation revisited. **314**, 604–614 (2007).
90. Rusanov, a. I. Thermodynamics of solid surfaces. *Surf. Sci. Rep.* **23**, 173–247 (1996).
91. Babak, V. G. Generalised line tension theory revisited. *Colloids Surfaces A Physicochem. Eng. Asp.* **156**, 423–448 (1999).
92. Marmur, A. Thermodynamic aspects of contact angle hysteresis. *Adv. Colloid Interface Sci.* **50**, 121–141 (1994).
93. Pompe, T. & Herminghaus, S. Three-Phase Contact Line Energetics from Nanoscale Liquid Surface Topographies. *Phys. Rev. Lett.* **85**, 1930–1933 (2000).
94. Drelich, J., Wilbur, J. L., Miller, J. D. & Whitesides, G. M. Contact Angles for Liquid Drops at a Model Heterogeneous Surface Consisting of Alternating and Parallel Hydrophobic/Hydrophilic Strips. *Langmuir* **12**, 1913–1922 (1996).
95. Marmur, A. Equilibrium and Spreading of Liquids on Solid Surfaces. *Adv. Colloid Interface Sci.* **19**, 75–102 (1983).
96. Marmur, A. Contact Angle and Thin-Film Equilibrium. **148**, 541–550 (1992).
97. Marmur, A. Contact Angle Equilibrium: The Intrinsic Contact Angle. *J. Adhes. Sci.*

- Technol.* **6**, 689–701 (1992).
98. Guo, Z., Liu, W. & Su, B. L. Superhydrophobic surfaces: From natural to biomimetic to functional. *J. Colloid Interface Sci.* **353**, 335–355 (2011).
 99. Park, C. I., Jeong, H. E., Lee, S. H., Cho, H. S. & Suh, K. Y. Wetting transition and optimal design for microstructured surfaces with hydrophobic and hydrophilic materials. *J. Colloid Interface Sci.* **336**, 298–303 (2009).
 100. Blondiaux, N., Scolan, E., Popa, A. M., Gavillet, J. & Pugin, R. Fabrication of superhydrophobic surfaces with controlled topography and chemistry. *Appl. Surf. Sci.* **256**, 46–53 (2009).
 101. Bell, M. S., Shahraz, A., Fichthorn, K. A. & Borhan, A. Effects of Hierarchical Surface Roughness on Droplet Contact Angle. *Langmuir* **31**, 6752–6762 (2015).
 102. Nishino, T., Meguro, M., Nakamae, K., Matsushita, M. & Ueda, Y. The Lowest Surface Free Energy Based on $-CF_3$ Alignment. *Langmuir* **15**, 4321–4323 (1999).
 103. Celia, E., Darmanin, T., Taffin de Givenchy, E., Amigoni, S. & Guittard, F. Recent advances in designing superhydrophobic surfaces. *J. Colloid Interface Sci.* **402**, 1–18 (2013).
 104. Li, W., Cui, X. S. & Fang, G. P. Optimal geometrical design for superhydrophobic surfaces: Effects of a trapezoid microtexture. *Langmuir* **26**, 3194–3202 (2010).
 105. Herminghaus, S. Roughness-induced non-wetting. *Europhys. Lett.* **52**, 165–170 (2000).
 106. Meng, L.-Y. & Park, S.-J. Superhydrophobic carbon-based materials: a review of synthesis, structure, and applications. *Carbon Lett.* **15**, 89–104 (2014).
 107. Lee, Y., Park, S. H., Kim, K. B. & Lee, J. K. Fabrication of hierarchical structures on a polymer surface to mimic natural superhydrophobic surfaces. *Adv. Mater.* **19**, 2330–2335 (2007).
 108. Bittoun, E. & Marmur, A. The role of multiscale roughness in the lotus effect: Is it essential for super-hydrophobicity? *Langmuir* **28**, 13933–13942 (2012).

109. Yu, Y., Zhao, Z. H. & Zheng, Q. S. Mechanical and superhydrophobic stabilities of two-scale surfacial structure of lotus leaves. *Langmuir* **23**, 8212–8216 (2007).
110. Extrand, C. W. Repellency of the lotus leaf: Resistance to water intrusion under hydrostatic pressure. *Langmuir* **27**, 6920–6925 (2011).
111. Darmanin, T., De Givenchy, E. T., Amigoni, S. & Guittard, F. Superhydrophobic surfaces by electrochemical processes. *Adv. Mater.* **25**, 1378–1394 (2013).
112. Li, X.-M., Reinhoudt, D. & Crego-Calama, M. What do we need for a superhydrophobic surface? A review on the recent progress in the preparation of superhydrophobic surfaces. *Chem. Soc. Rev.* **36**, 1350 (2007).
113. Isao Matsui, Mingjun Li & Naoki Omura. Fabricating Bulk Nanocrystalline Ni–W–B Alloys by Electrodeposition. *Mater. Trans.* **58**, 1038–1041 (2017).
114. Babakhani, B. & Ivey, D. G. Effect of electrodeposition conditions on the electrochemical capacitive behavior of synthesized manganese oxide electrodes. *J. Power Sources* **196**, 10762–10774 (2011).
115. Zhao, J. *et al.* Phosphate tuned copper electrodeposition and promoted formic acid selectivity for carbon dioxide reduction. *J. Mater. Chem. A* **5**, 11905–11916 (2017).
116. Dong, H., Wang, Y., Tao, F. & Wang, L. Electrochemical fabrication of shape-controlled copper hierarchical structures assisted by surfactants. *J. Nanomater.* **2012**, (2012).
117. Radi, A., Pradhan, D., Sohn, Y. & Leung, K. T. Nanoscale Shape and Size Control of Cubic, Cuboctahedral, and Octahedral Cu–Cu₂O Core–Shell Nanoparticles on Si(100) by One-Step, Templateless, Capping-Agent-Free Electrodeposition. *ACS Nano* **4**, 1553–1560 (2010).
118. Zhou, W. J., Zhao, D. D., Xu, M. W., Xu, C. L. & Li, H. L. Effects of the electrodeposition potential and temperature on the electrochemical capacitance behavior of ordered mesoporous cobalt hydroxide films. *Electrochim. Acta* **53**, 7210–7219 (2008).
119. Bakthavatsalam, R. *et al.* Solution chemistry-based nano-structuring of copper dendrites

- for efficient use in catalysis and superhydrophobic surfaces. *RSC Adv.* **6**, 8416–8430 (2016).
120. Kwon, Y. B. *et al.* X-ray-induced changes in wettability. *Langmuir* **25**, 1927–1929 (2009).
 121. Feng, X. *et al.* Reversible super-hydrophobicity to super-hydrophilicity transition of aligned ZnO nanorod films. *J. Am. Chem. Soc.* **126**, 62–63 (2004).
 122. Pinchasik, B.-E., Wang, H., Möhwald, H. & Asanuma, H. Fully Reversible Transition between Cassie and Wenzel States via Acoustic Waves. *Adv. Mater. Interfaces* **3**, 1600722 (2016).
 123. Lee, S. G. *et al.* Switchable transparency and wetting of elastomeric smart windows. *Adv. Mater.* **22**, 5013–5017 (2010).
 124. Robinson, L., Hentzell, A., Robinson, N. D., Isaksson, J. & Berggren, M. Electrochemical wettability switches gate aqueous liquids in microfluidic systems. *Lab Chip* **6**, 1277 (2006).
 125. Zang, D. *et al.* Corrosion-Resistant Superhydrophobic Coatings on Mg Alloy Surfaces Inspired by Lotus Seedpod. *Adv. Funct. Mater.* **27**, 1–7 (2017).
 126. Liu, Y. *et al.* Bioinspired, Stimuli-Responsive, Multifunctional Superhydrophobic Surface with Directional Wetting, Adhesion, and Transport of Water. *Adv. Funct. Mater.* **25**, 5047–5056 (2015).
 127. Wu, J., Zhang, L., Wang, Y. & Wang, P. Efficient and Anisotropic Fog Harvesting on a Hybrid and Directional Surface. *Adv. Mater. Interfaces* **4**, 1600801 (2017).
 128. Yu, X., Wang, Z., Jiang, Y., Shi, F. & Zhang, X. Reversible pH-responsive surface: From superhydrophobicity to superhydrophilicity. *Adv. Mater.* **17**, 1289–1293 (2005).
 129. Yan, X., Li, J. & Yi, L. Fabrication of pH-responsive hydrophilic/hydrophobic Janus cotton fabric via plasma-induced graft polymerization. *Mater. Lett.* **208**, 46–49 (2017).
 130. Wang, N., Zhao, Y. & Jiang, L. Low-cost, thermoresponsive wettability of surfaces: Poly(N- isopropylacrylamide)/polystyrene composite films prepared by electrospinning.

- Macromol. Rapid Commun.* **29**, 485–489 (2008).
131. Zhao, T., Nie, F.-Q. & Jiang, L. Precise control of wettability from LCST tunable surface. *J. Mater. Chem.* **20**, 2176 (2010).
 132. Zhu, W., Feng, X., Feng, L. & Jiang, L. UV-Manipulated wettability between superhydrophobicity and superhydrophilicity on a transparent and conductive SnO₂ nanorod film. *Chem. Commun.* **0**, 2753–2755 (2006).
 133. Wang, R. *et al.* Light-induced amphiphilic surfaces. *Nature* **388**, 431–432 (1997).
 134. Chang, F. M., Sheng, Y. J., Chen, H. & Tsao, H. K. From superhydrophobic to superhydrophilic surfaces tuned by surfactant solutions. *Appl. Phys. Lett.* **91**, 1–4 (2007).
 135. Motornov, M. *et al.* Reversible tuning of wetting behavior of polymer surface with responsive polymer brushes. *Langmuir* **19**, 8077–8085 (2003).
 136. Krupenkin, T. N., Taylor, J. A., Schneider, T. M. & Yang, S. From rolling ball to complete wetting: The dynamic tuning of liquids on nanostructured surfaces. *Langmuir* **20**, 3824–3827 (2004).
 137. Krupenkin, T. N. *et al.* Reversible wetting-dewetting transitions on electrically tunable superhydrophobic nanostructured surfaces. *Langmuir* **23**, 9128–9133 (2007).
 138. Parihar, V., Bandyopadhyay, S., Das, S. & Dasgupta, S. Anisotropic Electrowetting on Wrinkled Surfaces: Enhanced Wetting and Dependency on Initial Wetting State. *Langmuir* **34**, 1844–1854 (2018).
 139. Chen, T. H., Chuang, Y. J., Chieng, C. C. & Tseng, F. G. A wettability switchable surface by microscale surface morphology change. *J. Micromechanics Microengineering* **17**, 489–495 (2007).
 140. Park, J. K., Yang, Z. & Kim, S. Black Silicon/Elastomer Composite Surface with Switchable Wettability and Adhesion between Lotus and Rose Petal Effects by Mechanical Strain. *ACS Appl. Mater. Interfaces* **9**, 33333–33340 (2017).
 141. Wong, W. S. Y. *et al.* Strain Engineering of Wave-like Nanofibers for Dynamically

- Switchable Adhesive/Repulsive Surfaces. *Adv. Funct. Mater.* **26**, 399–407 (2016).
142. Goel, P., Kumar, S., Sarkar, J. & Singh, J. P. Mechanical strain induced tunable anisotropic wetting on buckled PDMS silver nanorods arrays. *ACS Appl. Mater. Interfaces* **7**, 8419–8426 (2015).
 143. Zhang, J., Li, J. & Han, Y. Superhydrophobic PTFE surfaces by extension. *Macromol. Rapid Commun.* **25**, 1105–1108 (2004).
 144. Kwon, G. *et al.* On-demand separation of oil-water mixtures. *Adv. Mater.* **24**, 3666–3671 (2012).
 145. Guo, F. & Guo, Z. Inspired smart materials with external stimuli responsive wettability: a review. *RSC Adv.* **6**, 36623–36641 (2016).
 146. Hao, C. *et al.* Electrowetting on liquid-infused film (EWOLF): Complete reversibility and controlled droplet oscillation suppression for fast optical imaging. *Sci. Rep.* **4**, 1–7 (2014).
 147. Xin, B. & Hao, J. Reversibly switchable wettability. *Chem. Soc. Rev.* **39**, 769–782 (2010).
 148. Lahann, J. *et al.* A reversibly switching surface. *Science (80-.)*. **299**, 371–374 (2003).
 149. Isaksson, J., Tengstedt, C., Fahlman, M., Robinson, N. & Berggren, M. A Solid-State Organic Electronic Wettability Switch. *Adv. Mater.* **16**, 316–320 (2004).
 150. Zheng, X., Guo, Z., Tian, D., Zhang, X. & Jiang, L. Electric Field Induced Switchable Wettability to Water on the Polyaniline Membrane and Oil/Water Separation. *Adv. Mater. Interfaces* **3**, 1–6 (2016).
 151. Zhang, G., Walker, M. & Unwin, P. R. Low-Voltage Voltammetric Electrowetting of Graphite Surfaces by Ion Intercalation/Deintercalation. *Langmuir* **32**, 7476–7484 (2016).
 152. Zou, Y., Walton, A. S., Kinloch, I. A. & Dryfe, R. A. W. Investigation of the Differential Capacitance of Highly Ordered Pyrolytic Graphite as a Model Material of Graphene. *Langmuir* **32**, 11448–11455 (2016).
 153. Wang, Z. *et al.* Polarity-dependent electrochemically controlled transport of water through

- carbon nanotube membranes. *Nano Lett.* **7**, 697–702 (2007).
154. Casado-Montenegro, J. *et al.* Electrochemical and chemical tuning of the surface wettability of tetrathiafulvalene self-assembled monolayers. *Chem. Commun.* **49**, 8084 (2013).
 155. Lin, X. *et al.* Electricity-induced switchable wettability and controllable water permeation based on 3D copper foam. *Chem. Commun.* **51**, 16237–16240 (2015).
 156. Kornyshev, A. A. *et al.* Ultra-Low-Voltage Electrowetting. *J. Phys. Chem. C* **114**, 14885–14890 (2010).
 157. Liu, Y., Liang, Y. E., Sheng, Y. J. & Tsao, H. K. Ultralow voltage irreversible electrowetting dynamics of an aqueous drop on a stainless steel surface. *Langmuir* **31**, 3840–3846 (2015).
 158. Lomax, D. J. *et al.* Ultra-low voltage electrowetting using graphite surfaces. *Soft Matter* **12**, 8798–8804 (2016).
 159. Chang, F. M., Cheng, S. L., Hong, S. J., Sheng, Y. J. & Tsao, H. K. Superhydrophilicity to superhydrophobicity transition of CuO nanowire films. *Appl. Phys. Lett.* **96**, 2008–2011 (2010).
 160. Zhang, J., Gu, C., Tong, Y., Yan, W. & Tu, J. A Smart Superhydrophobic Coating on AZ31B Magnesium Alloy with Self-Healing Effect. *Adv. Mater. Interfaces* **3**, 1500694 (2016).
 161. Laurenti, M. *et al.* How Micropatterning and Surface Functionalization Affect the Wetting Behavior of ZnO Nanostructured Surfaces. *Adv. Mater. Interfaces* **3**, 1600110 (2016).
 162. Chen, X., Weibel, J. A. & Garimella, S. V. Exploiting Microscale Roughness on Hierarchical Superhydrophobic Copper Surfaces for Enhanced Dropwise Condensation. *Adv. Mater. Interfaces* **2**, 1400480 (2015).
 163. Wang, S. *et al.* Manipulation of surface wettability between superhydrophobicity and superhydrophilicity on copper films. *ChemPhysChem* **6**, 1475–1478 (2005).

164. Cheng, Z. *et al.* Recycled Superwetting Nanostructured Copper Mesh Film: Toward Bidirectional Separation of Emulsified Oil/Water Mixtures. *Adv. Mater. Interfaces* **3**, 1–10 (2016).
165. Li, H. *et al.* In Situ Growth of Densely Packed Single-Crystal Copper Nanocone Structure Films with Condensate Microdrop Self-Removal Function on Copper Surfaces. *Adv. Mater. Interfaces* **3**, 1600362 (2016).
166. Sasmal, A. K. *et al.* Fabrication of Superhydrophobic Copper Surface on Various Substrates for Roll-off, Self-Cleaning, and Water/Oil Separation. *ACS Appl. Mater. Interfaces* **6**, 22034–22043 (2014).
167. Qiu, R. *et al.* Preparation of Dendritic Copper Nanostructures and Their Characterization for Electroreduction. *J. Phys. Chem. C* **113**, 15891–15896 (2009).
168. Dubal, D. P., Gund, G. S., Lokhande, C. D. & Holze, R. CuO cauliflowers for supercapacitor application: Novel potentiodynamic deposition. *Mater. Res. Bull.* **48**, 923–928 (2013).
169. Paracchino, A., Laporte, V., Sivula, K., Grätzel, M. & Thimsen, E. Highly active oxide photocathode for photoelectrochemical water reduction. *Nat. Mater.* **10**, 456–461 (2011).
170. Lee, S. M. *et al.* Facile route toward mechanically stable superhydrophobic copper using oxidation-reduction induced morphology changes. *J. Phys. Chem. C* **116**, 2781–2790 (2012).
171. Tu, S. H. *et al.* Growing hydrophobicity on a smooth copper oxide thin film at room temperature and reversible wettability transition. *Appl. Surf. Sci.* **316**, 88–92 (2014).
172. Haghdoost, a & Pitchumani, R. Fabricating superhydrophobic surfaces via a two-step electrodeposition technique. *Langmuir* **30**, 4183–91 (2014).
173. Pei, M. De *et al.* The fabrication of superhydrophobic copper films by a low-pressure-oxidation method. *Appl. Surf. Sci.* **256**, 5824–5827 (2010).
174. Sun, T. *et al.* Reversible Switching between Superhydrophilicity and

- Superhydrophobicity. *Angew. Chemie - Int. Ed.* **43**, 357–360 (2004).
175. Zhang, J., Lu, X., Huang, W. & Han, Y. Reversible superhydrophobicity to superhydrophilicity transition by extending and unloading an elastic polyamide film. *Macromol. Rapid Commun.* **26**, 477–480 (2005).
 176. Schmidt-Stein, F. *et al.* Electrochemical wettability control on conductive TiO₂nanotube surfaces modified with a ferrocene redox system. *Electrochem. commun.* **11**, 2000–2003 (2009).
 177. Chaudhary, A. & Barshilia, H. C. Nanometric multiscale rough CuO/Cu(OH)₂ superhydrophobic surfaces prepared by a facile one-step solution-immersion process: Transition to superhydrophilicity with oxygen plasma treatment. *J. Phys. Chem. C* **115**, 18213–18220 (2011).
 178. Wang, G. & Zhang, T. Y. Easy route to the wettability cycling of copper surface between superhydrophobicity and superhydrophilicity. *ACS Appl. Mater. Interfaces* **4**, 273–279 (2012).
 179. Hua, Z., Yang, J., Wang, T., Liu, G. & Zhang, G. Transparent surface with reversibly switchable wettability between superhydrophobicity and superhydrophilicity. *Langmuir* **29**, 10307–10312 (2013).
 180. Zheng, J. Y., Bao, S. H., Guo, Y. & Jin, P. Natural hydrophobicity and reversible wettability conversion of flat anatase TiO₂ thin film. *ACS Appl. Mater. Interfaces* **6**, 1351–1355 (2014).
 181. Che, H. *et al.* CO₂ -Responsive Nanofibrous Membranes with Switchable Oil/Water Wettability. *Angew. Chemie Int. Ed.* **54**, 8934–8938 (2015).
 182. Liu, Y. *et al.* Reversibly switchable wettability on aluminum alloy substrate corresponding to different pH droplet and its corrosion resistance. *Chem. Eng. J.* **303**, 565–574 (2016).
 183. Yadav, K., Mehta, B. R., Bhattacharya, S. & Singh, J. P. A fast and effective approach for reversible wetting-dewetting transitions on ZnO nanowires. *Sci. Rep.* **6**, 35073 (2016).

184. Ranganath, A. S., Ganesh, V. A., Sopiha, K., Sahay, R. & Baji, A. Thermoresponsive electrospun membrane with enhanced wettability. *RSC Adv.* **7**, 19982–19989 (2017).
185. Yang, H., Hu, X., Su, C., Liu, Y. & Chen, R. Reversibly photo-switchable wettability of stearic acid monolayer modified bismuth-based micro-/nanomaterials. *Phys. Chem. Chem. Phys.* **19**, 31666–31674 (2017).
186. Yang, W., Li, J., Zhou, P., Zhu, L. & Tang, H. Superhydrophobic copper coating: Switchable wettability, on-demand oil-water separation, and antifouling. *Chem. Eng. J.* **327**, 849–854 (2017).
187. Zhou, C. *et al.* Opposite Superwetting Nickel Meshes for On-Demand and Continuous Oil/Water Separation. *Ind. Eng. Chem. Res.* **57**, 1059–1070 (2018).
188. Zhang, G. *et al.* Electrical potential induced switchable wettability of super-aligned carbon nanotube films. *Appl. Surf. Sci.* **427**, 628–635 (2018).
189. Velayi, E. & Norouzbeigi, R. Annealing temperature dependent reversible wettability switching of micro/nano structured ZnO superhydrophobic surfaces. *Appl. Surf. Sci.* **441**, 156–164 (2018).
190. Zahiri, B., Sow, P. K., Kung, C. H. & Mérida, W. Active Control over the Wettability from Superhydrophobic to Superhydrophilic by Electrochemically Altering the Oxidation State in a Low Voltage Range. *Adv. Mater. Interfaces* **4**, (2017).
191. Haow Kung, C., Zahiri, B., Kumar Sow, P. & Mérida, W. On-demand oil-water separation via low-voltage wettability switching of core-shell structures on copper substrates. *Appl. Surf. Sci.* **444**, 15–27 (2018).
192. Yildirim Erbil, H. & Elif Cansoy, C. Range of applicability of the wenzel and cassie-baxter equations for superhydrophobic surfaces. *Langmuir* **25**, 14135–14145 (2009).
193. Cansoy, C. E. The effect of drop size on contact angle measurements of superhydrophobic surfaces. *RSC Adv.* **4**, 1197–1203 (2014).
194. Antonini, C., Villa, F. & Marengo, M. Oblique impacts of water drops onto hydrophobic

- and superhydrophobic surfaces: Outcomes, timing, and rebound maps. *Exp. Fluids* **55**, (2014).
195. Mishra, H. *et al.* Time-Dependent Wetting Behavior of PDMS Surfaces with Bioinspired, Hierarchical Structures. *ACS Appl. Mater. Interfaces* **8**, 8168–8174 (2016).
 196. Martines, E. *et al.* Superhydrophobicity and superhydrophilicity of regular nanopatterns. *Nano Lett.* **5**, 2097–2103 (2005).
 197. Zhenyu, S., Zhanqiang, L., Hao, S. & Xianzhi, Z. Prediction of contact angle for hydrophobic surface fabricated with micro-machining based on minimum Gibbs free energy. *Appl. Surf. Sci.* **364**, 597–603 (2016).
 198. Papadopoulos, P., Mammen, L., Deng, X., Vollmer, D. & Butt, H. How superhydrophobicity breaks down. *Proc. Natl. Acad. Sci. U. S. A.* **110**, 3254–3258 (2013).
 199. Antonini, C. *et al.* Unraveling wetting transition through surface textures with X-rays: Liquid meniscus penetration phenomena. *Sci. Rep.* **4**, 1–6 (2014).
 200. Hejazi, V., Moghadam, A. D., Rohatgi, P. & Nosonovsky, M. Beyond Wenzel and Cassie-Baxter: Second-order effects on the wetting of rough surfaces. *Langmuir* **30**, 9423–9429 (2014).
 201. Daikhin, L., Kornyshev, a. & Urbakh, M. Double-layer capacitance on a rough metal surface. *Phys. Rev. E* **53**, 6192–6199 (1996).
 202. Xu, J. *et al.* Preparing two-dimensional microporous carbon from Pistachio nutshell with high areal capacitance as supercapacitor materials. *Sci. Rep.* **4**, 5545 (2014).
 203. Liang, Y., Wu, D. & Fu, R. Preparation and electrochemical performance of novel ordered mesoporous carbon with an interconnected channel structure. *Langmuir* **25**, 7783–7785 (2009).
 204. Yang, D. Q. & Sacher, E. Platinum nanoparticle interaction with chemically modified highly oriented pyrolytic graphite surfaces. *Chem. Mater.* **18**, 1811–1816 (2006).
 205. Ko, T. J. *et al.* Water condensation behavior on the surface of a network of

- superhydrophobic carbon fibers with high-aspect-ratio nanostructures. *Carbon N. Y.* **50**, 5085–5092 (2012).
206. Plank, N. O. V, Jiang, L. & Cheung, R. Fluorination of carbon nanotubes in CF₄ plasma. *Appl. Phys. Lett.* **83**, 2426–2428 (2003).
207. Sow, P. K., Prass, S. & Mérida, W. An Alternative Approach to Evaluate the Wettability of Carbon Fiber Substrates. *ACS Appl. Mater. Interfaces* **7**, 22029–22035 (2015).
208. Stalder, A. F., Kulik, G., Sage, D., Barbieri, L. & Hoffmann, P. A snake-based approach to accurate determination of both contact points and contact angles. *Colloids Surfaces A Physicochem. Eng. Asp.* **286**, 92–103 (2006).
209. Dutcher, C. S., Wexler, A. S. & Clegg, S. L. Surface tensions of inorganic multicomponent aqueous electrolyte solutions and melts. *J. Phys. Chem. A* **114**, 12216–12230 (2010).
210. He, B., Lee, J. & Patankar, N. A. Contact angle hysteresis on rough hydrophobic surfaces. *Colloids Surfaces A Physicochem. Eng. Asp.* **248**, 101–104 (2004).
211. Lam, C. N. C. *et al.* Dynamic Cycling Contact Angle Measurements: Study of Advancing and Receding Contact Angles. *J. Colloid Interface Sci.* **243**, 208–218 (2001).
212. Cho, K.-H. & Chen, L.-J. Fabrication of sticky and slippery superhydrophobic surfaces via spin-coating silica nanoparticles onto flat/patterned substrates. *Nanotechnology* **22**, 445706 (2011).
213. Chuang, Y.-C., Chu, C.-K., Lin, S.-Y. & Chen, L.-J. Evaporation of water droplets on soft patterned surfaces. *Soft Matter* **10**, 3394–403 (2014).
214. Law, K. Y. & Zhao, H. *Surface wetting: Characterization, contact angle, and fundamentals*. *Surface Wetting: Characterization, Contact Angle, and Fundamentals* (2015). doi:10.1007/978-3-319-25214-8
215. Spori, D. M., Drobek, T., Zürcher, S. & Spencer, N. D. Cassie-state wetting investigated by means of a hole-to-pillar density gradient. *Langmuir* **26**, 9465–9473 (2010).

216. Yeh, K.-Y., Chen, L.-J. & Chang, J.-Y. Contact Angle Hysteresis on Regular Pillar-like Hydrophobic Surfaces. *Langmuir* **24**, 245–251 (2008).
217. Erbil, H. Y., McHale, G., Rowan, S. M. & Newton, M. I. Determination of the Receding Contact Angle of Sessile Drops on Polymer Surfaces by Evaporation. *Langmuir* **15**, 7378–7385 (1999).
218. Tan, X. H. *et al.* Titanium oxynitride interlayer to influence oxygen reduction reaction activity and corrosion stability of Pt and Pt-Ni alloy. *ChemSusChem* **8**, 361–376 (2015).
219. Farbod, B. *et al.* Array geometry dictates electrochemical performance of Ge nanowire lithium ion battery anodes. *J. Mater. Chem. A* **2**, 16770–16785 (2014).
220. Wang, C. F. *et al.* Fabrication of biomimetic super-amphiphobic surfaces through plasma modification of benzoxazine films. *Macromol. Rapid Commun.* **27**, 333–337 (2006).
221. Yan, J. *et al.* Electrochemical properties of graphene nanosheet/carbon black composites as electrodes for supercapacitors. *Carbon N. Y.* **48**, 1731–1737 (2010).
222. Frackowiak, E. & Béguin, F. Carbon materials for the electrochemical storage of energy in capacitors. *Carbon N. Y.* **39**, 937–950 (2001).
223. Schoch, R. B., van Lintel, H. & Renaud, P. Effect of the surface charge on ion transport through nanoslits. *Phys. Fluids* **17**, 2–7 (2005).
224. Wang, Y. *et al.* Evaluation of macroscale wetting equations on a microrough surface. *Langmuir* **31**, 2342–50 (2015).
225. Cwickel, D., Paz, Y. & Marmur, A. Contact angle measurement on rough surfaces: the missing link. *Surf. Innov.* **5**, 190–193 (2017).
226. Chen, W. *et al.* Ultrahydrophobic and Ultralyophobic Surfaces : Some Comments and Examples. **15**, 3395–3399 (1999).
227. Gao, L. & McCarthy, T. J. Contact angle hysteresis explained. *Langmuir* **22**, 6234–6237 (2006).

228. Duursma, G. R., Sefiane, K. & David, S. Advancing and receding contact lines on patterned structured surfaces. *Chem. Eng. Res. Des.* **88**, 737–743 (2010).
229. Bhushan, B., Nosonovsky, M. & Jung, Y. C. Towards optimization of patterned superhydrophobic surfaces. *J. R. Soc. Interface* **4**, 643–648 (2007).
230. Yeh, K. Y., Chen, L. J. & Chang, J. Y. Contact angle hysteresis on regular pillar-like hydrophobic surfaces. *Langmuir* **24**, 245–251 (2008).
231. Raj, R., Adera, S., Enright, R. & Wang, E. N. High-resolution liquid patterns via three-dimensional droplet shape control. *Nat. Commun.* **5**, 4975 (2014).
232. Johnson, R. E. & Dettre, R. H. Contact Angle Hysteresis I. Study of an Idealized Rough Surface. *Adv. Chem.* **43**, 112–135 (1964).
233. Weisensee, P. B., Neelakantan, N. K., Suslick, K. S., Jacobi, A. M. & King, W. P. Impact of air and water vapor environments on the hydrophobicity of surfaces. *J. Colloid Interface Sci.* **453**, 177–185 (2015).
234. Quéré, D. Wetting and Roughness. *Annu. Rev. Mater. Res.* **38**, 71–99 (2008).
235. Angles, D. C. A Note on the Measurement of Dynamic Contact Angles. *J. Colloid Interface Sci.* **51**, 532–534 (1975).
236. Sun, K. *et al.* Nanostructured Surface with Tunable Contact Angle Hysteresis for Constructing in Vitro Tumor Model. *J. Nanomater.* **2016**, 1–6 (2016).
237. Darmanin, T. & Guittard, F. Recent advances in the potential applications of bioinspired superhydrophobic materials. *J. Mater. Chem. A* **2**, 16319–16359 (2014).
238. Erbil, H. Y., McHale, G. & Newton, M. I. Drop evaporation on solid surfaces: Constant contact angle mode. *Langmuir* **18**, 2636–2641 (2002).
239. McHale, G., Aqil, S., Shirtcliffe, N. J., Newton, M. I. & Erbil, H. Y. Analysis of droplet evaporation on a superhydrophobic surface. *Langmuir* **21**, 11053–11060 (2005).
240. Darmanin, T. *et al.* Recent advances in the potential applications of bioinspired

- superhydrophobic materials. *J. Mater. Chem. A* **2**, 16319–16359 (2014).
241. Bushueva, E. G. *et al.* Double layer supercapacitor properties of onion-like carbon materials. *Phys. Status Solidi Basic Res.* **245**, 2296–2299 (2008).
242. Wang, S., Hsia, B., Carraro, C. & Maboudian, R. High-performance all solid-state micro-supercapacitor based on patterned photoresist-derived porous carbon electrodes and an ionogel electrolyte. *J. Mater. Chem. A* **2**, 7997–8002 (2014).
243. Noked, M., Avraham, E., Soffer, A. & Aurbach, D. Assessing the concentration effect on hydration radii in aqueous solutions by electroadsorption on a carbon molecular sieve electrode. *J. Phys. Chem. C* **114**, 13354–13361 (2010).
244. Bohinc, K., Kralj-Iglič, V. & Iglič, A. Thickness of electrical double layer. Effect of ion size. *Electrochim. Acta* **46**, 3033–3040 (2001).
245. Yang, K. L., Yiacomini, S. & Tsouris, C. Electrosorption capacitance of nanostructured carbon aerogel obtained by cyclic voltammetry. *J. Electroanal. Chem.* **540**, 159–167 (2003).
246. Al-zubaidi, A., Inoue, T., Matsushita, T., Ishii, Y. & Kawasaki, S. Ion adsorption on the inner surface of single-walled carbon nanotubes used as electrodes for electric double-layer capacitors. *Phys. Chem. Chem. Phys.* **14**, 16055 (2012).
247. Gujar, T. P., Shinde, V. R., Lokhande, C. D. & Han, S. H. Electrosynthesis of Bi₂O₃ thin films and their use in electrochemical supercapacitors. *J. Power Sources* **161**, 1479–1485 (2006).
248. Tsay, K. C., Zhang, L. & Zhang, J. Effects of electrode layer composition/thickness and electrolyte concentration on both specific capacitance and energy density of supercapacitor. *Electrochim. Acta* **60**, 428–436 (2012).
249. Nadakatti, S., Tendulkar, M. & Kadam, M. Use of mesoporous conductive carbon black to enhance performance of activated carbon electrodes in capacitive deionization technology. *Desalination* **268**, 182–188 (2011).

250. Ying, T.-Y., Yang, K.-L., Yiacoumi, S. & Tsouris, C. Electrosorption of ions from aqueous solutions by nanostructured carbon aerogel. *J. Colloid Interface Sci.* **250**, 18–27 (2002).
251. Hatsuki, R., Yujiro, F. & Yamamoto, T. Direct measurement of electric double layer in a nanochannel by electrical impedance spectroscopy. *Microfluid. Nanofluidics* **14**, 983–988 (2012).
252. Brown, M. A., Goel, A. & Abbas, Z. Effect of Electrolyte Concentration on the Stern Layer Thickness at a Charged Interface. *Angew. Chemie - Int. Ed.* **55**, 3790–3794 (2016).
253. Daikhin, L. I., Kornyshev, A. A. & Urbakh, M. Double-layer capacitance on a rough metal surface. *Phys. Rev. E* **53**, 6192–6199 (1996).
254. Borghi, F., Vyas, V., Podestà, A. & Milani, P. Nanoscale Roughness and Morphology Affect the IsoElectric Point of Titania Surfaces. *PLoS One* **8**, 1–14 (2013).
255. Young, K. F. & Frederikse, H. P. R. Compilation of the Static Dielectric Constant of Inorganic Solids. *J. Phys. Chem. Ref. Data* **2**, 313–410 (1973).
256. Kim, T. & Yoon, J. Relationship between capacitance of activated carbon composite electrodes measured at a low electrolyte concentration and their desalination performance in capacitive deionization. *J. Electroanal. Chem.* **704**, 169–174 (2013).
257. Yang, C., Tartaglino, U. & Persson, B. N. J. Nanodroplets on rough hydrophilic and hydrophobic surfaces. *Eur. Phys. J. E* **25**, 139–152 (2008).
258. Hu, L., Huang, Y., Chen, W., Fu, X. & Xie, H. Pinning Effects of Wettability Contrast on Pendant Drops on Chemically Patterned Surfaces. *Langmuir* **32**, 11780–11788 (2016).
259. Kashaninejad, N., Chan, W. K. & Nguyen, N. T. Eccentricity effect of micropatterned surface on contact angle. *Langmuir* **28**, 4793–4799 (2012).
260. Dorrer, C.; R uhe, J. Contact Line Shape on Ultrahydrophobic Post Surfaces. *Langmuir* **23**, 3179–3183 (2007).
261. Gao, L. & McCarthy, T. J. Wetting 101?? *Langmuir* **25**, 14105–14115 (2009).

262. Pease, D. C. The Significance of the Contact Angle in Relation to the Solid Surface. *J. Phys. Chem.* **49**, 107–110 (1945).
263. Pakdel, A., Bando, Y. & Golberg, D. Plasma-assisted interface engineering of boron nitride nanostructure films. *ACS Nano* **8**, 10631–9 (2014).
264. Li, Y., Wu, H. & Wang, F. Effect of a Single Nanoparticle on the Contact Line Motion. *Langmuir* **32**, 12676–12685 (2016).
265. Yeh, S. Y. & Lan, C. W. Adaptive Phase-Field Modeling of Anisotropic Wetting with Line Tension at the Triple Junction. *Langmuir* **31**, 9348–9355 (2015).
266. Zhang, B., Wang, J., Liu, Z. & Zhang, X. Beyond Cassie equation: Local structure of heterogeneous surfaces determines the contact angles of microdroplets. *Sci. Rep.* **4**, 1–7 (2014).
267. Cengiz, U. & Elif Cansoy, C. Applicability of Cassie–Baxter equation for superhydrophobic fluoropolymer–silica composite films. *Appl. Surf. Sci.* **335**, 99–106 (2015).
268. Ambrosia, M. S., Ha, M. Y. & Balachandar, S. The effect of pillar surface fraction and pillar height on contact angles using molecular dynamics. *Appl. Surf. Sci.* **282**, 211–216 (2013).
269. Pashos, G., Kokkoris, G. & Boudouvis, A. G. Minimum Energy Paths of Wetting Transitions on Grooved Surfaces. *Langmuir* **31**, 3059–3068 (2015).
270. Nosonovsky, M. & Bhushan, B. Biologically Inspired Surfaces: Broadening the Scope of Roughness**. *Adv. Funct. Mater.* **18**, 843–855 (2008).
271. Truong, V. K. *et al.* Air-directed attachment of coccoid bacteria to the surface of superhydrophobic lotus-like titanium. *Biofouling* **28**, 539–550 (2012).
272. Ivanova, E. P. *et al.* Bactericidal activity of black silicon. *Nat. Commun.* **4**, 684–692 (2013).
273. Bhushan, B. *Principles and Applications of Tribology, Second Edition. Principles and*

Applications of Tribology, Second Edition **32**, (John Wiley & Sons, Ltd, 2013).

274. Subramanian, C. S., King, P. I., Reeder, M. F., Ou, S. & Rivir, R. B. Effects of Strong Irregular Roughness on the Turbulent Boundary Layer. *Flow, Turbul. Combust. Former. Applied Sci. Res.* **72**, 349–368 (2004).
275. Bons, J. P., Taylor, R. P., McClain, S. T. & Rivir, R. B. The Many Faces of Turbine Surface Roughness. *J. Turbomach.* **123**, 739 (2001).
276. Santini, M., Guilizzoni, M. & Fest-Santini, S. X-ray computed microtomography for drop shape analysis and contact angle measurement. *J. Colloid Interface Sci.* **409**, 204–210 (2013).
277. Santini, M. & Guilizzoni, M. 3D X-ray Micro Computed Tomography on Multiphase Drop Interfaces: From Biomimetic to Functional Applications. *Colloids Interface Sci. Commun.* **1**, 14–17 (2014).
278. Jenkins, L. M. & M, D. A. Contact angle measurements on fibers in the environmental scanning electron microscope. *Langmuir* **15**, 7829–7835 (1999).
279. Sundberg, M., Månsson, A. & Tågerud, S. Contact angle measurements by confocal microscopy for non-destructive microscale surface characterization. *J. Colloid Interface Sci.* **313**, 454–460 (2007).
280. Zheng, D. *et al.* Salvinia-Effect-Inspired ‘sticky’ Superhydrophobic Surfaces by Meniscus-Confined Electrodeposition. *Langmuir* **33**, 13640–13648 (2017).
281. Darmanin, T. & Guittard, F. Superhydrophobic and superoleophobic properties in nature. *Mater. Today* **18**, 273–285 (2015).
282. Cheng, Z. *et al.* Designing heterogeneous chemical composition on hierarchical structured copper substrates for the fabrication of superhydrophobic surfaces with controlled adhesion. *ACS Appl. Mater. Interfaces* **5**, 8753–8760 (2013).
283. Yuan, C., Huang, M., Yu, X., Ma, Y. & Luo, X. A simple approach to fabricate the rose petal-like hierarchical surfaces for droplet transportation. *Appl. Surf. Sci.* **385**, 562–568

- (2016).
284. Avramescu, R. E., Ghica, M. V., Dinu-Pîrvu, C., Prisada, R. & Popa, L. Superhydrophobic natural and artificial Surfaces-A structural approach. *Materials (Basel)*. **11**, (2018).
 285. Liu, M., Wang, S. & Jiang, L. Nature-inspired superwettability systems. *Nat. Rev. Mater.* **2**, 17036 (2017).
 286. Tan, X., Zahiri, B., Holt, C. M. B., Kubis, A. & Mitlin, D. A TEM based study of the microstructure during room temperature and low temperature hydrogen storage cycling in MgH₂ promoted by Nb-V. *Acta Mater.* **60**, 5646–5661 (2012).
 287. Neckernuss, T., Wiedemann, S., Plettl, A. & Ziemann, P. Moving Water Droplets Over Nanoscaled (Super) hydrophobic Wettability Contrasts: Experimental Test of a Simple Model Describing Driving Forces. *Adv. Mater. Interfaces* **1**, 1300033 (2014).
 288. Yang, R., Moni, P. & Gleason, K. K. Ultrathin Zwitterionic Coatings for Roughness-Independent Underwater Superoleophobicity and Gravity-Driven Oil-Water Separation. *Adv. Mater. Interfaces* **2**, 1400489 (2015).
 289. Babu, D. J. *et al.* Inscribing Wettability Gradients onto Superhydrophobic Carbon Nanotube Surfaces. *Adv. Mater. Interfaces* **1**, 1–6 (2014).
 290. Zahiri, B., Sow, P. K., Kung, C. H. & Mérida, W. Validation of surface wettability theories via electrochemical analysis. *Electrochem. commun.* **68**, 95–98 (2016).
 291. Zahiri, B., Sow, P. K., Kung, C. H. & Mérida, W. Electrochemical Approach to Evaluate the Wettability of Rough Surfaces. *ECS Trans.* **75**, 49–57 (2017).
 292. Yan, L. *et al.* A photo-induced ZnO coated mesh for on-demand oil/water separation based on switchable wettability. *Mater. Lett.* **163**, 247–249 (2016).
 293. Zhou, W., Li, G., Wang, L., Chen, Z. & Lin, Y. A facile method for the fabrication of a superhydrophobic polydopamine-coated copper foam for oil/water separation. *Appl. Surf. Sci.* **413**, 140–148 (2017).

294. Nikolić, N. D., Popov, K. I., Pavlović, L. J. & Pavlović, M. G. Morphologies of copper deposits obtained by the electrodeposition at high overpotentials. *Surf. Coatings Technol.* **201**, 560–566 (2006).
295. Xu, H., Feng, J.-X., Tong, Y.-X. & Li, G.-R. Cu₂O–Cu Hybrid Foams as High-Performance Electrocatalysts for Oxygen Evolution Reaction in Alkaline Media. *ACS Catal.* **7**, 986–991 (2017).
296. Yang, T., Liu, J., Dai, J. & Han, Y. Shaping particles by chemical diffusion and reaction. *CrystEngComm* **19**, 72–79 (2017).
297. Liu, J., Yang, T., Li, C., Dai, J. & Han, Y. Reversibly Switching Silver Hierarchical Structures via Reaction Kinetics. *Sci. Rep.* **5**, 1–8 (2015).
298. Avizienis, A. V. *et al.* Morphological transitions from dendrites to nanowires in the electroless deposition of silver. *Cryst. Growth Des.* **13**, 465–469 (2013).
299. Liu, W., Yang, T., Li, C., Che, P. & Han, Y. Regulating silver morphology via electrochemical reaction. *CrystEngComm* **17**, 6014–6022 (2015).
300. Zahiri, B., Amirkhiz, B. S., Danaie, M. & Mitlin, D. Bimetallic Fe-V catalyzed magnesium films exhibiting rapid and cycleable hydrogenation at 200 °C. *Appl. Phys. Lett.* **96**, (2010).
301. Zahiri, R. *et al.* Microstructural evolution during low temperature sorption cycling of Mg-AlTi multilayer nanocomposites. *Int. J. Hydrogen Energy* **37**, 4215–4226 (2012).
302. Dubal, D. P., Dhawale, D. S., Salunkhe, R. R., Jamdade, V. S. & Lokhande, C. D. Fabrication of copper oxide multilayer nanosheets for supercapacitor application. *J. Alloys Compd.* **492**, 26–30 (2010).
303. Patake, V. D., Joshi, S. S., Lokhande, C. D. & Joo, O. S. Electrodeposited porous and amorphous copper oxide film for application in supercapacitor. *Mater. Chem. Phys.* **114**, 6–9 (2009).
304. Zhu, Y., Mimura, K. & Isshiki, M. The Effect of Impurities on the Formation of the Inner

- Porous Layer in the Cu₂O Scale During Copper Oxidation. *Oxid. Met.* **61**, 293–301 (2004).
305. Yang, J. *et al.* Lasting superhydrophobicity and antibacterial activity of Cu nanoparticles immobilized on the surface of dopamine modified cotton fabrics. *Surf. Coatings Technol.* **309**, 149–154 (2017).
306. Iijima, Y., Niimura, N. & Hiraoka, K. Prevention of the Reduction of CuO during X-ray Photoelectron Spectroscopy Analysis. *Surf. interface Anal.* **24**, 193–197 (1996).
307. Chusuei, C. C., Brookshier, M. A. & Goodman, D. W. Correlation of relative X-ray photoelectron spectroscopy shake-up intensity with CuO particle size. *Langmuir* **15**, 2806–2808 (1999).
308. Biesinger, M. C., Lau, L. W. M., Gerson, A. R. & Smart, R. S. C. Resolving surface chemical states in XPS analysis of first row transition metals, oxides and hydroxides: Sc, Ti, V, Cu and Zn. *Appl. Surf. Sci.* **257**, 887–898 (2010).
309. Biesinger, M. C., Hart, B. R., Polack, R., Kobe, B. A. & Smart, R. S. C. Analysis of mineral surface chemistry in flotation separation using imaging XPS. *Miner. Eng.* **20**, 152–162 (2007).
310. Chastain, J., King, R. C. & Moulder, J. F. *Handbook of X-ray photoelectron spectroscopy: a reference book of standard spectra for identification and interpretation of XPS data.* (Physical Electronics Eden Prairie, MN, 1995).
311. Wagner, C. D. *et al.* NIST Standard Reference Database 20, Version 3.4 (web version). (2003).
312. Wang, Y. *et al.* Synthesis of porous Cu₂O/CuO cages using Cu-based metal-organic frameworks as templates and their gas-sensing properties. *J. Mater. Chem. a* **3**, 12796–12803 (2015).
313. Gillot, B., Buguet, S., Kester, E., Baubet, C. & Tailhades, P. Cation valencies and distribution in the spinels Co_xCu_yMn_zFe₄O_{4+δ} (δ ≥ 0) thin films studied by X-ray photoelectron spectroscopy. *Thin Solid Films* **357**, 223–231 (1999).

314. An, L. *et al.* A Self-Standing High-Performance Hydrogen Evolution Electrode with Nanostructured NiCo₂O₄/CuS Heterostructures. *Adv. Funct. Mater.* **25**, 6814–6822 (2015).
315. Tian, Z. Y., Vieker, H., Kouotou, P. M. & Beyer, A. In situ characterization of Cu–Co oxides for catalytic application. *Faraday Discuss.* **177**, 249–262 (2015).
316. Dhal, S. *et al.* Adhesive hydrophobicity of Cu₂O nano-columnar arrays induced by nitrogen ion irradiation. *Soft Matter* **11**, 9211–9217 (2015).
317. Li, X.-M. *et al.* What do we need for a superhydrophobic surface? A review on the recent progress in the preparation of superhydrophobic surfaces. *Chem. Soc. Rev.* **36**, 1350 (2007).
318. Sundstrom, L. G. & Bark, F. H. On morphological instability during electrodeposition with a stagnant binary electrolyte. *Electrochim. Acta* **40**, 599–614 (1995).
319. Wang, B., Zhang, Y., Shi, L., Li, J. & Guo, Z. Advances in the theory of superhydrophobic surfaces. *J. Mater. Chem.* **22**, 20112 (2012).
320. Hibbert, D. B. Introduction to electrochemistry. in *Introduction to electrochemistry* 1–10 (Macmillan Education UK, 1993). doi:10.1007/978-1-349-22721-1_1
321. Le, W. Z. & Liu, Y. Q. Preparation of nano-copper oxide modified glassy carbon electrode by a novel film plating/potential cycling method and its characterization. *Sensors Actuators, B Chem.* **141**, 147–153 (2009).
322. Nakayama, S., Kimura, A., Shibata, M., Kuwabata, S. & Osakai, T. Voltammetric Characterization of Oxide Films Formed on Copper in Air. *J. Electrochem. Soc.* **148**, B467 (2001).
323. Bard, A. J. *Standard Potentials in Aqueous Solution*. (Routledge, 2017).
324. Dong, S., Xie, Y. & Cheng, G. Cyclic voltammetric and spectroelectrochemical studies of copper in alkaline solution. *Electrochim. Acta* **37**, 17–22 (1992).
325. Teo, W. Z., Ambrosi, A. & Pumera, M. Direct electrochemistry of copper oxide

- nanoparticles in alkaline media. *Electrochem. commun.* **28**, 51–53 (2013).
326. Peters, A. M. *et al.* Cassie-Baxter to Wenzel state wetting transition: Scaling of the front velocity. *Eur. Phys. J. E* **29**, 391–397 (2009).
327. Zhang, G., Walker, M. & Unwin, P. R. Low-Voltage Voltammetric Electrowetting of Graphite Surfaces by Ion Intercalation/Deintercalation. *Langmuir* **32**, 7476–7484 (2016).
328. Preston, D. J. *et al.* Effect of hydrocarbon adsorption on the wettability of rare earth oxide ceramics. *Appl. Phys. Lett.* **105**, (2014).
329. Liu, P. *et al.* Insights into the superhydrophobicity of metallic surfaces prepared by electrodeposition involving spontaneous adsorption of airborne hydrocarbons. *Appl. Surf. Sci.* **324**, 576–583 (2015).
330. Wang, F., Lei, S., Xu, Y. & Ou, J. Green Approach to the Fabrication of Superhydrophobic Mesh Surface for Oil/Water Separation. *ChemPhysChem* **16**, 2237–2243 (2015).
331. Campbell, W. E. & Thomas, U. B. The Oxidation of Metals. *Trans. Electrochem. Soc.* **91**, 623 (1947).
332. Huan, T. N. *et al.* A Dendritic Nanostructured Copper Oxide Electrocatalyst for the Oxygen Evolution Reaction. *Angew. Chemie - Int. Ed.* **56**, 4792–4796 (2017).
333. Kalisvaart, P. *et al.* Thermodynamically destabilized hydride formation in “bulk” Mg–AlTi multilayers for hydrogen storage. *Phys. Chem. Chem. Phys.* **15**, 16432 (2013).
334. Zahiri, B., Amirkhiz, B. S. & Mitlin, D. Hydrogen storage cycling of MgH₂ thin film nanocomposites catalyzed by bimetallic Cr Ti. *Appl. Phys. Lett.* **97**, 083106 (2010).
335. Cheng, S.-L. & Chen, M.-F. Fabrication, characterization, and kinetic study of vertical single-crystalline CuO nanowires on Si substrates. *Nanoscale Res. Lett.* **7**, 119 (2012).
336. Zhang, X. *et al.* Nanoparticle-aggregated CuO nanoellipsoids for high-performance non-enzymatic glucose detection. *J. Mater. Chem. A* **2**, 10073 (2014).

337. Cao, M. *et al.* A controllable synthetic route to Cu, Cu₂O, and CuO nanotubes and nanorods. *Chem. Commun. (Camb)*. **1**, 1884–1885 (2003).
338. Hou, J. *et al.* High-performance p-Cu₂O/n-TaON heterojunction nanorod photoanodes passivated with an ultrathin carbon sheath for photoelectrochemical water splitting. *Energy Environ. Sci.* **7**, 3758–3768 (2014).
339. Iijima, Y., Niimura, N. & Hiraoka, K. Prevention of the Reduction of CuO during X-ray Photoelectron Spectroscopy Analysis. *Surf. Interface Anal.* **24**, 193–197 (1996).
340. Dhal, S. *et al.* Adhesive hydrophobicity of Cu₂O nano-columnar arrays induced by nitrogen ion irradiation. *Soft Matter* **11**, 9211–9217 (2015).
341. Xu, Z., Jiang, D., Wei, Z., Chen, J. & Jing, J. Fabrication of superhydrophobic nano-aluminum films on stainless steel meshes by electrophoretic deposition for oil-water separation. *Appl. Surf. Sci.* **427**, 253–261 (2018).
342. Chu, Z., Feng, Y. & Seeger, S. Oil/water separation with selective superantwetting/superwetting surface materials. *Angew. Chemie - Int. Ed.* **54**, 2328–2338 (2015).
343. Pi, P. *et al.* Superhydrophobic Cu₂S@Cu₂O film on copper surface fabricated by a facile chemical bath deposition method and its application in oil-water separation. *Appl. Surf. Sci.* **396**, 566–573 (2017).
344. Li, J. J., Zhou, Y. N. & Luo, Z. H. Smart Fiber Membrane for pH-Induced Oil/Water Separation. *ACS Appl. Mater. Interfaces* **7**, 19643–19650 (2015).
345. Zhang, G., Zhang, X., Huang, Y. & Su, Z. A surface exhibiting superoleophobicity both in air and in seawater. *ACS Appl. Mater. Interfaces* **5**, 6400–6403 (2013).
346. Extrand, C. W., Sung, I. M., Hall, P. & Schmidt, D. Superwetting of structured surfaces. *Langmuir* **23**, 8882–8890 (2007).
347. Wang, Z. *et al.* Wicking Enhancement in Three-Dimensional Hierarchical Nanostructures. *Langmuir* **32**, 8029–8033 (2016).

348. Jung, Y. C. & Bhushan, B. Wetting behavior of water and oil droplets in three-phase interfaces for hydrophobicity/philicity and oleophobicity/philicity. *Langmuir* **25**, 14165–14173 (2009).
349. Li, H. *et al.* Vapor-liquid interfacial reaction to fabricate superhydrophilic and underwater superoleophobic thiol-ene/silica hybrid decorated fabric for oil/water separation. *Appl. Surf. Sci.* **427**, 92–101 (2018).
350. Ye, S., Cao, Q., Wang, Q., Wang, T. & Peng, Q. A highly efficient, stable, durable, and recyclable filter fabricated by femtosecond laser drilling of a titanium foil for oil-water separation. *Sci. Rep.* **6**, 37591 (2016).
351. Yong, J., Chen, F., Yang, Q., Huo, J. & Hou, X. Superoleophobic surfaces. *Chem. Soc. Rev.* **46**, 4168–4217 (2017).
352. Hou, K. *et al.* Durable underwater superoleophobic PDDA/halloysite nanotubes decorated stainless steel mesh for efficient oil–water separation. *Appl. Surf. Sci.* **416**, 344–352 (2017).
353. Yu, H. *et al.* Mechanically durable underwater superoleophobic surfaces based on hydrophilic bulk metals for oil/water separation. *Appl. Surf. Sci.* **437**, 400–409 (2018).
354. Venkataraman, N. & Raghavan, S. Dissolution and electrochemical impedance spectroscopy studies of thin copper oxide films on copper in semi-aqueous fluoride solutions. *Microelectron. Eng.* **87**, 1689–1695 (2010).
355. Su, F. & Yao, K. Facile fabrication of superhydrophobic surface with excellent mechanical abrasion and corrosion resistance on copper substrate by a novel method. *ACS Appl. Mater. Interfaces* **6**, 8762–8770 (2014).
356. Tuberquia, J. C., Song, W. S. & Jennings, G. K. Investigating the superhydrophobic behavior for underwater surfaces using impedance-based methods. *Anal. Chem.* **83**, 6184–6190 (2011).
357. Singh Raman, R. K. *et al.* Protecting copper from electrochemical degradation by graphene coating. *Carbon N. Y.* **50**, 4040–4045 (2012).

358. Fattah-alhosseini, A., Imantalab, O. & Attarzadeh, F. R. Enhancing the Electrochemical Behavior of Pure Copper by Cyclic Potentiodynamic Passivation: A Comparison between Coarse- and Nano-Grained Pure Copper. *Metall. Mater. Trans. B Process Metall. Mater. Process. Sci.* **47**, 2761–2770 (2016).
359. Liu, T. *et al.* Corrosion behavior of super-hydrophobic surface on copper in seawater. *Electrochim. Acta* **52**, 8003–8007 (2007).
360. Mishra, R. K., Baek, G. W., Kim, K., Kwon, H.-I. & Jin, S. H. One-step solvothermal synthesis of carnation flower-like SnS₂ as superior electrodes for supercapacitor applications. *Appl. Surf. Sci.* **425**, 923–931 (2017).
361. Rammelt, U. & Reinhard, G. On the applicability of a constant phase element (CPE) to the estimation of roughness of solid metal electrodes. *Electrochim. Acta* **35**, 1045–1049 (1990).
362. Khorsand, S., Raeissi, K. & Ashrafizadeh, F. Corrosion resistance and long-term durability of super-hydrophobic nickel film prepared by electrodeposition process. *Appl. Surf. Sci.* **305**, 498–505 (2014).
363. Xiao, F. *et al.* Superhydrophobic CuO nanoneedle-covered copper surfaces for anticorrosion. *J. Mater. Chem. A* **3**, 4374–4388 (2015).
364. Huh, J.-H. *et al.* Enhancement of seawater corrosion resistance in copper using acetone-derived graphene coating. *Nanoscale* **6**, 4379–4386 (2014).
365. Cai, Y. *et al.* Nanofibrous metal–organic framework composite membrane for selective efficient oil/water emulsion separation. *J. Memb. Sci.* **543**, 10–17 (2017).
366. Zheng, S., Xu, M. & Lu, X. Facile method toward hierarchical fullerene architectures with enhanced hydrophobicity and photoluminescence. *ACS Appl. Mater. Interfaces* **7**, 20285–20291 (2015).
367. Rukosuyev, M. V., Lee, J., Cho, S. J., Lim, G. & Jun, M. B. G. One-step fabrication of superhydrophobic hierarchical structures by femtosecond laser ablation. *Appl. Surf. Sci.* **313**, 411–417 (2014).

368. Utech, S., Bley, K., Aizenberg, J. & Vogel, N. Tailoring re-entrant geometry in inverse colloidal monolayers to control surface wettability. *J. Mater. Chem. A* **4**, 6853–6859 (2016).
369. Li, B. *et al.* Underwater superoleophobic stainless steel mesh fabricated by laser cladding a copper foil for oil–water separation. *Mater. Res. Express* **5**, 075014 (2018).
370. Li, J. *et al.* Superhydrophobic meshes that can repel hot water and strong corrosive liquids used for efficient gravity-driven oil/water separation. *Nanoscale* **8**, 7638–7645 (2016).
371. Wen, Q., Di, J., Jiang, L., Yu, J. & Xu, R. Zeolite-coated mesh film for efficient oil-water separation. *Chem. Sci.* **4**, 591–595 (2013).
372. Wang, H. & Pilon, L. Physical interpretation of cyclic voltammetry for measuring electric double layer capacitances. *Electrochim. Acta* **64**, 130–139 (2012).
373. Xu, F. *et al.* Fast ion transport and high capacitance of polystyrene-based hierarchical porous carbon electrode material for supercapacitors. *J. Mater. Chem.* **21**, 1970–1976 (2011).
374. Kim, M., Oh, I. & Kim, J. Hierarchical porous silicon carbide with controlled micropores and mesopores for electric double layer capacitors. *J. Power Sources* **282**, 277–285 (2015).
375. Purkait, T., Singh, G., Kumar, D., Singh, M. & Dey, R. S. High-performance flexible supercapacitors based on electrochemically tailored three-dimensional reduced graphene oxide networks. *Sci. Rep.* **8**, 1–13 (2018).

Appendices

Appendix A: Measurement of advancing and receding contact angles

Typical procedures for the advancing (ACA) and receding contact angle (RCA) measurement using the needle-syringe method are illustrated in Figure A1 using smooth GC as an example. The ACA corresponds to the value at which the contact angle (CA) remains constant with increasing droplet volume and diameter. The RCA is identified as the point prior to the sudden increase in CA during the volume retraction, as illustrated in Figure A1 (b). For determination of RCA using the droplet evaporation method, the RCA is the value of the first contact angle peak following a decrease in the droplet base diameter.

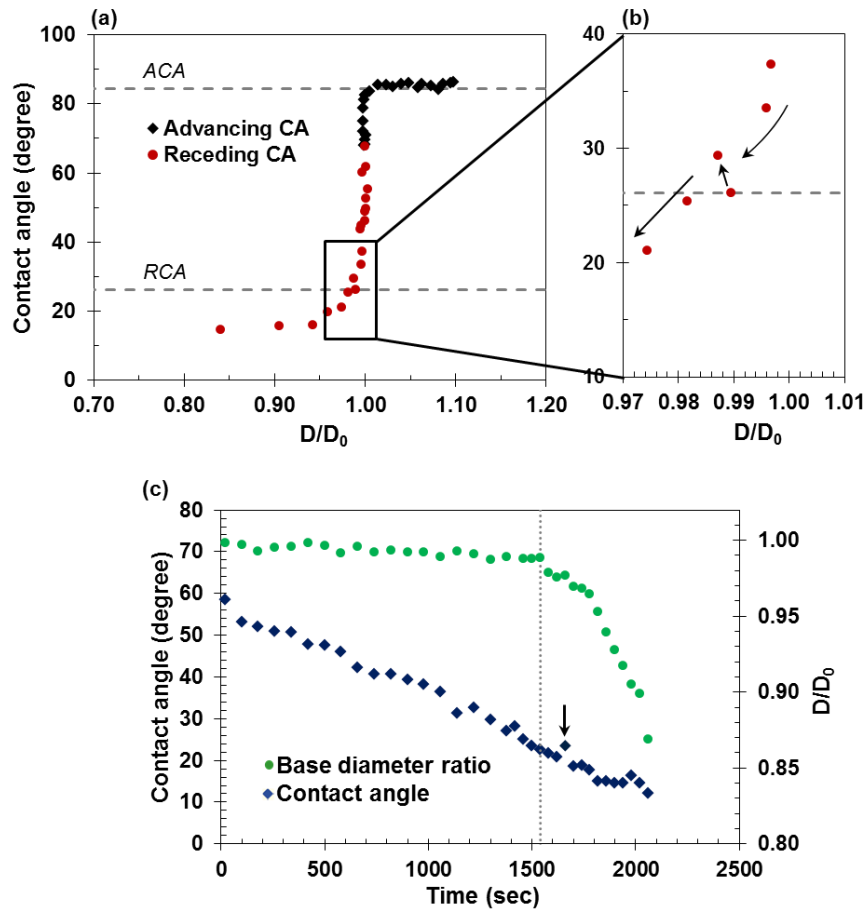


Figure A1: (a) and (b) Exemplification of the typical advancing (ACA) and receding contact angle (RCA) measurements for the smooth glassy carbon (GC) surface. D is the base diameter and D_0 is the starting base diameter for a 5 mL droplet. The RCA was achieved after about 1% variation in the base diameter and a sudden increase in the CA during the receding process. (c) Contact angle during the evaporation of 5 mL droplet on the smooth GC. The first local maximum (arrow) in the contact angle after the decrease in the base diameter (denoted by the dotted line) is considered as the RCA.

Appendix B: Cyclic voltammetry plots of mechanically abraded samples at different sweep rates and electrolyte concentrations

Figure B1 compares the cyclic voltammetry (CV) plots of the smooth and mechanically abraded glassy carbon samples at various sweep rates obtained using 1 mM and 1 M Na₂SO₄ aqueous electrolytes. The symmetric shape of the CV curves implies that the electrochemical double layer charging process is reversible²⁴⁵. At low sweep rate, there is sufficient time for ion diffusion from the bulk electrolyte to the electrode surface, ensuring nearly complete ion access to the available surface sites. As a result, a quasi-rectangular CV shape is observed. As the sweep rate increases, the CV curve becomes skewed. The distortion of the CV curve with increasing sweep rate is even more prominent when a lower electrolyte concentration (1 mM Na₂SO₄) is used, as illustrated in the transition from quasi-rectangular to an elliptical shape in Figure B1. The deformation of the CV plot at high sweep rate can be attributed to sluggish ion transport that fails to keep up with the potential variation during the double layer charging process³⁷². Such mass transport limitation is exacerbated at low concentration due to lower ion mobility associated with a lower concentration gradient. Overall, the dependence of capacitance on the sweep rate is weaker at higher electrolyte concentration due to improved mass transfer kinetics²⁴⁵.

Compared to the smooth sample, the degree of distortion in the CV with the sweep rate and concentration is more pronounced for the rough samples. The rough samples offer longer and more tortuous ion transport pathway for charge accumulation at the electrode-electrolyte interface. Consequently, the restriction of the ionic motion gives rise to a slower reorganization of the double layer at the switching potentials during CV measurement, leading to lag in the attainment of the steady state current^{203,373,374}. In addition, the extent of electrode surface involved in the charging dynamics strongly depends on ion penetration depth into the roughness structure, which is also dictated by the sweep rate and solution concentration. When a higher sweep rate or a lower concentration is used, the greater transport resistance renders only the outer electrode surface to be accessible to the ions³⁷⁵. Due to delay in the double layer charging, distortion of the CVs and lower capacitance value are observed. In contrast, the ion diffusion length is much smaller for the smooth sample, providing faster charge propagation. Thus the impact of the ion diffusion rate on the charging process is less significant. As shown in Figure

B1, the dissimilarity between the CVs of the smooth sample obtained at different sweep rates and concentrations is minimal.

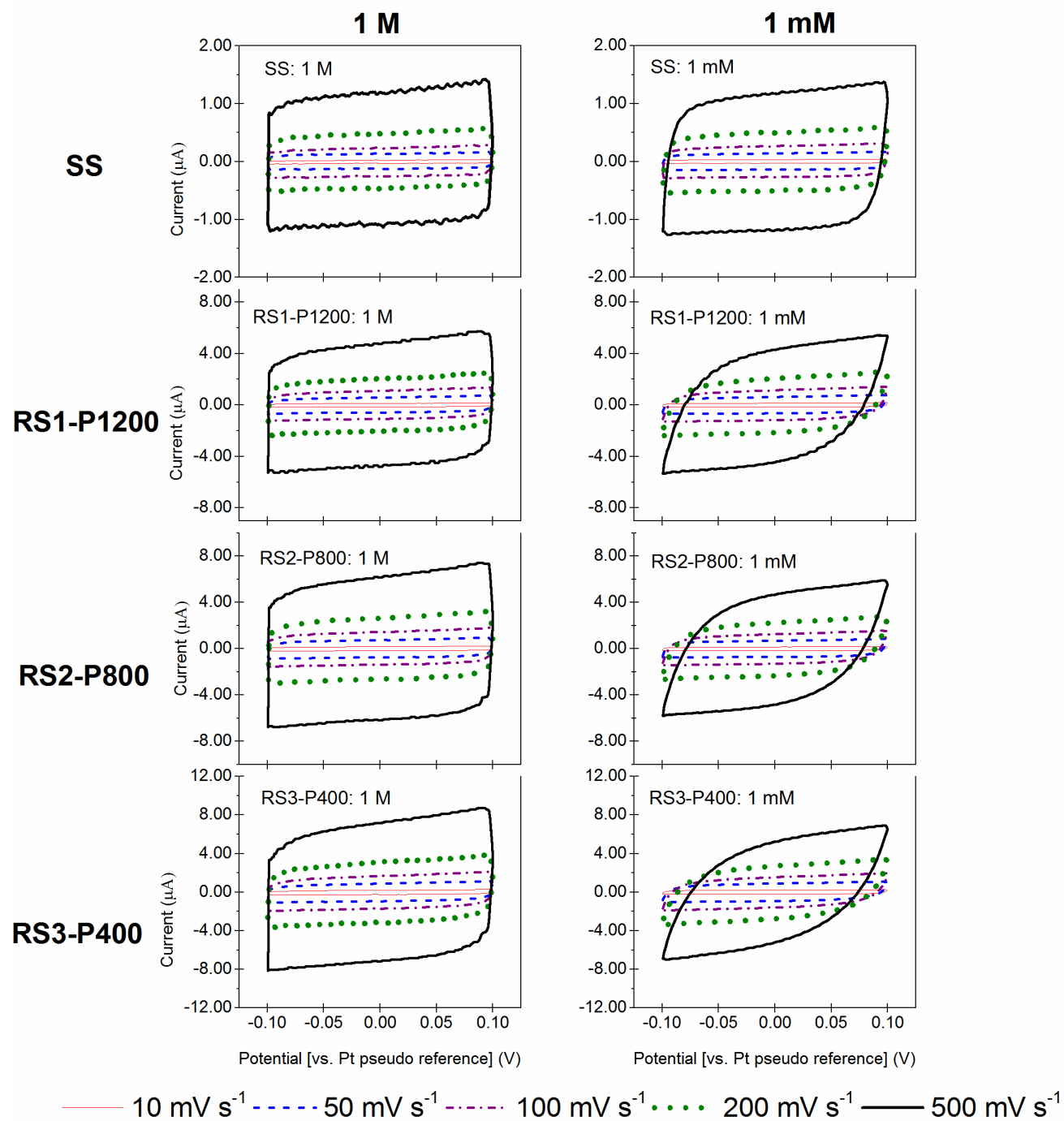


Figure B1: Cyclic voltammograms of mechanically abraded glassy carbon samples obtained using 1 mM and 1 M Na₂SO₄ electrolyte at different sweep rates of 10, 50, 100, 200, and 500 mV s⁻¹.

Appendix C: Stickiness of the electrodeposited copper surface

Figure C1 shows the time-lapsed motion of the droplet upon removal of the Pt wires. The droplet rolls off the sample surface towards the edges.

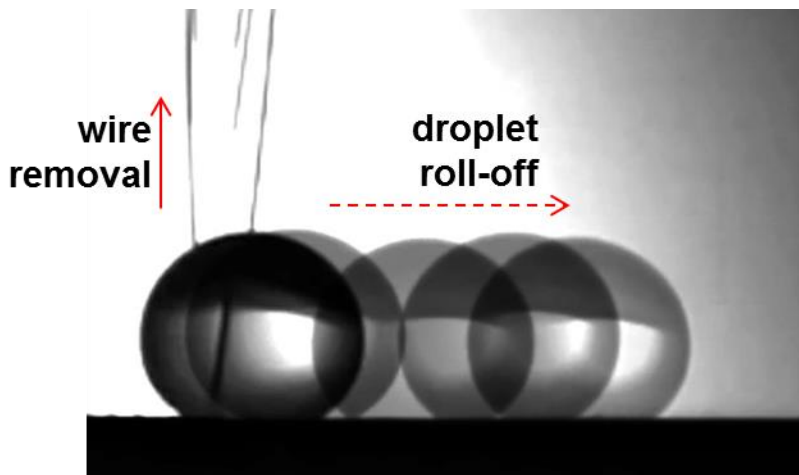


Figure C1: The easy roll-off motion of the droplet upon the removal of the Pt wires. The droplet moves towards the edge of the sample.

Figure C2 demonstrates the impact of applying positive potential on the contact angle and the adhesiveness of the surface. Figure C2 (a) shows the easy roll-off behaviour of the as-deposited surface when Pt wires are used to move the droplet on the surface. Upon applying a positive 0.5 V vs. Pt pseudo-reference electrode for over 5 min, the surface becomes more adhesive. This is demonstrated in Figure C2 (b) where the droplet does not move using the same rolling technique. The potential of the Pt pseudo-reference electrode is about -0.25 V relative to the Ag/AgCl reference electrode. Applying higher voltages (>0.5 V vs. Pt) promotes the water decomposition reaction on the Pt counter electrode.

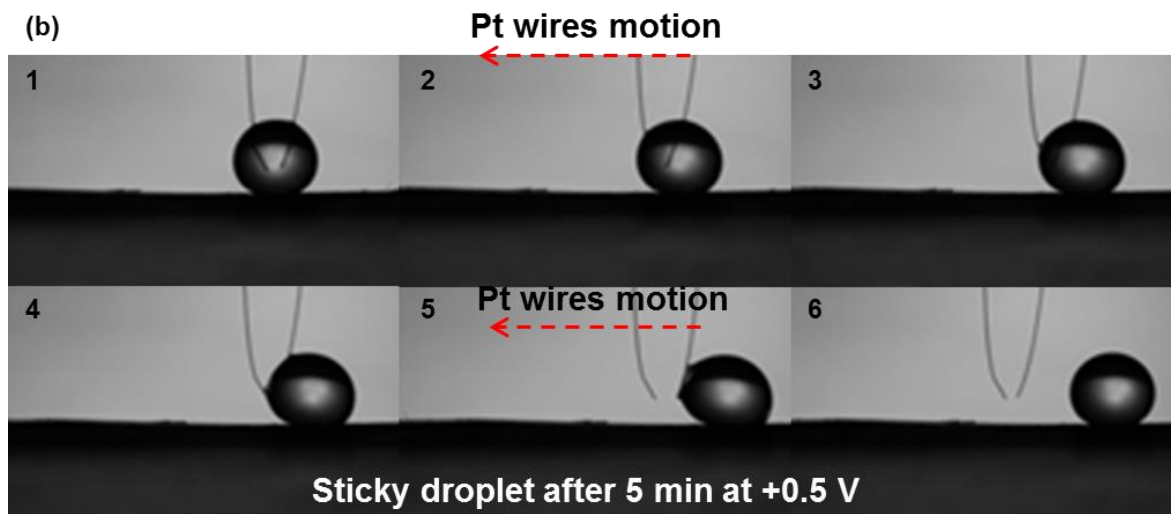
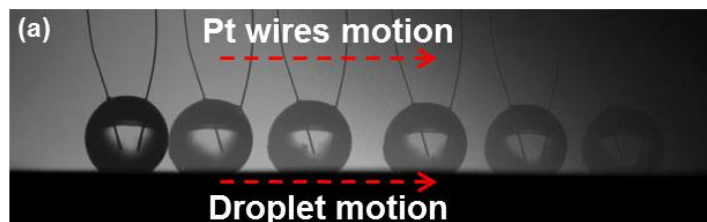


Figure C2: (a) The easy rolling motion of the droplet with the aid of Pt wires. (b) The droplet becomes sticky after applying +0.5 V vs. Pt pseudo reference for 5 min.

Appendix D: Effect of ambient hydrocarbon adsorption and mild heat drying at 100°C

In order to investigate the possibility of adsorption of carbonaceous species on the surface upon ambient exposure, XPS survey scans were performed. Three sets of samples were compared: (1) sample in the as-deposited state, (2) sample prepared by applying -0.8 V vs. Ag/AgCl for 200 seconds (sample at the middle of transition), and (3) sample after the wetting transition. Figure D1 (a) and (b) show the XPS survey scan and C 1s profiles of the samples in the as-deposited state, in the mid-point (-0.8 V, 200 s), and at the end of wetting transition. The overall survey scans do not show any significant variation in the surface composition. The C 1s signal does not show any significant change in the carbon content at the different stages of the wetting transition that could contribute significant modification to the surface wetting properties

340

XPS analysis was also performed on two samples that were air-dried (room temperature for 1 hr) and heat-dried (100°C) to examine the presence of adsorbed species upon mild thermal treatment in air. Figure D1 (c) and (d) compares the surface composition and oxygen species for the samples dried at room temperature and at 100°C. As can be seen in Figure D1 (c) and (d), the surface composition and the type of adsorbed species were unchanged.

These results confirm that although adventitious carbon presents on the surface, the amount of carbonaceous species is similar for all the samples prepared in this study. Furthermore, the use of mild temperature (100°C) for accelerating the sample drying process does not alter the hydrocarbon content at the copper surface.

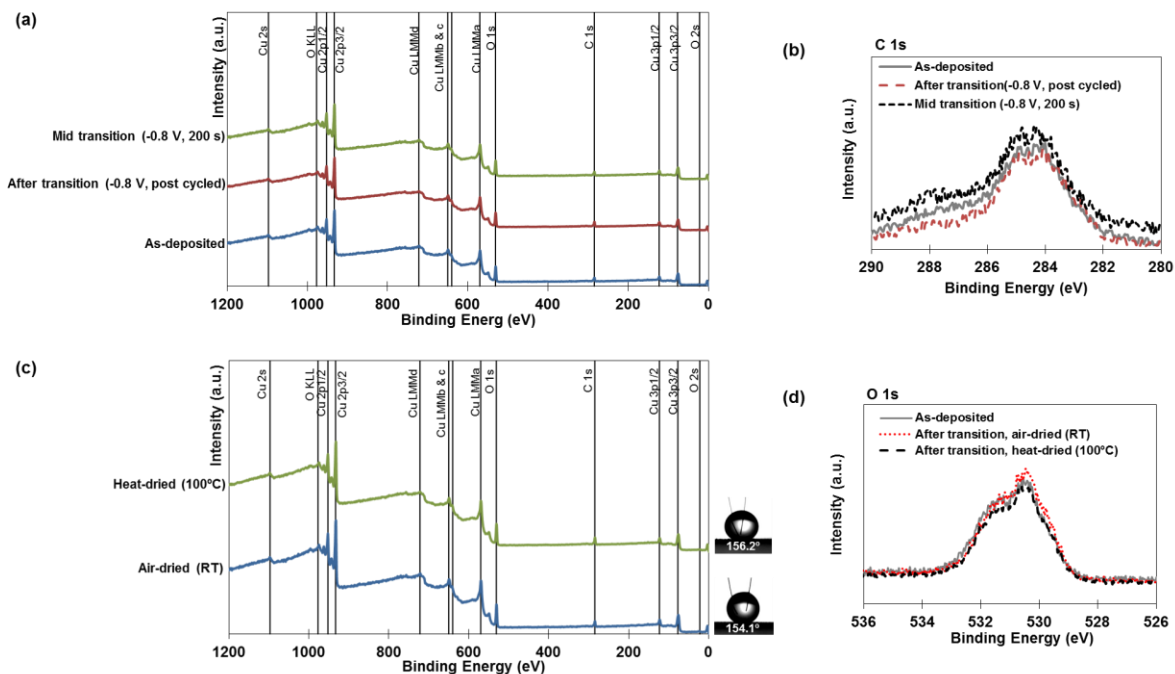


Figure D1: (a) XPS survey scan and (b) C 1s signal for the as-deposited, mid-point and the end of the wetting transition. Similar C 1s intensity and shape suggests similar carbon content for all the samples. (c) XPS survey scan and (b) O 1s spectrum for samples dried at room temperature (air-dried) and at 100°C (heat-dried) and comparison vs. the as-deposited state. The CA for the air-dried vs. the heat-dried samples is also shown in the inset.

Appendix E: Microstructural characterization of the copper mesh before and after 30 wetting transition cycles

SEM micrographs of the copper mesh prior to and after 30 separation cycles are shown in Figure E1 (a) and (b). Comparison of these micrographs reveals that the dendritic microstructure on the copper mesh remains intact after the wetting cycles. Thus the alternate application of voltage and air drying do not change the surface morphology of the mesh.

Figure E1 (c) and (d) show the STEM-EDS mapping of the individual dendritic arm before and after the wetting transition cycles, respectively. Similar to the as-deposited dendritic structures, the post-cycled dendrites contains a thin layer of O₂-rich region at the exterior surface shielding the interior section of high Cu concentration. Therefore the formation of copper oxide species and/or oxygen adsorption occur regardless of whether the electrochemical reduction reaction is initiated.

Figure E1 (e) compares the XPS profiles of the as-deposited and post-cycled Cu structures. The chemical states of copper of the post-cycled sample were identified using similar fitting parameters for the as-deposited Cu mesh. The overall XPS profile and the position of the fitted curve for the Cu mesh after the wetting cycles are almost identical to that of the as-deposited Cu mesh. The similarity between the XPS results of the Cu mesh before and after the wetting transition cycles further corroborates that the voltage application and air drying did not modify the Cu microstructure and chemical state.

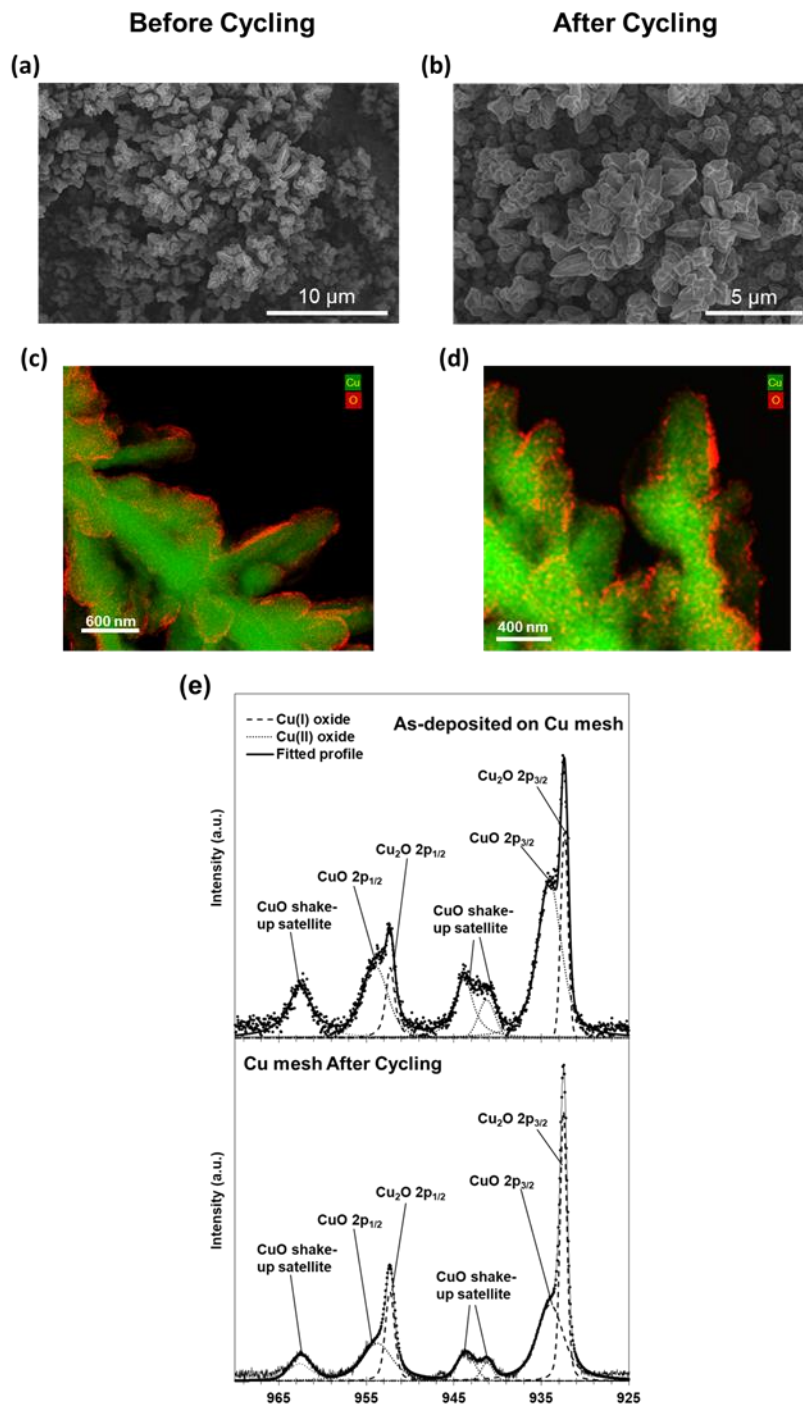


Figure E1: SEM micrographs of the (a) as-deposited and (b) post-cycled copper mesh. STEM-EDS mapping of Cu and O elements on single dendrite branch (c) before and (d) after the wetting cycling. (e) XPS spectra of the Cu 2p region for the as-deposited and post-cycled Cu samples are similar to each other with identical copper oxide species.